VIBRATIONAL SPECTRA, THEORETICAL CALCULATIONS, AND

STRUCTURES OF CYCLIC SILANES,

2,4,7-TRIOXA(3.3.0)OCTANE AND BOTRYOCOCCENES

A Dissertation

by

HYE JIN CHUN

Submitted to the Office of Graduate and Professional Studies of
Texas A&M University
in partial fulfillment of the requirements for the degree of

DOCTOR OF PHILOSOPHY

Chair of Committee,	Jaan Laane
Committee Members,	Robert R. Lucchese
	Steven E. Wheeler
	George W. Kattawar
Head of Department,	Francois Gabbai

December 2014

Major Subject: Chemistry

ABSTRACT

The vibrational spectra and structures of several cyclic silanes and a bicyclic molecule have been investigated with high-level *ab initio* and density function theory (DFT) calculations. In addition, the Raman spectra of botryococcene hydrocarbons have been studied to help with their identification.

Infrared and Raman spectra and *ab initio* and DFT calculations have been utilized to study 1,3-disilacyclopent-3-ene, 1,3-disilacyclopentane, 1-silacyclopent-3-ene, silacyclopentane and their derivatives. In each case the agreement between observed and calculated infrared and Raman spectra was very good.

Theoretical computations have also been used to calculate the potential energy surfaces (PES) for four cyclic silanes. The calculated ring-puckering potential energy functions of 1-silacyclopent-3-ene and 1,3-disilacyclopent-3-ene had barriers of 3.8 cm^{-1} and 0 cm^{-1}, respectively, in good agreement with experimental results. The calculated results for and 1,3-disilacyclopentane predicted ring-twisting barriers of 2493 cm^{-1} (vs. 2110 cm^{-1} observed) and 1395 cm^{-1}, respectively. The conformational energies for the bent forms were calculated to be 1467 cm^{-1} (vs. 1509 cm^{-1} observed) for the former and 878 cm^{-1} for the latter relative to the energy of the twist minima.

The vibrational assignments of 2,4,7-trioxa(3.3.0)octane have been made based on its infrared and Raman spectra and theoretical DFT calculations. The two ring-puckering motions (in-phase and out-of-phase) were observed in the Raman spectrum of the liquid at 249 and 205 cm^{-1} and these values correspond well to the DFT values of

247 and 198 cm^{-1}. *Ab initio* calculations were utilized to calculate the structures and conformational energies for the four energy minima and the barriers to interconversion and the data were utilized to generate a two-dimensional PES for the two ring-puckering motions.

The Raman and infrared spectra of liquid squalene, which is a building block molecule for the production of essential cellular molecules, have been collected and assigned using DFT calculations. This was helpful for analyzing the Raman spectra of *botryococcus braunii*. DFT calculations also assisted in understanding the Raman spectra of the botryococcenes. The spectral region from 1600-1700 cm^{-1} shows C=C stretching bands specific for botryococcenes, and this is of great value for identifying the specific molecules.

DEDICATION

I wish to dedicate my dissertation to my Lord.

AKNOWLEDGMENTS

TABLE OF CONTENTS

LIST OF TABLES

CHAPTER I

INTRODUCTION

Spectroscopic methods such as infrared and Raman spectroscopy have been used to record and determine the vibrarional spectra, potential energy functions (PEFs), and structures of many molecules for a number of decades. Infrared and Raman spectroscopy were used in a complementary way. Infrared spectroscopy results from a dipole moment changes in molecules during vibrations. On the other hand, a polarizability change during the vibration is required for Raman spectroscopy. Far-infrared spectra were used to determine the ring-puckering and ring-twisting potential energy functions of small cyclic and bicylic molecules. Infrared and Raman spectroscopy were utilized to collect the vibrational spectra experimentally for 2,4,7-trioxa(3.3.0)octane, squalene and botryococcene hydrocarbons in this study.

Density functional theory (DFT) calculations were carried out to determine the calculated vibrarional spectra and vibrational assignments for 1,3-disilacyclopent-4-ene, 1,3-disilacyclopentane, 1-silacyclopent-3-ene, silacyclopentane, 2,4,7-trioxa(3.3.0)octane, squalene and botryococcene hydrocarbons. High level *ab initio* computations were used to calculate the conformational structures and potential energy functions of the cyclic and bicyclic molecules. The potential energy surfaces (PESs) were calculated with the conformational energies for different values of selected vibrational coordinates.

Vibrational Spectra, Theoretical Calculations, and Potential Energy Surfaces of 2,4,7-Triox(3.3.0)octane

Two-dimentional potential energy surfaces (PESs) for a number of bicyclic molecules have been determined in past several decades [1-3]. 2,4,7-Trioxa(3.3.0)octane (247TOO) is an unusual bicyclic molecule which can have the four different conformational forms. These are determined by the directions of the two ring- puckering motions. In this study the infrared and Raman spectra were collected. The vibrational frequencies were assigned. The computational calculations of vibrational spectra, PESs, and structures of four different conformational forms have been carried out using *ab initio* and DFT calculations.

Spectroscopic and Theoretical Investigations of Cyclic Silanes

For over four decades the cyclic silanes such as 1,3-disilacyclopent-4-ene, 1,3-disilacyclopentane, 1-silacyclopent-3-ene, and silacyclopentane have been studied to determine the potential energy functions and conformations. Colegrove and Laane reported the first preparation of 1,3-disilacyclopent-4-ene and 1,3-disilacyclopentane and their tetrachloro derivatives in 1991 [4]. In the previous studies of 1,3-disilacyclopent-4-ene[4] and 1-silacyclopent-3-ene [5-8], the ring-puckering potential energy surfaces and the far-infrared spectra were reported. The ring-puckering and ring-twisting potential energy surfaces of 1,3-disilacyclopentane and silacyclopentane were determined using far-infrared spectra [9]. Infrared and Raman spectra of 1,3-disilacyclopent-4-ene and 1,3-disilacyclopentane and their tetrachloro derivatives were analyzed [10]. In the

present work, *ab initio* and density function theory (DFT) calculations were used to calculate the vibrational spectra, potential energy functions and structures of these four cyclic silanes. The conformational energy was calculated point by point for the ring-puckering and ring-twisting potential energy functions.

Raman Studies of Squalene and Botryococcenes

Squalene is a linear triterpene molecule found in many organisms throughout nature including mammals, plants, and bacteria [11,12]. The limited studies of Raman spectroscopy analysis for squalene were reported to identify squalene as a component of olive oil [13], to study the effect of squalene on the packing of lipid bilayers and monolayers [14], to analyze the degradation of squalene by bacteria [15], and to analyze the components of sebaceous gland exudates [16]. However, the detailed analysis and structure studies of squalene were not reported based on Raman spectroscopy. In this study, the liquid infrared and Raman spectra of squalene were collected. The calculated vibrational spectra have been determined and assigned by DFT computations.

The use of green algae has been of interest because of the depletion of world petroleum reserves. The recent methods of detecting algal oil production are complicated, time consuming, and destructive [17]. Raman spectroscopy is one of the techniques to detect various molecular compounds in algae and is a valuable method for studying algae because Raman spectroscopy can detect algae in aqueous samples and differentiate algal strains. In this study, the Raman spectroscopy and DFT calculations

were carried out for the characterization of botryococcenes from the B race of *B. braunii*.

CHAPTER II

THEORETICAL AND COMPUTATIONAL METHODS

Ab initio Calculations

Ab initio methods involve theoretical quantum mechanical calculations and can be used to calculate molecular structures, energies, and vibrational spectra. These methods include Hartree–Fock (HF), Møller–Plesset Perturbation Theory (MPn), and coupled cluster theory (CC). In this study the MP2 (Moller-Plesset Perturbation Theory) method and cc-pVTZ basis set were used to calculate the structures, energies of the conformational minima, and the energy barrier between these conformations for cyclic silans and 247TOO. The CCSD (single and double excitations) method and cc-pVTZ basis set were utilized to determine the structures of 1,3-disilacyclopent-4-ene, 1,3-disilacyclopentane, 1,1,3,3-tetrachloro-1,3-disilacyclopent-4-ene, and 1,1,3,3-tetrachloro-1,3-disilacyclopentane. The theoretical calculations were carried out using Gaussian 03 and 09 packages [18,19]. The infrared and Raman spectra were recorded and compared to predicted spectra from DFT calculations.

Potential Energy Function

In 1945 R. P. Bell reported that ring-puckering four-membered ring vibration was expressed using a quartic oscillator function [20]. This function is shown in Equation (2.1).

$$V = ax^4 \tag{2.1}$$

For a number of decades the potential energy surfaces for large-amplitude motions have been reported in Jaan Laane's laboratory [1-2,21-25].

$$V = ax^4 + bx^2 \qquad (2.2)$$

Equation (2.2) is a one dimensional potential energy function and a and b are potential energy parameters. x is the vibrational coordinate such as ring-bending and ring-twisting based on high-low frequency separation. The sign of the parameter b determines the geometry of the molecule. The conformation of the ring is planar when b is positive and has a single-minimum. If b is negative, the ring has a double-minimum.

The vibrational frequencies of the ring-puckering and ring-twisting motions were calculated using the DA1OPTN program [26]. The VNCOSPX program was used to calculate the pseudorotational frequencies [27]. The energy levels of the 2D potential energy surface were carried out using the Meinander-Laane DA2OPTN4 program [28].

CHAPTER III

EXPERIMENTAL METHODS

Infrared and Raman spectroscopy were utilized in this work. These techniques will be generally described in this section. The more specific procedures used for individual molecules will be discussed in the related chapters.

Infrared Spectra

The liquid mid-infrared spectra of squalene and 247TOO were recorded on a Bruker Vertex 70 FT spectrometer equipped with a globar light source, a KBr beamsplitter and deuterated lanthanum triglycine sulfate (DLaTGS) detector. Two polished KBr windows that have 25 mm diameter and 4 mm thickness were used to hold the liquid samples. The spectra were collected with 0.5 cm^{-1} resolution and 512 scans.

Raman Spectra

A Jobin–Yvon U-1000 spectrometer (Instrument S. A., Edison, NJ) equipped with a liquid nitrogen-cooled charged-coupled device (CCD) detector was used to record the vapor and liquid Raman spectra. A Coherent Verdi-V10 laser operating at 532 nm was used and typically operated at 6 W of power for vapor-phase samples and 0.5 to 2 W of power for liquid-phase samples. For the vapor samples, a homemade single-pass gas cell was used to contain 300 torr of the samples, achieved by heating the liquid

sample to 200 ℃. Spectra of the liquid samples were recorded using a quartz cuvette. The resolution was 0.7 cm^{-1}.

VIBRATIONAL SPECTRA, THEORETICAL CALCULATIONS AND

TWO-DIMENSIONAL POTENTIAL ENERGY SURFACE FOR

THE RING-PUCKERING VIBRATIONS OF

2,4,7-TRIOXA(3.3.0)OCTANE

Introduction

For a number of decades both experimental and theoretical investigations of vibrational potential energy surfaces (PESs) for large-amplitude motions have been reported by Laane [1-3]. For several of those studies our focus has been on determining two-dimensional PESs for bicyclic molecules in order to better understand how the two rings interact. In 2004 the study of bicyclo[3.3.0]oct-1,5-ene (BCO) [29] has been presented and showed that its PES could be represented by a function of the

BCO   SSH   CEK   247TOO
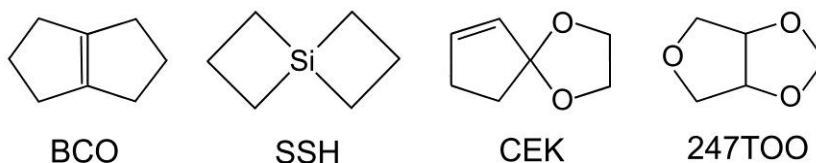
form

$$V = a(x_1{}^4 + x_2{}^4) + b(x_1{}^2 + x_2{}^2) + cx_1{}^2x_2{}^2 + dx_1x_2 \qquad (4.1)$$

where x_1 and x_2 are the ring-puckering coordinates of the two rings and a, b, c, and d are potential energy parameters which are determined so that they best fit the two different conformational energies and energy barriers found from *ab initio* calculates. The complex nature of the ring-puckering quantum states and the resulting spectra were

analyzed in detail. More recently we have reported the two-dimensional PES for the two ring-puckering vibrations of 4-silaspiro(3,3)heptane (SSH) [30]. The calculated quantum states, wavefunctions, and predicted spectra were reported. For SSH the PES has the form of Eq. (4.1) but does not require the x_1x_2 term. Recently the PES for two out-of-plane ring vibrations of 2-cyclopenten-1-one ethylene ketal (CEK) [31] has also been calculated and its energy levels and wavefunctions have been analyzed. The two-dimensional PES for CEK has two pairs of energy minima at two different conformational energies. In the present study the results for 2,4,7-trioxa[3.3.0] octane (247TOO) have been presented. The infrared and Raman spectra have been recorded and compared to predicted spectra from DFT calculations. *Ab* initio calculations were used to calculate the structures and energies of the four conformational minima and the energy barriers between these conformations. A PES in terms of the two ring-puckering coordinates was then calculated and the corresponding energy levels and wavefunctions were determined. This molecule is of particular interest since the anomeric effect is expected to cause puckering of the ring with two oxygen atoms (this labeled the β ring) and torsional forces are expected to pucker the ring with the single oxygen (the α ring).

Experimental

2,4,7-Trioxa(3.3.0)octane was prepared at the University of Texas-Pan American through a ring-closure condensation reaction of anhydroerythritol and paraformaldehyde [32]. At the time of the synthesis, there was no mention in the chemical literature of this compound having been prepared. In a 500-mL three-necked flask, anhydroerythritol

(Aldrich, 0.25 moles) was dissolved in 150-mL of dry benzene. The flask was charged with 15-g of paraformaldehyde and a Dean-Stark trap was used to remove water over a four-hour period. The reaction contents were mixed in a separatory funnel with three successive 150-mL portions of 5% Na_2CO_3 and then with 150-mL portions of saturated NaCl and water. After overnight drying over anhydrous $MgSO_4$, the mixture was concentrated via a 10-inch Vigreux column and distilled under vacuum (b.p 105°-115°). The 2,4,7-trioxa(3.3.0)octane was characterized by C-13 and H-1 NMR spectrometry. Raman spectra were recorded at right angle scattering geometry using an Jobin Yvon U-1000 monochromator equipped with 1800 groves mm^{-1} holographic grating and CCD detection. The resolution was 0.7 cm^{-1}. A Coherent Verdi-V10 laser operating at 532 nm was used and typically operated at 6 W of power for vapor-phase samples and 0.5 W of power for liquid-phase samples. For the vapor sample a homemade single-pass gas cell [33,34] was used to contain 300 torr of the 247TOO, achieved by heating the liquid sample to 200 ℃. Spectra of the liquid were obtained of the sample contained and a quartz cuvette. The liquid mid-infrared spectrum of 247TOO was recorded on a Bruker Vertex 70 FT spectrometer equipped with a globar light source, a KBr beamsplitter and deuterated lanthanum triglycine sulfate (DLaTGS) detector.

Theoretical Calculations

Density functional theory (DFT) computations for calculating the infrared and Raman spectra were carried out using the GAUSSIAN 09 package [19] and the B3LYP/cc-pVTZ method and basis set. Scaling factors of 0.985 for frequencies below

2000 cm^{-1} and 0.961 for the higher frequencies were used. *Ab initio* computations with MP2/cc-pVTZ were used to calculate the conformational structures and potential energy surface. The Meinander-Laane DA2OPTN4 program [28] was used to calculate the ring-puckering energy levels and wavefunctions. The calculated wavefunctions were obtained by Meinander.

Results and Discussion

1. Structure

Figure 1 shows the calculated structure and geometrical parameters of 247TOO in its lowest energy conformation which we label structure A. Both rings are puckered up and the dihedral angles of puckering are 41.9 ° for the α ring with the single oxygen and 36.0 ° for the β ring. The molecule also has three additional conformational energy minima resulting from whether the two rings pucker up or down relative to each other, and structures are labeled as B, C, and D in order of increasing energy. Figure 2 shows all four conformations along with their calculated relative energies and puckering angles. The bond distances and angles differ little from one structure to another and these are shown in Table 1. The puckering of the α ring results from the torsional strain between the CH$_2$ group and H-C-O grouping on the bridgehead carbon atom. This can be seen in Figure 3 which shows that eclipsing would result if this ring were planar. The puckering of the β ring is brought about by the anomeric effect due to the O-C-O bonding configuration. This result has been observed previously and discussed in some detail in

12
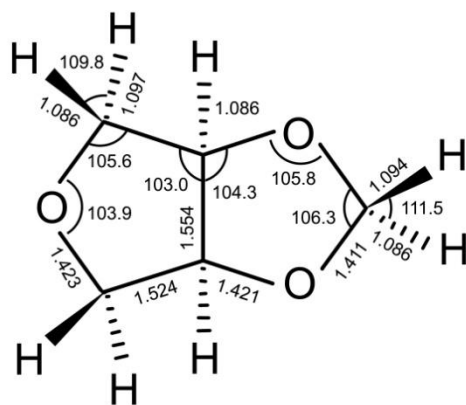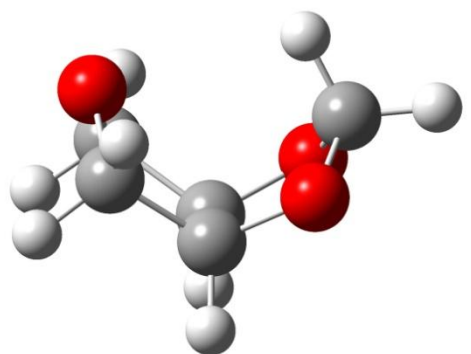
Figure 1. Geometrical parameters and structure of 247TOO in its lowest energy conformation.

	A	**B**	**C**	**D**
E (cm^{-1})	0	189	797	1130
τ_α , τ_β	+41.8°, +36.5°	+41.3°, -39.5°	-40.7°, +38.7°	-41.1°, -39.1°
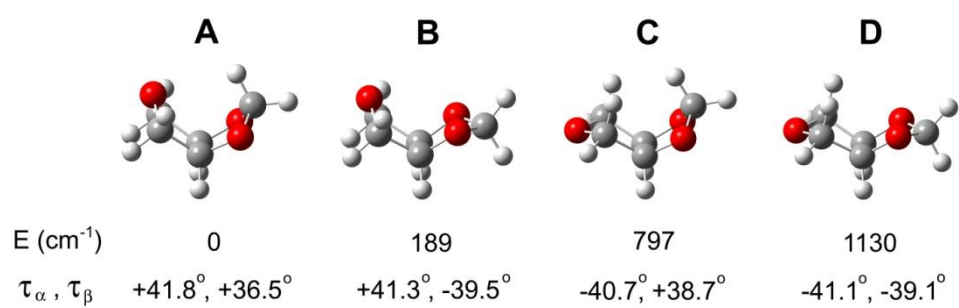
Figure 2. Conformational minima and relative conformational energies (cm^{-1}) of 247TOO.

Parameter	A	B	C	D
α ring				
C-C	1.524	1.519	1.527	1.532
C-O	1.423	1.420	1.422	1.422
C-H (CH$_2$)	1.086/1.097	1.086/1.067	1.085/1.095	1.092/1.096
∠CCO	105.6	105.5	105.0	105.5
∠COC	103.9	104.4	105.0	105.0
∠CCC	103.0	103.2	103.2	103.3
∠HCH	109.8	109.9	109.9	109.2
Puckering angle	41.9	41.5	40.5	41.1
Bridged C-C	1.554	1.550	1.550	1.550
C-H (CH)	1.086	1.091	1.090	1.085
β ring				
C-O	1.421	1.423	1.423	1.421
O-CH$_2$	1.411	1.406	1.410	1.410
C-H (CH$_2$)	1.086/1.094	1.086/1.098	1.086/1.098	1.085/1.097
∠CCO	104.3	104.2	104.7	104.5
∠COC	105.8	105.0	104.7	104.6
∠OCO	106.3	106.4	106.5	106.6
∠HCH	111.5	111.2	111.1	110.8
Puckering angle	36.0	38.4	38.7	39.1
Conformational energy (cm^{-1})	0	189	797	1130

Table 1. Bond distances (Å) and angles (degrees) calculated for the four conformations of 247TOO.
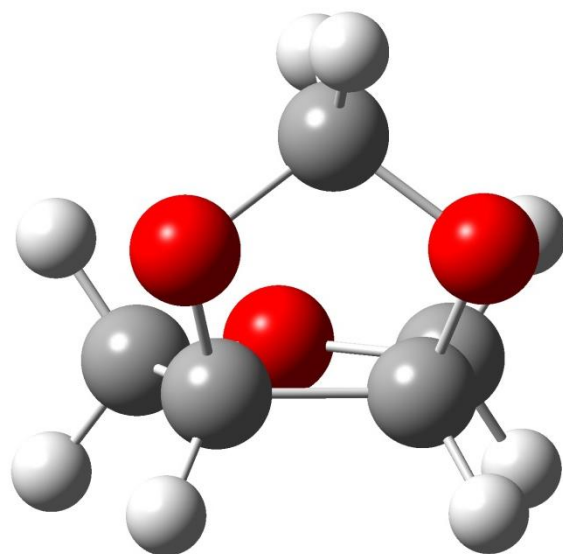
Figure 3. Eclipsing of the CH$_2$ and H-C-O groups when the α ring is planar.

the studies of 1,3-dioxole [35] and 1,3-benzodioxole [36]. While the puckering of each ring is readily understood, the reasons for the conformational energy differences between A, B, C, and D are less clear.

2. NMR Spectra

The C-13 NMR spectrum shows three types of carbon atoms with chemical shifts at 96 ppm, 80 ppm and 73 ppm. The H-1 NMR spectrum shows five signals; 5.0 ppm (1-proton), 4.8 ppm (1-proton), 4.7 ppm (2-protons), 4.1 (2-protons) and 3.4 ppm (2 protons). The data support a bicyclic ring system in which the two protons of each of the methylene groups are not equivalent due to the conformations of the two rings and of the bicyclic system, in general. The chemical shifts of the methylene groups and of the bridgehead hydrogens are consistent with those in the literature for similar groups (1,3-dioxolane, tetrahydrofuran, and 9-oxabicyclo(6.1.0)nonane). Significantly, each of the nmr peaks shows up as a closely spaced doublet, indicating that two different conformers have significant abundance in the liquid at room temperature. These clearly arise from conformers A and B which are calculated to be 181 cm^{-1} apart in conformational energy. Conformations C and D, which are calculated to be 745 and 1148 cm^{-1} higher in energy, were not observed in the nmr spectra.

3. Vibrational Spectra

Figure 4 shows the infrared spectrum of liquid 247TOO and compares it to the calculated spectra of the four conformers. Figure 5 compares the observed Raman

17
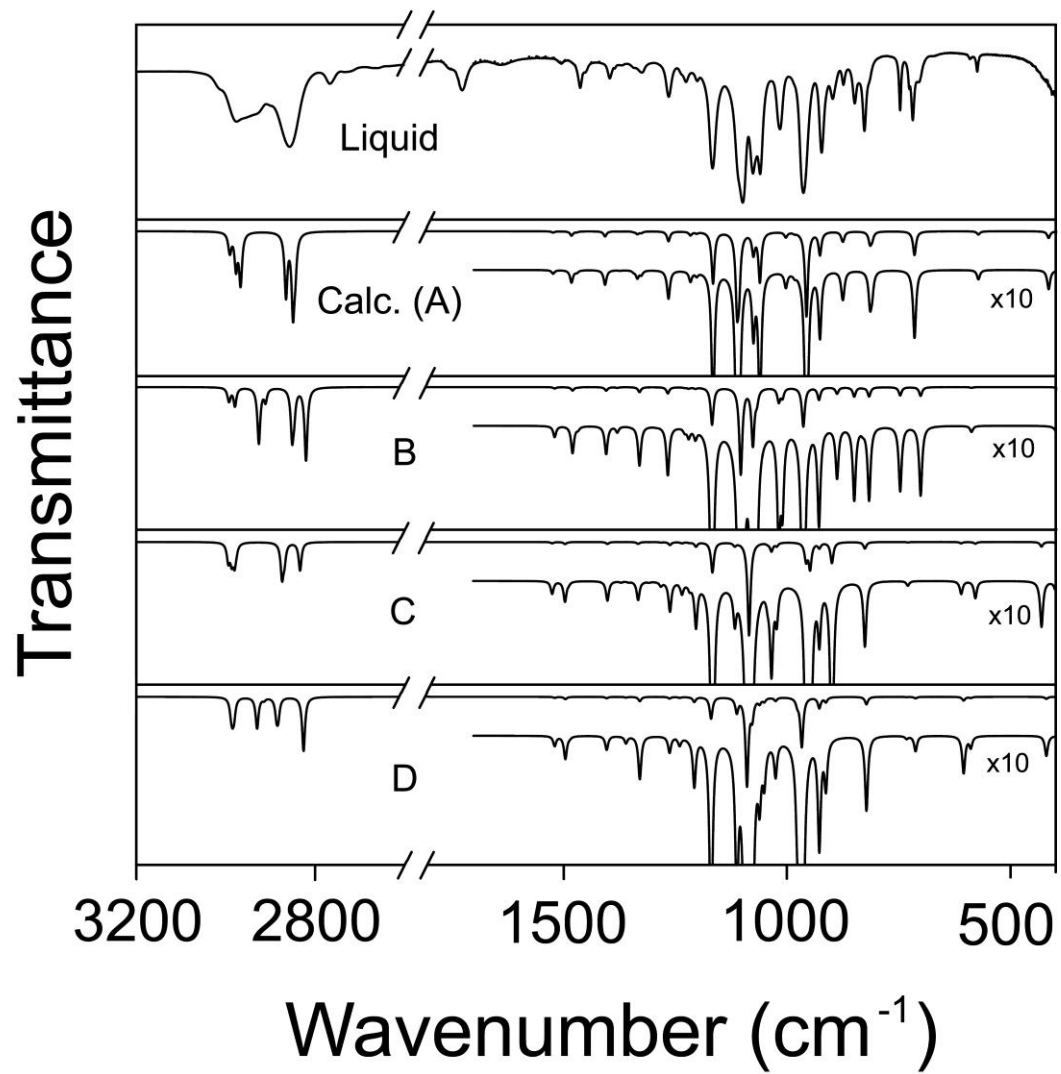
Figure 4. Observed and calculated infrared spectra of 247TOO for its four conformations.
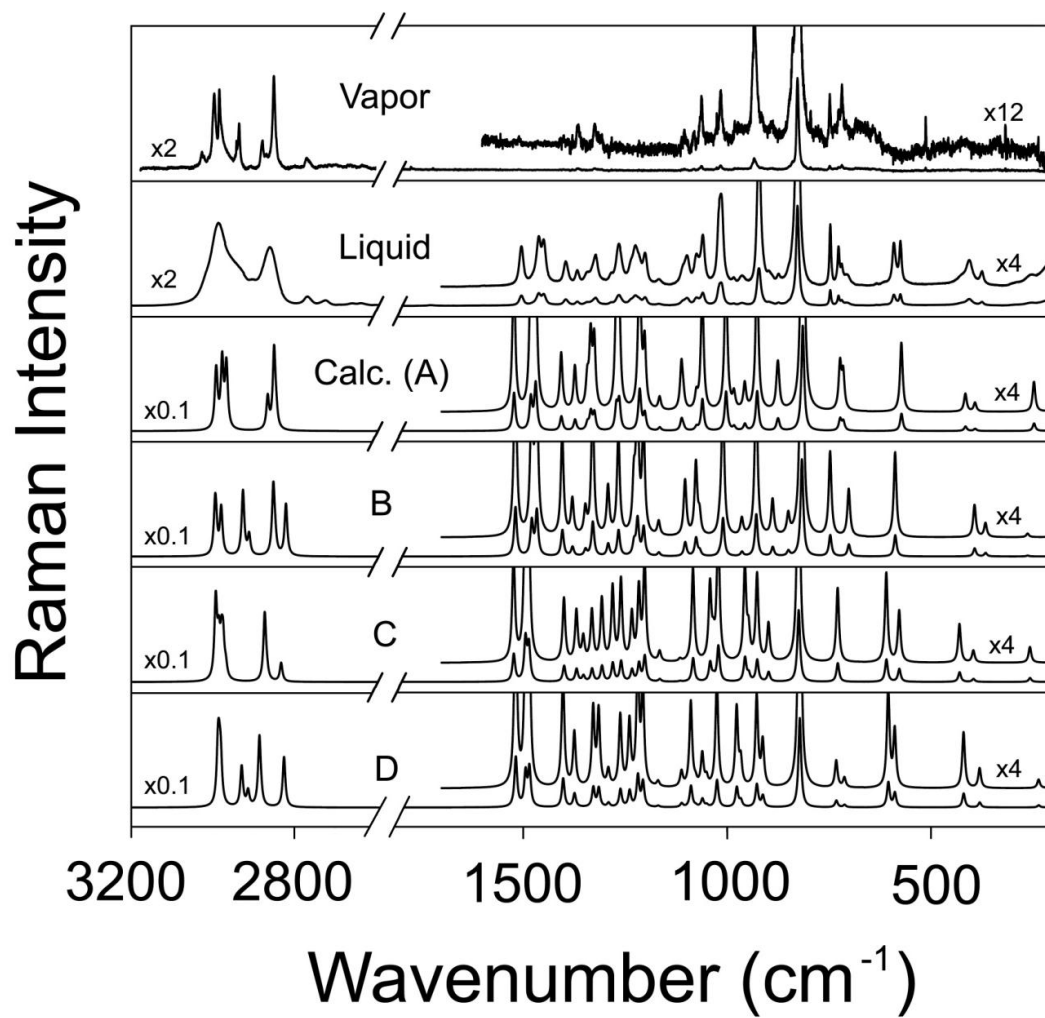
Figure 5. Observed and calculated Raman spectra of 247TOO for its four conformations.

spectra of the vapor and liquid to the calculated spectrum. As can be seen, the observed spectra agree quite well with that of structure A which is the predominant one in the sample. This molecule has C_s symmetry with the plane of symmetry passing through the oxygen atom of the α ring and the CH_2 group of the β ring. With Cs symmetry the molecule has $23A' + 19A''$ modes. Visualizing and assigning the vibrations are facilitated if we assume the molecule takes on a totally planar skeletal structure and has C_{2v} symmetry. The vibrations are then distributed as

$$\Gamma = 14A_1 + 7A_2 + 12B_1 + 9B_2 \tag{4.2}$$

where the A_1 and B_2 are in actuality A' modes and A_2 and B_2 are the A'' modes. Utilizing the C_{2v} approximation, however, allows to distinguish the A_1 and B_1 in-plane ring modes from the A_2 and B_2 out-of-plane modes. Table 2 presents a listing of the observed infrared and Raman bands according to C_{2v} symmetry and compares these to the calculated frequencies and intensities for all conformations of the molecule. The primary interests are the low frequency modes of 247TOO. The vibration of lowest frequency is the skeletal twisting motion where the two rings twist in opposite directions. This is calculated to be at 92 cm^{-1}. The next two lowest frequency vibrations are the ring-puckering motions calculated to be at 198 and 247 cm^{-1} for a vapor sample. Although we have not observed these in the vapor spectrum, they appear in the liquid spectra at 205 and 249 cm^{-1}. The lower frequency results from both rings puckering in phase (this labeled υ_+) while the higher frequency (υ_-) has both the β and α rings puckering in opposite directions. In this study the potential energy surface was focused

20

	Description[a]	Infrared (liquid)[b]	Raman (vapor)[c]	Raman (liquid)[c]	A Calculated[d]	B Calculated[d]	C Calculated[d]	D Calculated[d]
					2,4,7-trioxa(3.3.0)-octane			
A_1 (A')	C-H sym. Str.	2977 (m, br)	2983 (51)	2986(41, br)	2978 (41, 1101)	2926 (98, 1129)	2975 (8, 889)	3003 (36, 768)
	CH$_2$ sym. Str. (β)	2858 (s, br)	2877 (16)	2861(29, br)	2866 (74, 505)	2821 (100, 882)	2833 (45, 428)	2896 (62, 931)
	CH$_2$ sym. Str. (i.p.) (α)	2858 (s, br)	2850 (51)	2861 (9, br)	2850 (92, 1260)	2852 (84, 1198)	2873 (54, 1577)	2958 (20, 1278)
	CH$_2$ deformation (β)	1504 (vvw)		1505 (9)	1523 (1, 42)	1519 (2, 60)	1523 (2, 45)	1518 (1, 66)
	CH$_2$ deformation (i.p.) (α)	1504 (vvw)		1462 (12)	1481 (5, 35)	1479 (6, 41)	1495 (3, 68)	1495 (3, 43)
	CH$_2$ wag (i.p.) (α)	1396 (vw)	1365 (2)	1368 (3)	1373 (0.2, 12)	1379 (1, 11)	1369 (0.2, 20)	1374 (0, 17)
	C-H wag (i.p.)	1226 (vw)		1225 (10)	1216 (4, 10)	1228 (1, 14)	1233 (2, 18)	1239 (1, 20)
	Ring str. (i.p.)	1060 (s)	1063 (4)	1060 (12)	1060 (59, 32)	1076 (100, 20)	1083 (100, 28)	1089 (100, 26)
	Ring str. (i.p.)	1016 (m)	1015 (5)	1015 (22)	1002 (6, 39)	1010 (16, 41)	1021 (5, 51)	976 (4, 32)
	Ring str. (i.p.)	922 (ms)	933 (13)	922 (37)	926 (27, 38)	928 (22, 45)	956 (27, 34)	926 (12, 26)
	Ring str. (i.p.)	874 (vw)		873 (2)	874 (7, 7)	888 (11, 9)	824 (10, 100)	821 (8, 100)
	Ring str. (i.p.)	827 (ms)	827 (100)	827 (100)	814 (13, 100)	816 (16, 100)	926 (8, 31)	966 (7, 23)
	Ring bending		748 (5)	727 (9)	722 (0.2, 11)	747 (15, 21)	728 (1, 20)	732 (0.3, 7)
	Ring bending	719 (ms)	718 (6)	719 (5)	715 (28, 8)	701 (16, 12)	609 (2, 30)	604 (4, 27)
A_2 (A'')	CH$_2$ antisym. Str. (o.p.) (α)	2977 (m, br)	2996 (40)	2986(41, br)	2991 (18, 376)	2993 (19, 423)	2986 (27, 875)	3059 (18, 630)
	C-H wag (o.p.)				1343 (1, 7)	1347 (0, 7)	1352 (0.1, 9)	1359 (1, 0)
	CH$_2$ twist (β)	1226 (vw)		1225 (10)	1214 (0.1, 33)	1220 (2, 41)	1216 (1, 27)	1219 (0.1, 38)
	CH$_2$ twist (o.p.) (α)	1200 (vw)		1201 (8)	1202 (2, 17)	1205 (2, 32)	1202 (7, 39)	1206 (6, 30)
	CH$_2$ rock (o.p.) (α)			983 (1)	983 (1, 4)	1067 (19, 5)	1115 (5, 1)	1077 (21, 1)
	Ring twist			375 (3)	391 (1, 2)	366 (2, 3)	395 (3, 4)	380 (0.2, 5)
	Ring twist				92 (1, 2)	98 (1, 2)	87 (0.1, 5)	35 (1, 2)

Table 2. Observed and calculated infrared and Raman spectra for 247TOO.

		2,4,7-trioxa(3.3.0)-octane			A	B	C	D
	Description[a]	Infrared (liquid)[b]	Raman (vapor)[c]	Raman (liquid)[c]	Calculated[d]	Calculated[d]	Calculated[d]	Calculated[d]
B$_1$ (A")	CH$_2$ sym. Str. (o.p.) (α)	2977 (m, br)	2996 (40)	2986(41, br)	2993 (6, 671)	2995 (6, 734)	2993 (29, 1919)	3062 (13, 1025)
	C-H antisym. Str.	2977 (m, br)	2983 (51)	2986(41, br)	2966 (12, 302)	2911 (23, 349)	2968 (0.1, 269)	2987 (3, 287)
	CH$_2$ deformation (o.p.) (α)	1462 (w)		1450 (11)	1470 (1, 51)	1467 (1, 53)	1486 (0.3, 57)	1485 (0.1, 50)
	CH$_2$ wag (β)	1396 (vw)		1396 (5)	1407 (6, 15)	1404 (6, 31)	1400 (3, 25)	1402 (2, 37)
	CH$_2$ wag (o.p.) (α)	1324 (vw)		1322 (7)	1325 (2, 18)	1329 (1, 12)	1307 (0.1, 24)	1315 (0, 24)
	C-H wag (o.p.)	1264 (w)		1266 (10)	1272 (0.1, 25)	1292 (0, 14)	1280 (1, 29)	1291 (0, 5)
	Ring str. (o.p.)	1099 (vs)	1105 (2)	1099 (6)	1107 (56, 3)	1104 (84, 3)	1083 (48, 7)	1111 (16, 5)
	Ring str. (o.p.)	1076 (s)		1075 (7)	1075 (24, 4)	1018 (24, 2)	1033 (14, 6)	1025 (4, 2)
	Ring str. (o.p.)	963 (vs)		963 (2)	956 (100, 6)	963 (69, 4)	947 (41, 10)	927 (57, 7)
	Ring bending	874 (vw)		873 (2)	876 (6, 5)	830 (1, 0.2)	728 (0, 5)	912 (5, 13)
	Ring str. (o.p.)				810 (8, 0.3)	850 (16, 5)	898 (33, 11)	712 (2, 3)
	Skeletal bend	574 (w)		575 (11)	572 (4, 16)	587 (1, 21)	577 (3, 17)	588 (1, 15)
B$_2$ (A')	CH$_2$ antisym. Str. (β)	2977 (m, br)	2983 (44)	2986(41, br)	2967 (50, 774)	2980 (32, 830)	2979 (32, 770)	3055 (18, 807)
	CH$_2$ antisym. Str. (i.p.) (α)	2858 (s, br)	2850 (51)	2861(29, br)	2845 (35, 207)	2847 (36, 214)	2868 (25, 160)	2954 (20, 112)
	C-H wag (i.p.)				1334 (3, 19)	1330 (8, 28)	1331 (3, 20)	1328 (5, 25)
	CH$_2$ twist (i.p.) (α)	1264 (w)		1266 (10)	1265 (12, 30)	1266 (11, 30)	1260 (5, 31)	1262 (2, 22)
	CH$_2$ rock (β)	1166 (s)		1168 (1)	1165 (61, 3)	1167 (66, 4)	1165 (48, 4)	1169 (25, 2)
	CH$_2$ rock (i.p.) (α)	1099 (vs)		1099 (6)	1112 (80, 12)	1102 (72, 13)	1041 (2, 27)	1060 (6, 10)
	Ring flap			406 (5)	415 (8, 4)	393 (5, 8)	429 (7, 12)	419 (2, 14)
	Ring puckering (o.p.)			249 (2)	247 (5, 6)	262 (8, 1)	257 (11, 5)	235 (8, 2)
	Ring puckering (i.p.)			205 (5)	198 (7, 3)	181 (3, 4)	175 (2, 4)	193 (1, 3)

[a] i.p.-in phase; o.p.-out of phase; $\alpha-\alpha$ ring; $\beta-\beta$ ring
[b] s-strong; m-medium; w-weak; v-very; br-broad
[c] Relative intensities; br-broad
[d] The frequency and relative intensities (IR, Raman) were calculated using the B3LYP/cc-pVTZ basis set. The scaling factor 0.985 was used for frequencies below 2000 cm^{-1} and 0.961 for above.

Table 2. Continued.

since they determine the conformations of the molecules.

4. Potential Energy Surface (PES)

Figure 2 shows the four conformations and their relative energies calculated for 247TOO. Each conformation can be defined in terms of its ring-puckering coordinates x_1 and x_2 which are defined in Figure 6. *Ab initio* calculations provided the energy and x_1 and x_2 coordinate values for each of the minima as well as for the four barriers between the minima. In addition, the central barrier value of 3141 cm^{-1} at $x_1 = x_2 = 0$ has been calculated. These twenty-five data points have allowed us to calculate a potential energy surface that fits all of the values from the *ab initio* computations quite closely. In particular, the potential energy parameters were chosen so that the data at lower energies would be well fit. The function determined, which at first glance looks excessively complicated, is

$$
\begin{aligned}
V\ (\text{cm}^{-1}) = {} & 6.324\text{x}10^5\ x_1{}^4 + 2.250\text{x}10^4\ x_1{}^3 - 6.551\text{x}10^4\ x_1{}^2 \\
& + 1.781\text{x}10^6\ x_2{}^4 + 2.766\text{x}10^4\ x_2{}^3 - 9.851\text{x}10^4\ x_2{}^2 \\
& + 3.223\text{x}10^5\ x_1{}^2\ x_2{}^2 - 4.809\text{x}10^3\ x_1{}^3\ x_2 + 4.443\text{x}10^4\ x_1\ x_2{}^3 \\
& - 3.116\text{x}10^3\ x_1 - 1.589\text{x}10^3\ x_2 + 2.001\text{x}10^3\ x_1\ x_2 \\
& + 1.309\text{x}10^5\ x_1{}^6 + 1.039\text{x}10^4\ x_1{}^5 - 9.946\text{x}10^4\ x_2{}^6 \\
& - 8.653\text{x}10^4\ x_2{}^5 + 9.827\text{x}10^6\ x_1{}^4\ x_2{}^2 - 1.391\text{x}10^7\ x_1{}^2\ x_2{}^4 \\
& - 3.136\text{x}10^5\ x_1{}^3\ x_2{}^3 + 9.684\text{x}10^5\ x_1{}^5\ x_2 + 8.336\text{x}10^4\ x_1\ x_2{}^2 \\
& + 3141
\end{aligned}
\tag{4.3}
$$

The puckering coordinates are in Ångstrom units. A large number of terms, above and beyond those used in Eq. (4.1), were required to reproduce the conformational energies of this highly asymmetric PES. In Eq. (4.1) no terms above fourth order were utilized,
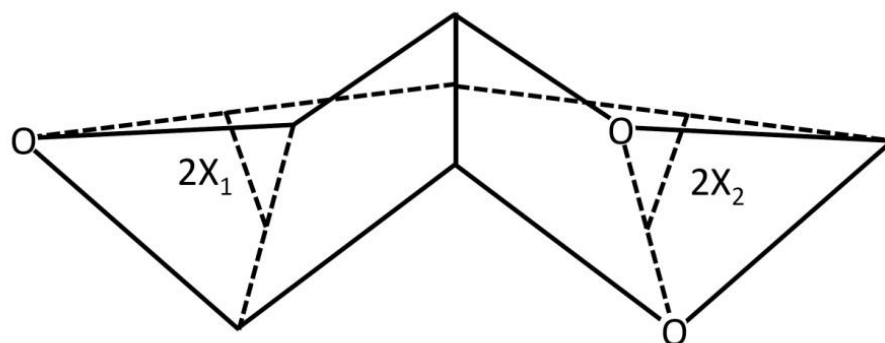
Figure 6. Definition of the ring-puckering coordinates x_1 and x_2 for the α and β rings, respectively. Each coordinate is half the distance between two ring diagonals.

but Eq. (4.3) also uses sixth power terms and this may seem troublesome. However, these higher power terms have been used to tweak the PES only somewhat and have considerably smaller contributions than it might seem. For example, the x_1^6 term contributes about forty times less at the energy minima than the x_1^4 term since its coefficient is about eight times smaller and its value is about five times less there. Similarly, the x_2^6 term contributes about ninety times less than the x_2^4 term. Without the higher order terms, however, the overall PES would not be so well fit. Figure 7 shows the two-dimensional PES corresponding to Eq. (4.3). Having determined this PES, we were then able to use the Meinander-Laane DA2OPTN4 program [28] to calculate the energy levels for this surface. The calculations also require the utilization of the kinetic energy (reciprocal reduced mass) terms. The realistic estimates of these were made by choosing their values so that our program reproduces the ring-puckering frequencies calculated by the DFT program. The DFT frequencies are calculated based on the harmonic approximation and it is well known that deep within a potential well the harmonic oscillator approximation works quite well for predicting frequencies [37].

Figure 8 shows the calculated energy levels for the PES of Eq. (4.3). The lowest quantum states are isolated in the potential energy wells for structures A and B with those for the latter starting 181 cm^{-1} higher. The vibrational excited states can be described by the number of quanta for each puckering motion (v_-, v_+), and they are also labeled sequentially starting at 0. Thus, the lowest ring-puckering level is (0,0) or 0 and corresponds to structure A. The next level (0,1) or 1 corresponds to structure B and lies 181 cm^{-1} higher in energy. In the figure the levels for structures A, B, C, and D are
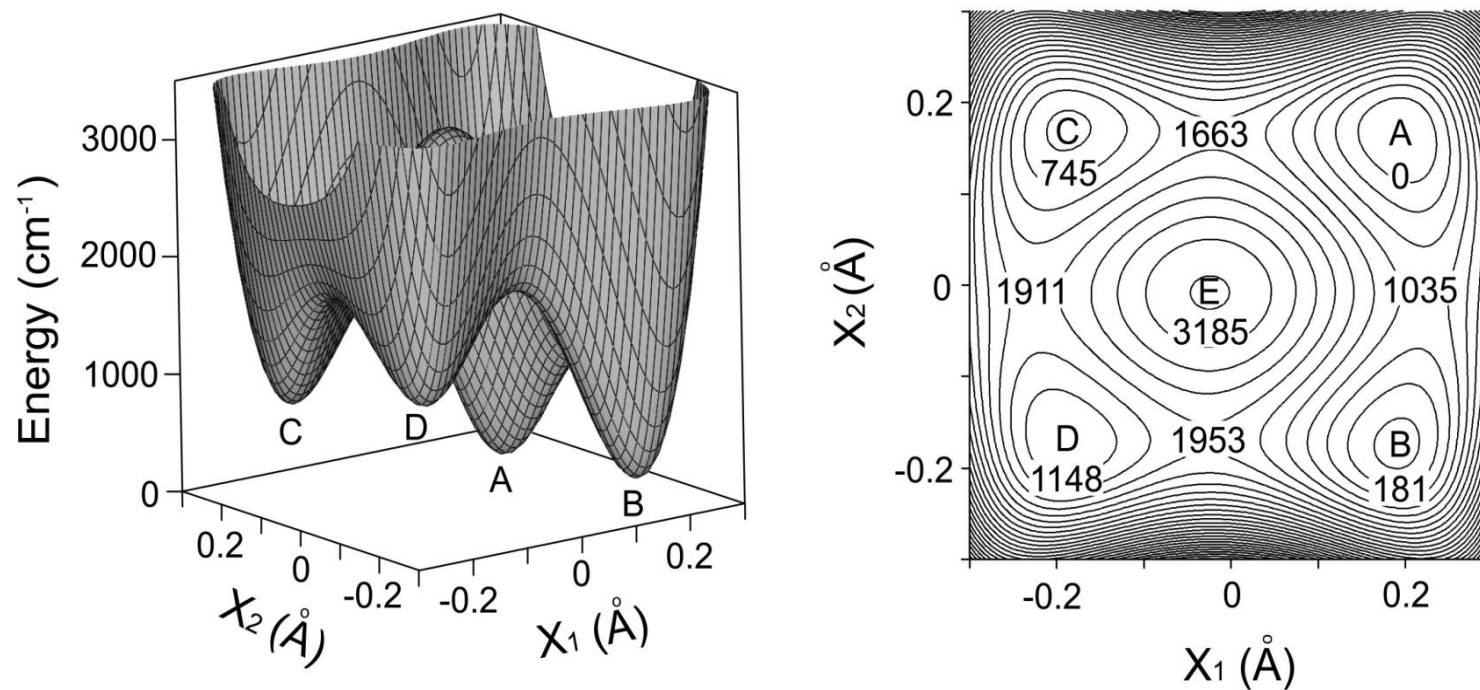
Figure 7. PES corresponding to Eq. (4.3) for 247TOO. The conformational energies (cm^{-1}) for the energy minima and barriers are also shown.
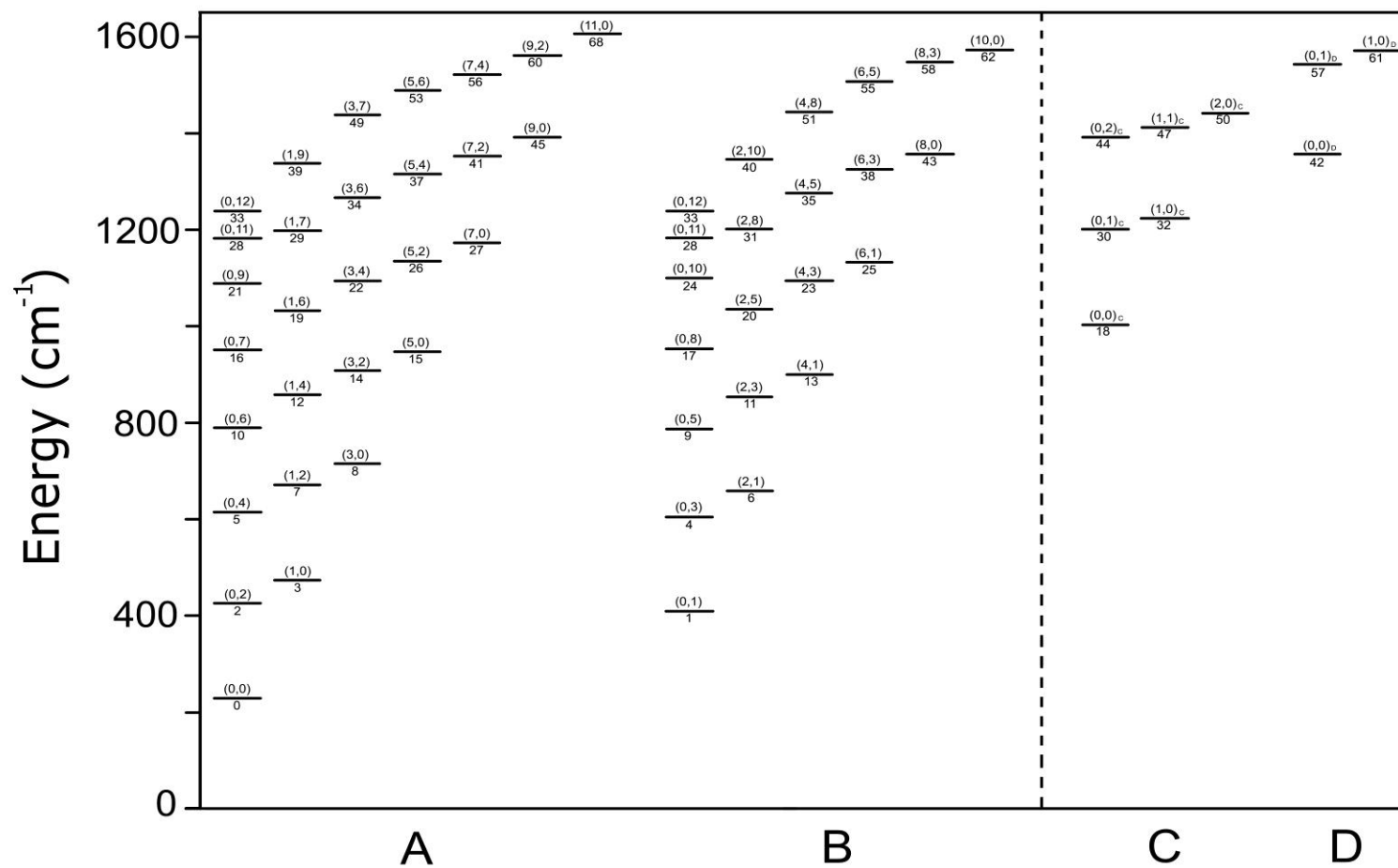
Figure 8. Energy levels calculated for the different conformations of 247TOO. The levels are labeled sequentially and also according to (v_-, v_+) format.

27

shown separately since at lower energies each level is isolated in one well or another. The complete listing of the lowest 100 calculated energy levels is available in the supplementary material. The energy levels in Figure 8 are shown so that those for υ_+ with the lower puckering frequency are in a vertical column. Those for υ_- are shown progressing to the right. Thus, the lowest puckering transition for structure A is for υ_+ and is $(0,0) \rightarrow (0,2)$ or $0 \rightarrow 2$ for the sequential levels. For structure B the lowest puckering transition is $(0,1) \rightarrow (0,3)$ or $1 \rightarrow 4$. The corresponding transitions for the υ_- puckering are $(0,0) \rightarrow (1,0)$ or $0 \rightarrow 3$ for structure A and $(0,1) \rightarrow (2,1)$ or $1 \rightarrow 6$ for structure B. Most of the levels shown represent states for which both puckering motions have been excited at the same time. The (v_-, v_+) labels can become confusing since the lowest energy level $(0,0)$ corresponds to structure A while the next one $(0,1)$ corresponds to structure B. Figures 9 and 10 show one-dimensional slices of the two-dimensional PES, and each shows the energy levels associated υ_+ or υ_-, respectively. The former shows the function for the puckering of ring β along x_2 while x_1 is at its minimum energy value. Figure 10 shows the potential energy curve for the α ring as a function of x_1 while x_2 is at its minimum energy value. These provide additional perspective and help to understand the distribution of the quantum states between the potential wells for structures A, B, and C. The fourth well D and its energy levels are at much higher energies as can be seen in Figures 7 and 8.

Figure 11 shows a selection of the wavefunctions calculated for the energy levels in the different wells of the PES. The supplementary material presents many more of these. The figure clearly shows that the lowest eight quantum states are clearly isolated

28
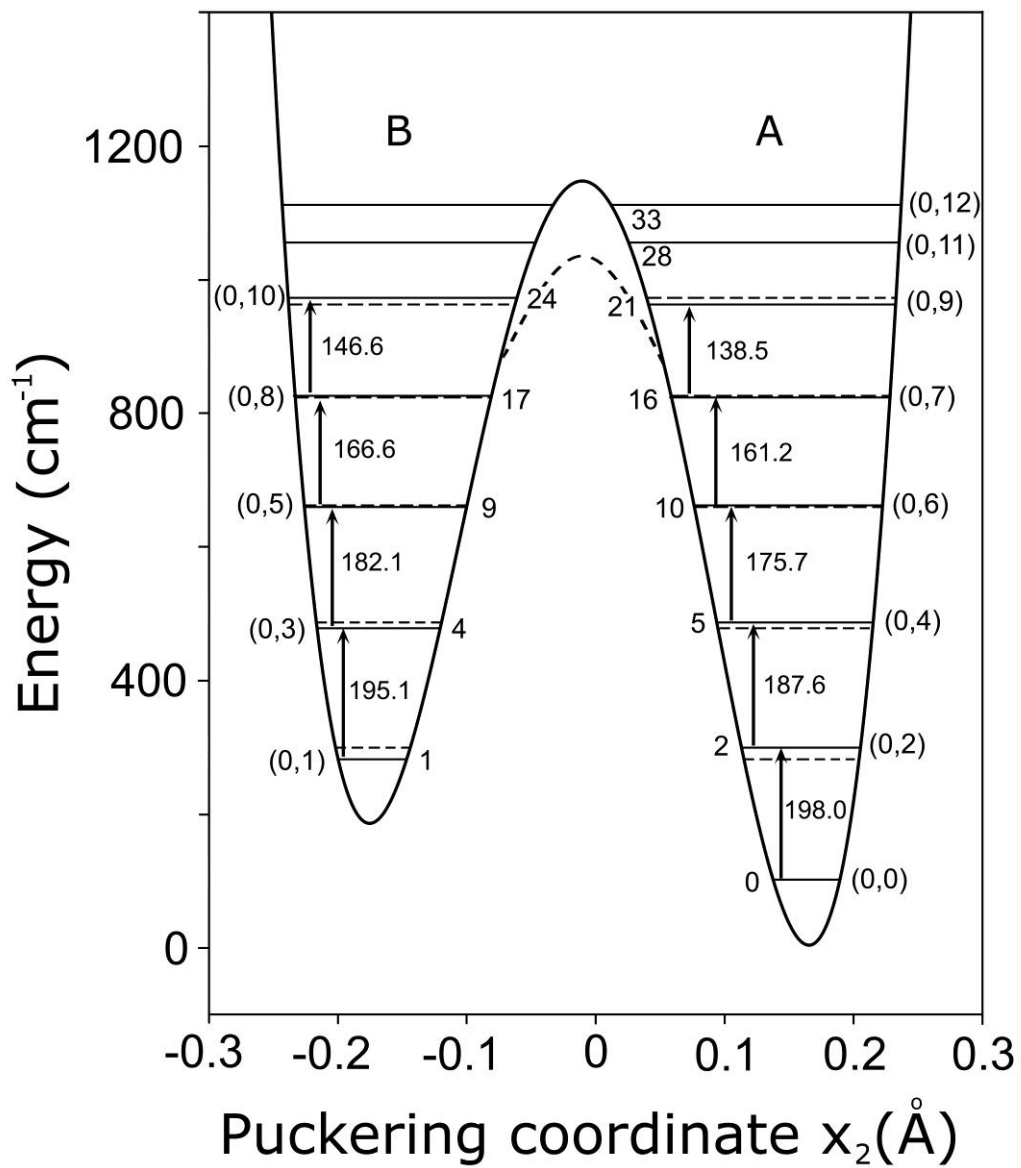
Figure 9. One-dimensional slice of the PES for 247TOO along x_2 with x_1 fixed at its energy minimum. The energy levels for ν_+ are also shown.

Figure 10. One-dimensional slice of the PES for 247TOO along x_1 with x_2 fixed at its energy minimum. Note that the levels (n,0) for n = 2, 4, 6, and 8 are within the B well. The energy levels for v_- are also shown.
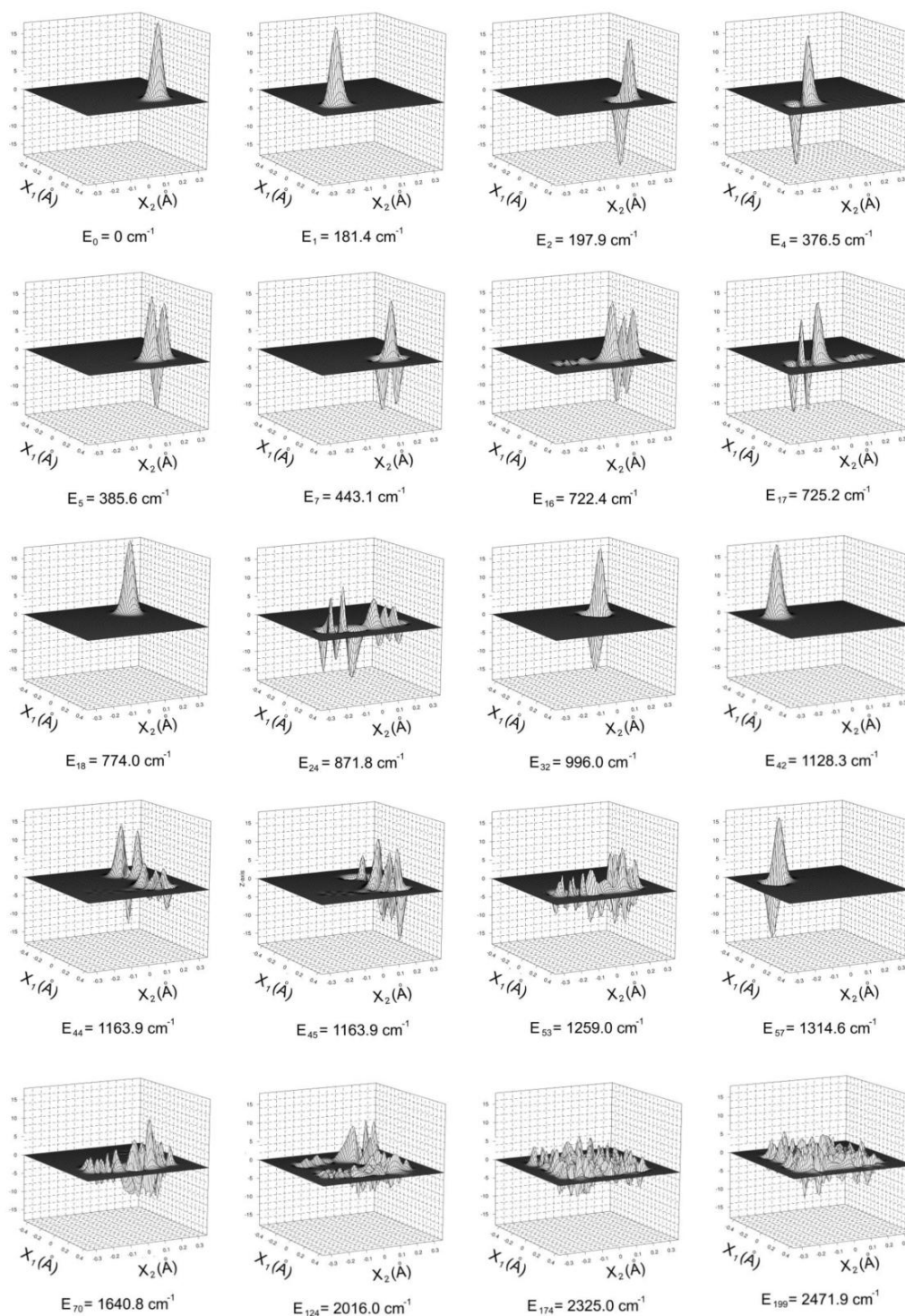
Figure 11. Selected wavefunctions calculated for the PES of 247TOO.

in either well A (levels 0, 2, 3, 5 and 7) or B (levels 1, 4, and 6). Level 9 is almost totally in B but begins to show a tiny bit of probability in well A. Higher levels begin to show progressively more and more probability in both wells. Yet higher levels wind up isolated in conformation C (18, 30, 44, 47, 50) or D (42, 57, 61). In addition to showing where the conformational probabilities lie, the wavefunctions also show the expected nodes for each of the PES wells. Level 0 is the lowest state for conformation A and level 1 is the lowest state for conformation B. Hence, neither has a node for the wavefunction. Levels 2 and 4 are the first excited vibrational levels for A and B, respectively, and each has one node. For higher levels the number of nodes increases progressively. Careful inspection of the functions also shows that there is a directionality of the functions either along x_1 or x_2 and a conformation of both. These correspond as expected based on where the levels lie in Figure 9 and 10. For the very highest levels which lie along all but the central barrier (such as 174 and 199), the conformational probability corresponds to all of the conformations (A, B, C, and D).

Conclusion

The 247TOO was synthesized for the first time and it analyzed its infrared and Raman spectra with the aid of theoretical calculations. *Ab initio* calculations provided conformational energy data for detecting the two-dimensional PES for the out-of-plane modes of the two rings. The nmr spectrum of the molecules showed the presence of the two lowest energy conformations. The energies for the quantum states corresponding to each of the four potential energy wells were calculated along with their corresponding

32

wavefunctions. The results provide a comprehensive understanding of both the energy

level patterns and the nature of the wavefunctions.

CHAPTER V

VIBRATIONAL SPECTRA, THEORETICAL CALCULATIONS AND STRUCTURES FOR 1,3-DISILACYCLOPENT-4-ENE AND 1,3-DISILACYCLOPENTANE AND THEIR TETRACHLORO DERIVATIVES[*]

Introduction

In 1991 the first preparation of 1,3-disilacyclopent-4-ene (I) and a portion of its vibrational spectra have been reported by Colegrove and Laane [4]. The aim of the project was to determine the ring-puckering potential function for the molecule to see whether it had unusual rigidity due to possible p_π-d_π bonding involving the silicon atoms. Along the way 1,3-disilacyclopentane (II), 1,1,3,3-tetrachloro-1,3-disilacyclopent-4-ene (III), and 1,1,3,3-tetrachloro-1,3-disilacyclopentane(IV) were prepared.
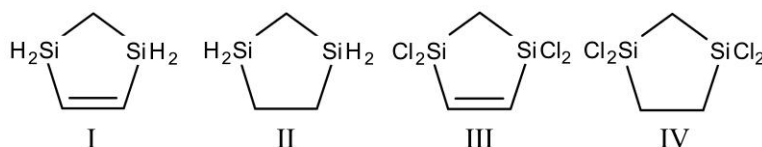
The preparation of these molecules was difficult and tedious, requiring many weeks to complete, and the final products were only obtained in small quantities. Hence, in order to conserve the samples, the samples were not reduced by additional

purification. The infrared and Raman spectra obtained therefore included bands from impurities [10]. In the present work the infrared and Raman spectra of these four molecules have been presented which were recorded more than two decades ago [10]. These studies were also complemented with *ab initio* and DFT computations which the structures of the molecules and their infrared and Raman spectra were carried out to calculate.

Experimental

The infrared and Raman spectra were recorded on Digilab FTS-60 and Cary 82 Raman instruments. The details, including the preparation methods for these molecules, have been previously described [4,10].

Computations

Density functional theory (DFT) computations for calculating the infrared and Raman spectra were carried out using the GAUSSIAN 09 package [19] and B3LYP/cc-pVTZ computation. Scaling factors of 0.961 for frequencies above 2200 cm^{-1} and 0.985 for the lower frequencies were used. *Ab initio* computations with MP2/cc-pVTZ and CCSD/cc-pVTZ were used to calculate the molecular structures.

Calculated Structures

Fig. 12 shows the calculated structures for these molecules. For comparison purposes, Fig. 13 shows the Si-C and C-C bond distances for the related molecules
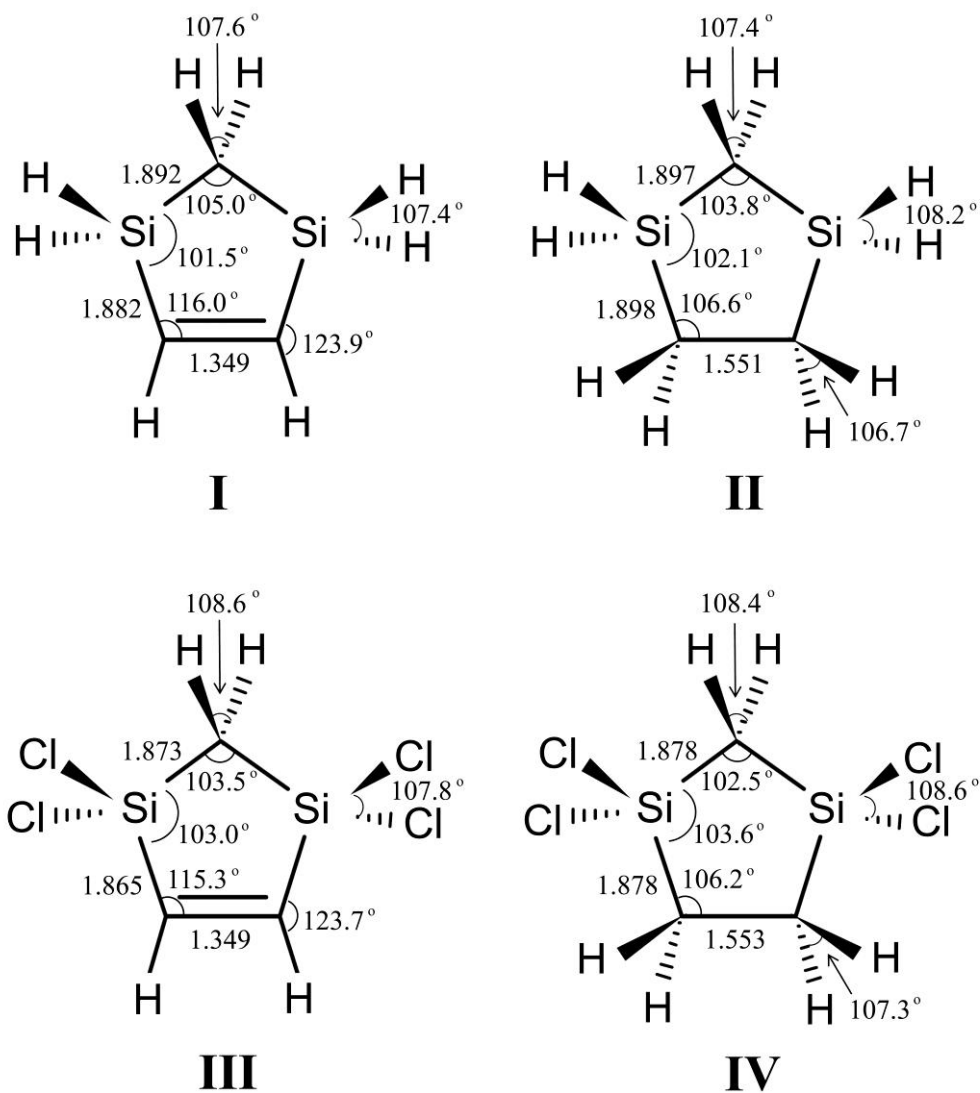
Figure 12. Calculated structures for 1,3-disilacyclopent-4-ene (I), 1,3-disilacyclopentane (II), 1,1,3,3-tetrachloro-1,3-disilacyclopent-4-ene (III), and 1,1,3,3-tetrachloro-1,3-disilacyclopentane (IV).
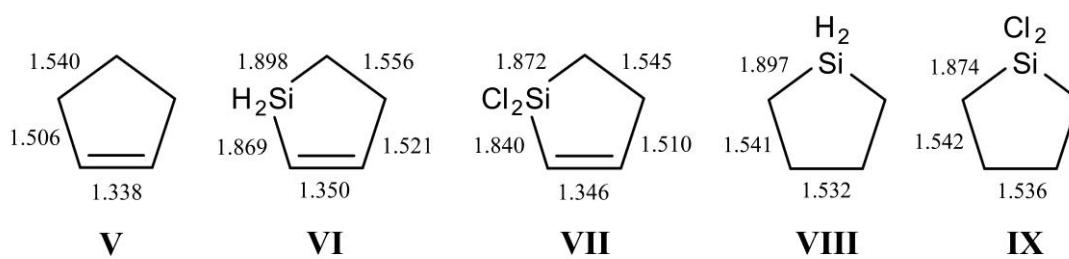
Figure 13. Calculated bond distances for five-membered rings containing silicon.

cyclopentene (V) [38], silacyclopenten-2-ene (VI) [39], 1,1-dichloro-1-silacyclopent-2-ene (VII) [39], silacyclopentane (VIII) [40], and 1,1-dichloro-1-silacyclopentane (IX) [40]. The interest in molecules I and VI originated from the possibility that these may show p_π-d_π type π bonding between the silicon atoms and the C=C double bond. The determination of the ring-puckering potential energy function of I, however, showed that while the five-membered ring is planar, it is only slightly more rigid than would be expected without this type of interaction [4]. In addition, the reanalysis of the far-infrared spectrum of VI [39] also showed that the molecule is less rigid than previous results [41,42]. Examination of the silicon–carbon bond distances in Figs. 12 and 13 shows these all to be 1.892–1.898 Å for the SiH_2-CH_2 bonds for molecules I, II, VI, and VIII. For $SiCl_2$-CH_2 bonds in molecules III, IV, VII, and IX these are slightly shortened by about 0.02 Å to 1.872 to 1.878 Å. When the silicon atom is bonded to an olefinic carbon atom, the SiH_2-CH= bonds are shorter (1.869–1.882 Å) by about 0.02 Å than the SiH_2-CH_2 bonds. Likewise, the $SiCl_2$-CH= bonds are also shortened a similar amount as compared to the $SiCl_2$-CH_2 bonds. This does demonstrate that there is a small bond strengthening when the silicon atom bonds to an olefinic carbon atom. Figs. 12 and 13 also show that there is a very small lengthening of the C=C double bond when a silicon atom is next to it. The figures also show that replacement of hydrogen atoms by chlorines on the silicon atoms has the effect of shortening the Si-C bonds in the saturated molecules, also by about 0.02 Å. Molecules I and III were found to be planar molecules in agreement with previous experimental results. Molecules II and IV were calculated to be twisted with twisting angles of 28.1 ° and 27.5 °, respectively.

Vibrational Spectra

As mentioned previously, the scarcity of these samples did not allow them to be fully purified and some impurities remained in the samples and gave rise to some of the spectral peaks. Nonetheless, it is desirable to present the spectra of molecules I to IV. Figs. 14-17 show the infrared and Raman spectra for molecules I and II and Tables 3 and 4 summarize the experimental data and compare them to the calculated values for all four molecules. Figs. 18 and 19 show the calculated infrared and Raman spectra for molecules III and IV. Their observed spectra and a listing of all the spectral bands can be found elsewhere [10]. Molecules I and III have C_{2v} symmetry while II and IV have C_2 symmetry. However, the assignments for II and IV were assigned according to C_{2v} symmetry since the vibrations are quite well approximated by that planar model. With the aid of the computed spectra the vibrational assignments of the four molecules were mostly quite straightforward, and the agreement between observed and calculated values can be seen to be good. However, the presence of some impurity bands made a few assignments somewhat uncertain. The biggest puzzle was, 1,3-disilacyclopent-4-ene (I), and its tetrachloro derivative (III), both showed two strong Raman bands in the C=C region. For For I these are observed at 1600 and 1512 cm^{-1} and for III they are at 1600 and 1509 cm^{-1}. The calculated values using a scaling factor of 0.985 are 1542 for both molecules, so the lower Raman frequency in each case is the logical choice for the assignments. Moreover, for 2-silacyclopentene (VI), the C=C stretching frequency has a low value of 1560 cm^{-1} [41] showing that a silicon atom next to the double bonded carbon lowers this vibrational frequency. Since I has two silicon atoms next to the C=C

39
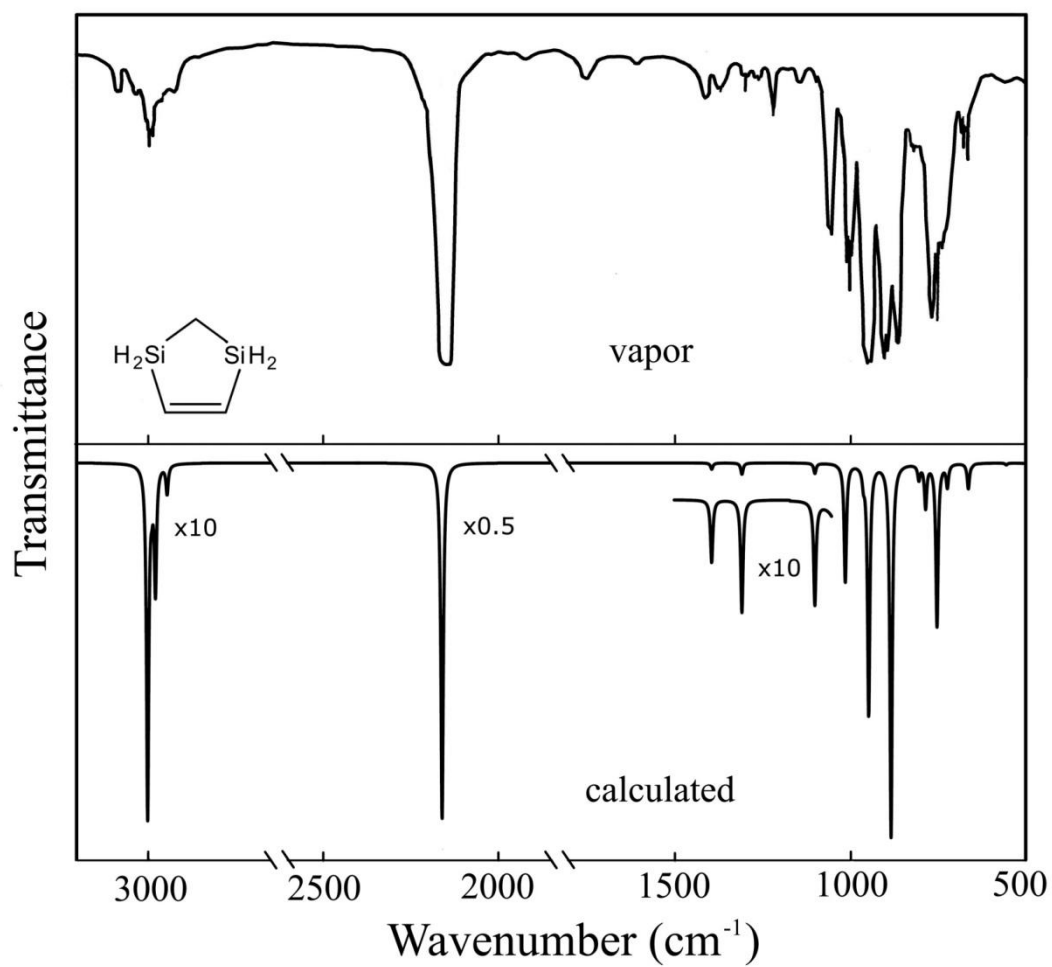
Figure 14. Observed and calculated infrared spectra of 1,3-disilacyclopent-4-ene (I).
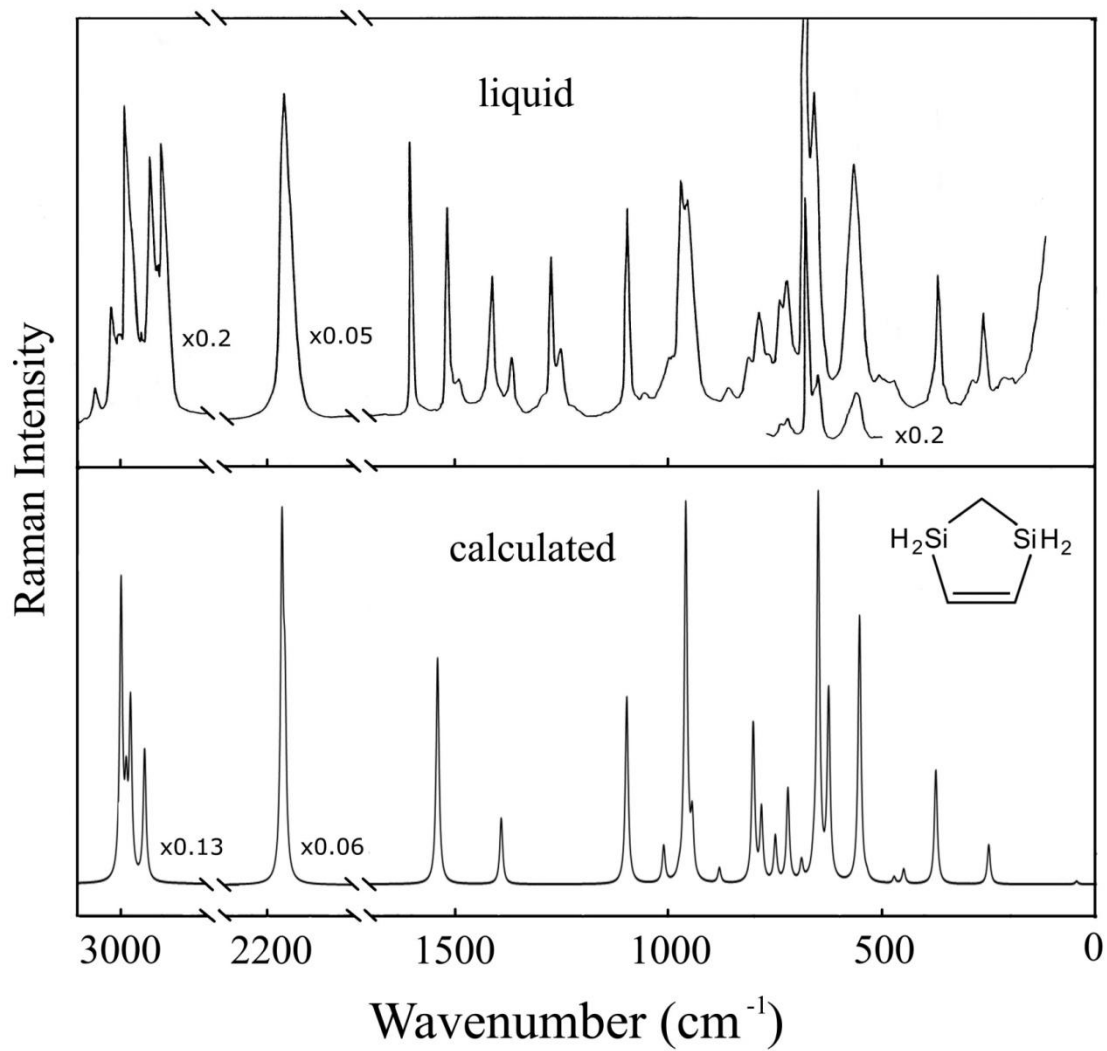
Figure 15. Observed and calculated Raman spectra of 1,3-disilacyclopent-4-ene (I).
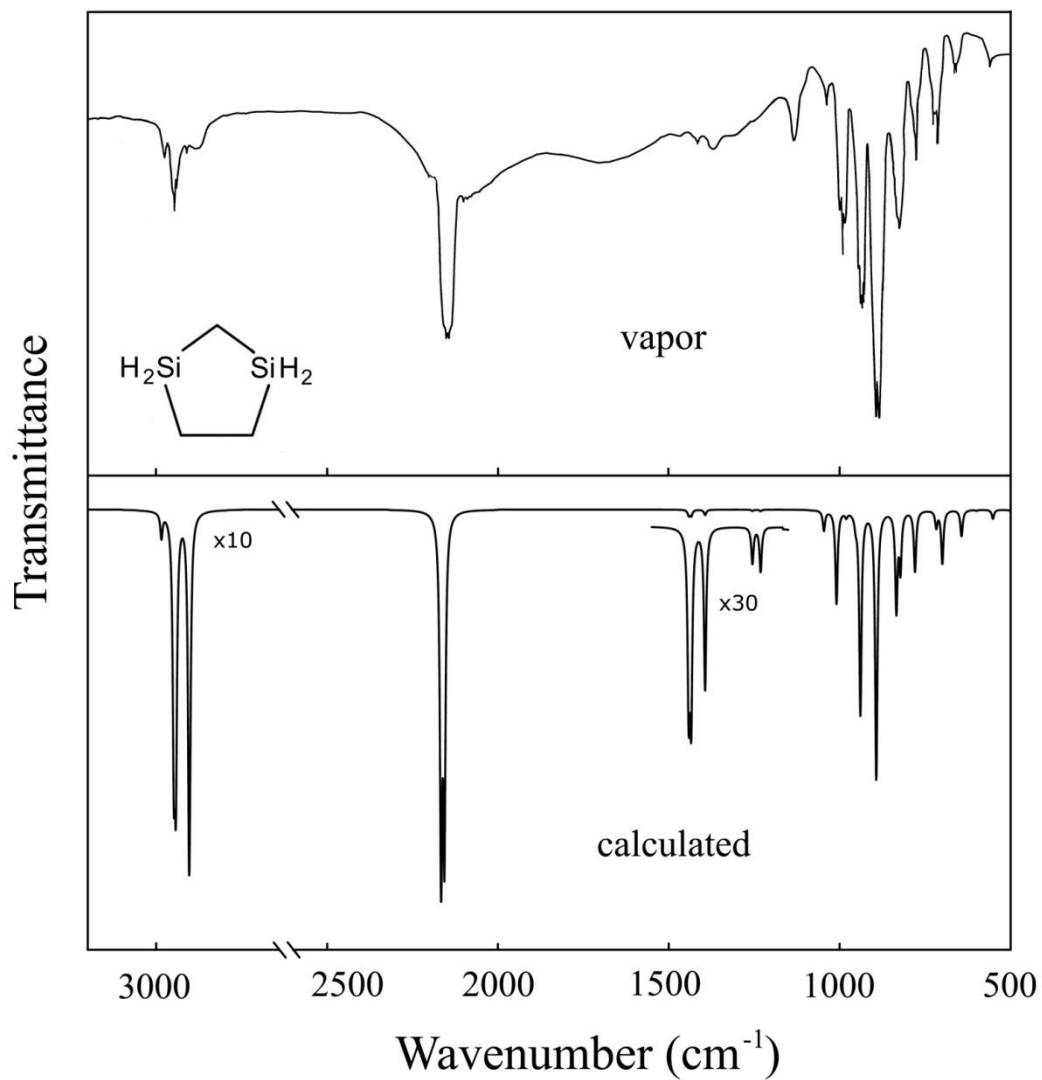
Figure 16. Observed and calculated infrared spectra of 1,3-disilacyclopentane (II).
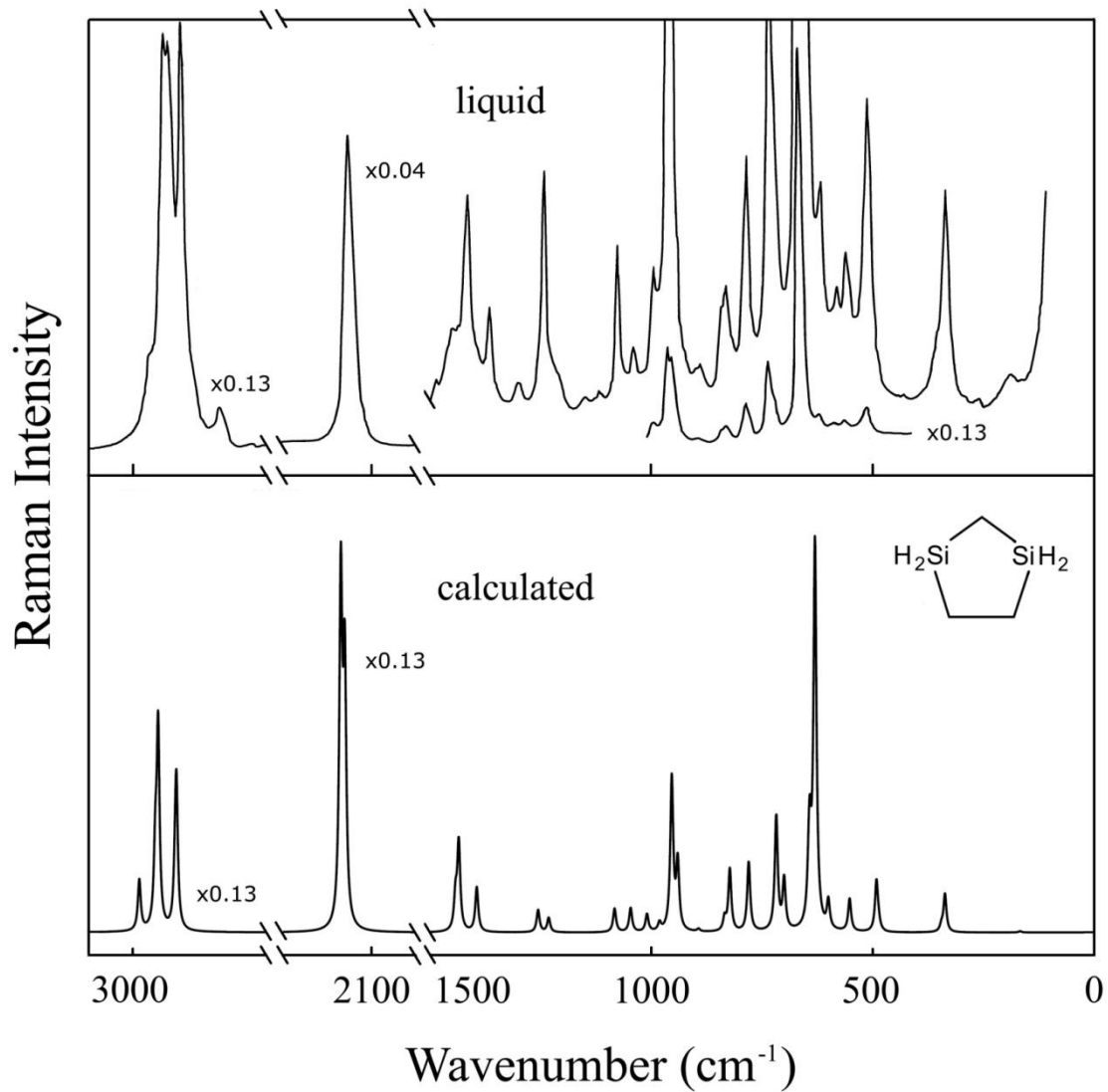
Figure 17. Observed and calculated Raman spectra of 1,3-disilacyclopentane (II).

		Description	1,3-Disilacyclopent-4-ene			1, 1, 3, 3-Tetrachloro-1,3-disilacyclopent-4-ene	
			Infrared (vapor)[a]	Raman (liquid)[b]	Calculated[c]	Raman (liquid)[b]	Calculated[c]
A_1	v_1	C-H sym. Str.	3018 m	3017 (53)	3000 (9, 100)	3028 (100)	3025 (100)
	v_2	CH_2 sym. Str.	2905 m	2922 (113)	2945 (1, 100)	2925 (550)	2957 (38)
	v_3	SiX_2 sym. Str. (i.p.)	2155 vs	2150 (526)	2167 (4, 100)	530 (165)	533 (10)
	v_4	C=C str.	-	1512 (23)	1542 (0, 72)	1509 (94)	1542 (14)
	v_5	CH_2 deformation	1409 w	1410 (12)	1394 (2, 22)	1409 (73)	1381 (3)
	v_6	C-H wag (i.p.)	1093 vw	1094 (17)	1099 (3, 54)	1089 (47)	1094 (7)
	v_7	SiX_2 deformation (i.p.)	948 vs	952 (18)	961 (4, 100)	140 (240)	127 (2)
	v_8	SiX_2 wag (i.p.)	868 vs	861 (2)	883 (100, 4)	170 (vw)	172 (0.4)
	v_9	ring C-Si str. (i.p.)	666 w	672 (100)	651 (0.3, 100)	795 (7)	756 (0.7)
	v_{10}	ring C-Si str. (i.p.)	-	654 (26)	626 (0.03, 48)	710 (7)	692 (5)
	v_{11}	ring deformation	-	370 (11)	375 (0.02, 28)	299 (425)	290 (7)
A_2	v_{12}	SiX_2 antisym. Str. (o.p.)	-	-	2160 (0.01, 93)	580 (52)	550 (4)
	v_{13}	C-H wag (o.p.).	-	-	1024 (0, 0)	-	1019 (0)
	v_{14}	CH_2 twist	-	969 (19)	977 (0, 1)	940 (vw)	941 (0.1)
	v_{15}	SiX_2 twist (o.p.)	-	-	690 (0, 4)	70 (-)	68 (0.1)
	v_{16}	SiX_2 rock (o.p.)	-	513 (3)	537 (0, 1)	140 (240)	123 (2)
	v_{17}	ring twist	-	263 (7)	252 (0, 9)	380 (vw)	372 (0)

Table 3. Characteristic Infrared and Raman frequencies of 1, 3-disilacyclopent-4-ene and 1,1,3,3-tetrachloro-1,3-disilacyclopent-4-ene.

			1,3-Disilacyclopent-4-ene			1, 1, 3, 3-Tetrachloro-1,3-disilacyclopent-4-ene	
		Description	Infrared (vapor)[a]	Raman (liquid)[b]	Calculated[c]	Raman (liquid)[b]	Calculated[c]
B_1	ν_{18}	C-H antisym. Str. (o.p.)	2951 m	2979 (135)	2978 (3, 100)	2965 (288)	3006 (56)
	ν_{19}	SiX_2 sym. Str. (o.p.)	2146 vs	-	2161 (100, 72)	-	397 (0)
	ν_{20}	C-H wag (o.p.)	1297 w	-	1307 (3, 0)	1292 (18)	1304 (0)
	ν_{21}	CH_2 wag	1054 s	1052 (2)	1013 (32, 11)	1002 (15)	1017 (1)
	ν_{22}	SiX_2 deformation (o.p.)	948 vs	952 (18)	947 (68, 15)	170 (vw)	174 (0.1)
	ν_{23}	SiX_2 wag (o.p.)	815 vw	815 (4)	804 (4, 43)	248 (49)	236 (0.5)
	ν_{24}	ring C-Si str. (o.p.)	-	735 (11)	722 (6, 24)	801 (6)	765 (0.1)
	ν_{25}	ring C-Si str. (o.p.)	678 w	-	662 (7, 4)	720 (11)	699 (1)
	ν_{26}	ring deformation	-	478 (2)	474 (6, 2)	-	521 (0)
B_2	ν_{27}	CH_2 antisym. Str. (i.p.)	2991 s	3007 (40)	2988 (1, 100)	2980 (313)	3008 (22)
	ν_{28}	SiX_2 antisym. Str. (i.p.)	2146 vs	-	2162 (93, 35)	520 (120)	521 (0)
	ν_{29}	C-H wag (i.p.)	780 s	791 (8)	784 (12, 20)	749 (6)	721 (0.5)
	ν_{30}	CH_2 rock	750 s	740 (9)	752 (44, 13)	679 (6) ()	684 (0.1)
	ν_{31}	SiX_2 twist (i.p.)	550 w	565 (21)	555 (1, 67)	185 (53)	175 (2)
	ν_{32}	SiX_2 rock (i.p.)	-	-	451 (3, 4)	-	242 (0)
	ν_{33}	ring pucker	48 w	-	46 (1, 1)	-	20 (0)

[a]s-strong; m-medium; w-weak; v-very
[b]Relative intensities in parentheses
[c]Frequency and relative intensities (IR, Raman) were calculated using the B3LYP/cc-pVTZ basis set. The scaling factor was 0.985 for frequencies below 2200 cm^{-1} and 0.961 for above.

Table 3. Continued.

	C$_{2v}$	C$_2$	Description	Infrared (vapor)[a]	Raman (liquid)[b]	Calculated[c]	Raman (liquid)[a]	Calculated[c]
				1,3-Disilacyclopentane			1, 1, 3, 3-Tetrachloro-1,3-disilacyclopentane	
A$_1$ (A)	ν_1	ν_2	αCH$_2$ sym. str.	2930 vs	2918 (40)	2942 (0.1, 44)	2950 vvs	2954 (58)
	ν_2	ν_3	βCH$_2$ sym. str. (i.p.)	2870 vs	2888 (40)	2901 (3, 51)	2920 vvs	2922 (21)
	ν_3	ν_4	SiX$_2$ sym. str. (i.p.)	2145 vs	2150 (100)	2167 (100, 6)	575 s	552 (8)
	ν_4	ν_6	βCH$_2$ deformation (i.p.)	1465 w	1450 (1)	1442 (2, 1)	1460 w	1435 (3)
	ν_5	ν_7	αCH$_2$ deformation	1375 w	1363 (1)	1394 (2, 1)	1349 mw	1379 (3)
	ν_6	ν_9	βCH$_2$ wag (i.p.)	-	1072 (2)	1083 (0.1, 1)	1075 w	1084 (1)
	ν_7	ν_{11}	SiX$_2$ deformation (i.p.)	950 s	956 (9)	953 (3, 4)	139 vs	127 (2)
	ν_8	ν_{12}	ring C-C str.	-	947 (8)	940[*] (0.2, 2)	-	944 (0.01)
	ν_9	ν_{13}	SiX$_2$ wag (i.p.)	899 vs	890 (0.3)	893 (82, 0.1)	189 ms	176 (1)
	ν_{10}	ν_{15}	ring C-Si str. (i.p.)	665[*] w	658 (37)	642 (1, 2)	748 w	737 (0.4)
	ν_{11}	ν_{16}	ring C-Si str. (i.p.)	-	615 (3)	630 (0.1, 10)	663 mw	675 (9)
	ν_{12}	ν_{19}	ring deformation	330 ?	332 (3)	337 (0.01, 1)	299 vvs	285 (8)
A$_2$ (A)	ν_{13}	ν_1	βCH$_2$ antisym. str. (o.p.)	-	2920 (40)	2943 (7, 31)	-	2968 (80)
	ν_{14}	ν_5	SiX$_2$ antisym. str. (o.p.)	-	2150 (100)	2159 (0.1, 76)	520 vvs	534 (0.1)
	ν_{15}	ν_8	βCH$_2$ twist (o.p.)	-	1238 (3)	1255 (0.4, 1)	1268 m	1253 (1)
	ν_{16}	ν_{10}	αCH$_2$ twist	-	991 (2)	981 (2, 0.2)	941 mw	937 (2)
	ν_{17}	ν_{14}	βCH$_2$ rock (o.p.)	-	829[*] (1)	834 (30, 0.4)	-	796 (0.2)
	ν_{18}	ν_{17}	SiX$_2$ twist (o.p.)	-	580 (1)	600 (0.3, 1)	120 s	108 (1)
	ν_{19}	ν_{18}	SiX$_2$ rock (o.p.)	-	510 (4)	491 (0.03, 1)	173 ms	165 (1)
	ν_{20}	ν_{20}	ring twist	-	188 (0.4)	167 (0.1, 0.03)	-	22 (0.04)

Table 4. Characteristic Infrared and Raman frequencies of 1,3-disilacyclopentane and 1,1,3,3-tetrachloro-1,3-disilacyclopentane.

	C_{2v}	C_2	Description	Infrared (vapor)[a]	Raman (liquid)[b]	Calculated[c]	Raman (liquid)[a]	Calculated[c]
					1,3-Disilacyclopentane		**1, 1, 3, 3-Tetrachloro-1,3-disilacyclopentane**	
B_1 (B)	ν_{21}	ν_{23}	βCH_2 sym. str. (o.p.)	2909 w	2900 (41)	2904 (9, 13)	2975 vs	2973 (56)
	ν_{22}	ν_{25}	SiX_2 sym. str. (o.p.)	2143 vs	2145 (100)	2157 (97, 2)	486 s	470 (0.03)
	ν_{23}	ν_{26}	βCH_2 deformation (i.p.)	1415 w	1412 (3)	1434 (2, 3)	1405 ms	1429 (5)
	ν_{24}	ν_{27}	βCH_2 wag (o.p.)	1258 vw	1238 (3)	1231 (1, 0.4)	1239 mw	1238 (1)
	ν_{25}	ν_{29}	αCH_2 wag	996 s	-	1009 (28, 1)	995 w	1014 (1)
	ν_{26}	ν_{30}	SiX_2 deformation (o.p.)	945 s	-	940[*] (61, 1)	-	176 (1)
	ν_{27}	ν_{31}	SiX_2 wag (o.p.)	832 m	829[*] (1)	822 (17, 2)	249 ms	245 (1)
	ν_{28}	ν_{34}	ring C-Si str. (o.p.)	715[*] m	718 (vw)	700 (16, 1)	780 mw	774 (0.4)
	ν_{29}	ν_{35}	ring C-Si str. (o.p.)	665[*] w	658 (37)	644 (8, 1)	-	680 (0.2)
	ν_{30}	ν_{38}	ring deformation	?	347 (1)	345 (1, 0.2)	370 m	360 (1)
B_2 (B)	ν_{31}	ν_{21}	αCH_2 antisym. str.	2972 m	2959 (10)	2985 (1, 19)	-	3004 (31)
	ν_{32}	ν_{22}	βCH_2 antisym. str. (i.p.)	2942 vs	2928 (40)	2949 (7, 27)	2895 vvs	2918 (100)
	ν_{33}	ν_{24}	SiX_2 antisym. str. (i.p.)	2152 vs	2150 (100)	2168 (7, 100)	500 s	503 (13)
	ν_{34}	ν_{28}	βCH_2 twist (i.p.)	1038 m	1039 (1)	1046 (6, 1)	-	1034 (1)
	ν_{35}	ν_{32}	αCH_2 rock	780 m	781 (3)	780 (19, 2)	701 s	707 (1)
	ν_{36}	ν_{33}	βCH_2 rock (i.p.)	730[*] m	730 (7)	717 (5, 3)	-	602 (1)
	ν_{37}	ν_{36}	SiX_2 twist (i.p.)	560 w	559 (2)	552 (3, 1)	-	237 (1)
	ν_{38}	ν_{37}	SiX_2 rock (i.p.)	-	-	486 (5, 0.2)	-	243 (1)
	ν_{39}	ν_{39}	ring pucker	56	-	51 (1, 0)	-	66 (0.1)

[a]s-strong; m-medium; w-weak; v-very
[b]Relative intensities in parentheses
[c]Frequency and relative intensities (IR, Raman) were calculated using the B3LYP/cc-pVTZ basis set. The scaling factor was 0.985 for frequencies below 2200 cm^{-1} and 0.961 for above.
[*]Overlapping bands

Table 4. Continued.
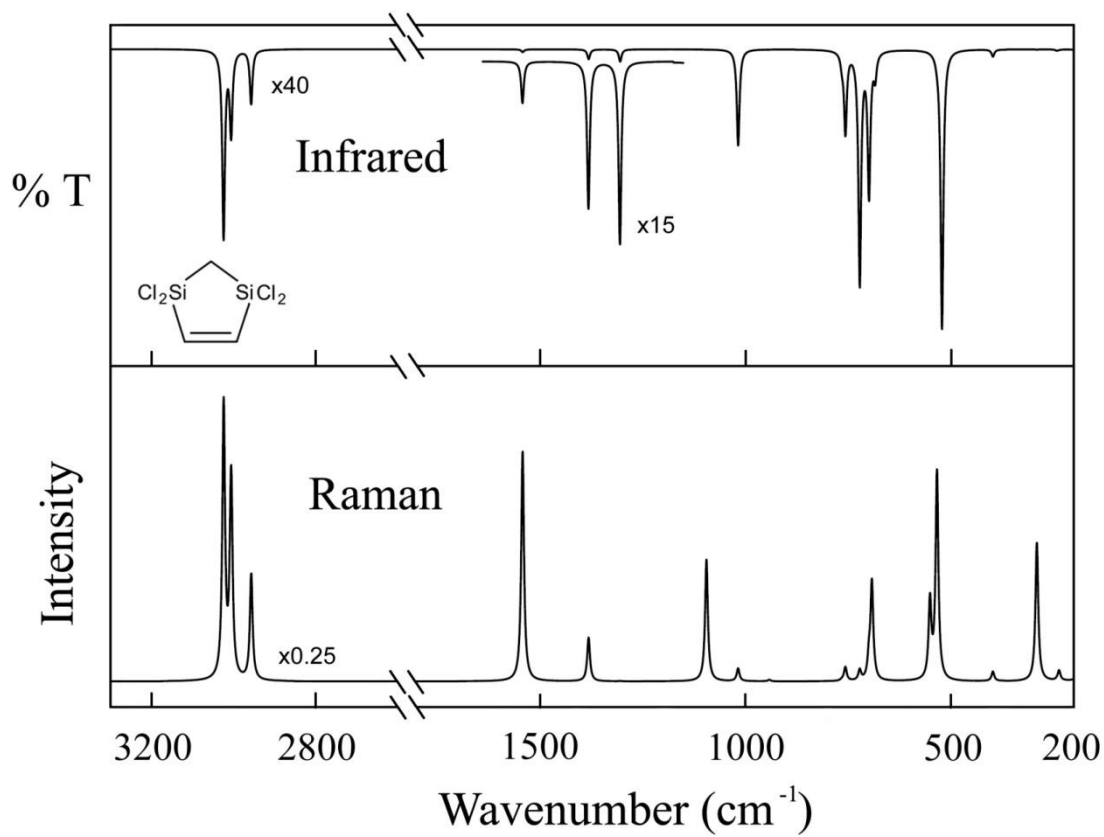
Figure 18. Calculated infrared and Raman spectra for 1,1,3,3-tetrachloro-1,3-disilacyclopent-4-ene (III).
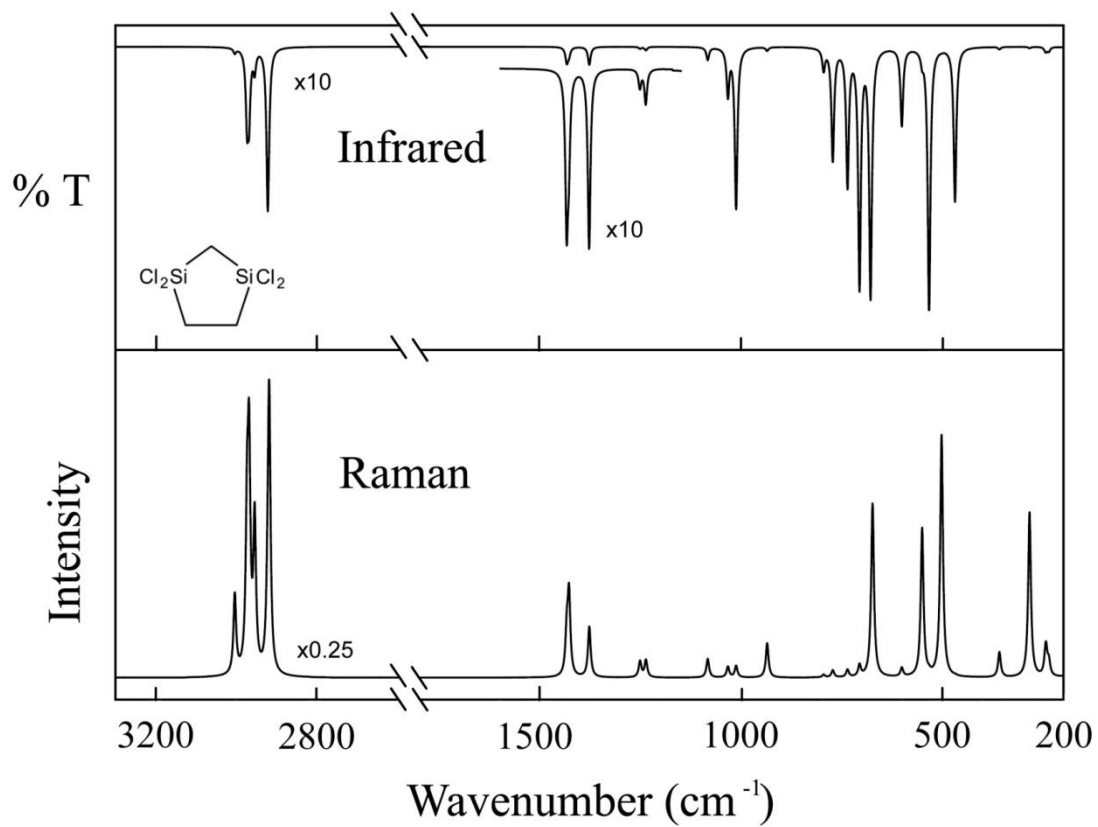
Figure 19. Calculated infrared and Raman spectra for 1,1,3,3-tetrachloro-1,3-disilacyclopentane (IV).

bond, an even lower frequency is expected. Unfortunately, this still leaves the band near 1600 cm^{-1} for I and III as unidentified but must evidently be from a starting material or a side product from the preparation.

Conclusion

The calculations have been provided with the computed structures of the four molecules discussed in this study. They also have assigned their infrared and Raman spectra with considerable confidence. On the structural side the shortening of the SiH_2-C= bond between the silicon atom and the olefinic carbon atom is notable. Simultaneously the C=C double bond is lengthened in these systems. These changes reflect the fact that the Si-C bond is strengthened when the carbon atom is part of a π bonded system. This may be due to p_π-d_π interactions or to electrostatic effects.

CHAPTER VI

THEORETICAL CALCULATIONS, FAR-INFRARED SPECTRA AND

THE POTENTIAL ENERGY SURFACES OF

THE SELECTED FOUR CYCLIC SILANES[*]

Introduction

In many years the low-frequency vibrations and potential energy surfaces of small ring compounds have been investigating [1-2,21-25]. Among these are a number of organosilanes
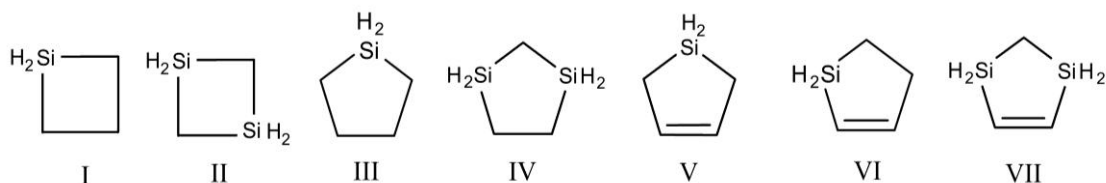
including silacyclobutane (I) [5,43-48], 1,3-disilacyclobutane (II) [49,50], silacyclopentane (III) [9,51-53], 1,3-disilacyclopentane (IV) [4,54], 1-silacyclopent-3-ene (V) [5-8], 1-silacyclopent-2-ene (VI) [39,41-42,55], and 1,3-disilacyclopent-4-ene (VII) [4,54]. Among these, molecules I, II, IV, and VII were prepared for the first time by Laane's laboratories. Theoretical calculations for I [43], II [49], and VI [39] have been reported previously. In the present work III, IV, V, and VII were reported with a focus on theoretical calculations of the conformational energies of these molecules as

governed by their low-frequency out-of-plane vibrations.

Theoretical Calculations

Ab initio and DFT computations were carried out using the Gaussian 09 package [19]. The MP2/cc-pVTZ computation was utilized to determine the molecular structures and the conformational energies for different values of selected vibrational coordinates. The B3LYP/cc-pVTZ computation was used to calculate vibrational frequencies. A scaling factor of 0.985 was used for the lower frequencies. The vibrational frequencies of the ring-puckering and ring-twisting motions were calculated using the DA1OPTN program [26]. The VNCOSPX program [27] was used to calculate the pseudorotational frequencies.

Fig. 20 shows the calculated structures for III and V, which they have not been previously reported. III is twisted with a calculated twist angle of 27.7 ° while V is planar. The structures for IV and VII were presented previously [54].

Experimental

The far-infrared spectra of 1,3-disilacyclopentane (IV) and 1,3-disilacyclopent-4-ene (VII) were previously recorded and published in part [4].   Additional spectra were reported in the L. F. Colegrove Ph. D. thesis [10].
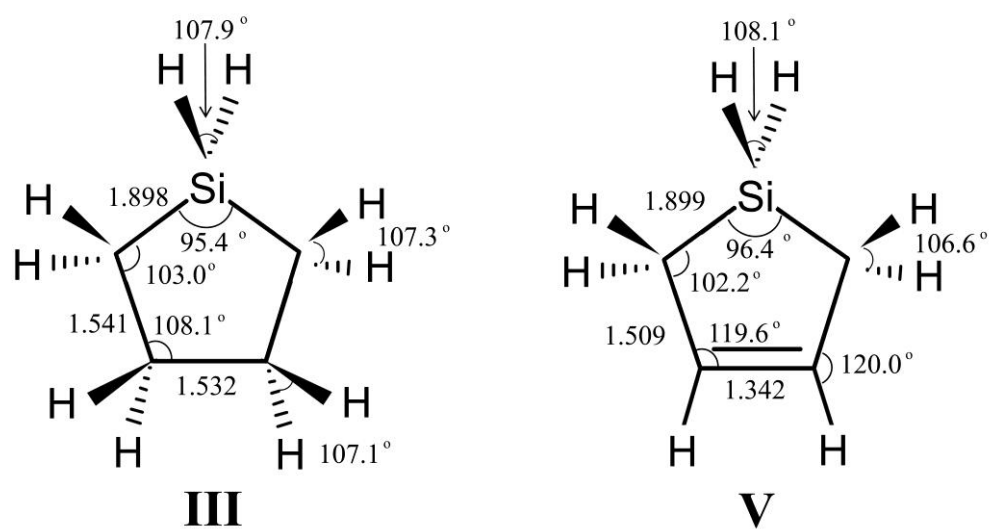
Figure 20. Calculated structures for silacyclopentane (III) and 1-silacyclopnet-3-ene (V).

Results and Discussion

1. 1-Silacyclopent-3-ene

Previously the far-infrared spectrum of this molecule was reported and its one-dimensional ring-puckering potential energy function was determined [8]. At that time the reduced mass was only estimated, but some years later, after the refining process of carrying out reduced mass calculations [56,57], an improved value was determined [6]. That value of μ = 128.64 au along with the kinetic energy expansion terms, which account for the change in reduced mass with coordinate, will be utilized here. The conformational energy of V was calculated point by point using increments of Δx = 0.008 to 0.28 Å for the puckering coordinate. The computations predicted a barrier of 3.8 cm^{-1} and the calculated values were fit with the potential function in Eq. (6.1):

$$V(cm^{-1}) = 2.200x10^5x^4 - 0.0183x10^5x^2 \tag{6.1}$$

This can be compared to the function in Eq. (6.2) determined from the experimental data [6] and the calculated reduced mass [6]

$$V(cm^{-1}) = 2.130x10^5x^4 - 0.0054x10^5x^2 \tag{6.2}$$

The experimentally determined function in Eq. (6.2) has a barrier of only 0.3 cm^{-1}. Thus both functions produce a miniscule barrier so for all practical purposes the molecule is planar and very nearly a pure quartic oscillator. Fig. 21 compares the two functions and the agreement can be seen to be excellent. Table 5 compares the observed experimental frequencies to those calculated from Eqs. (6.1) and (6.2). The latter fits the data very well since the potential energy parameters were refined to fit the spectroscopic data. Moreover, the excellent agreement is gratifying since it also confirms that our model
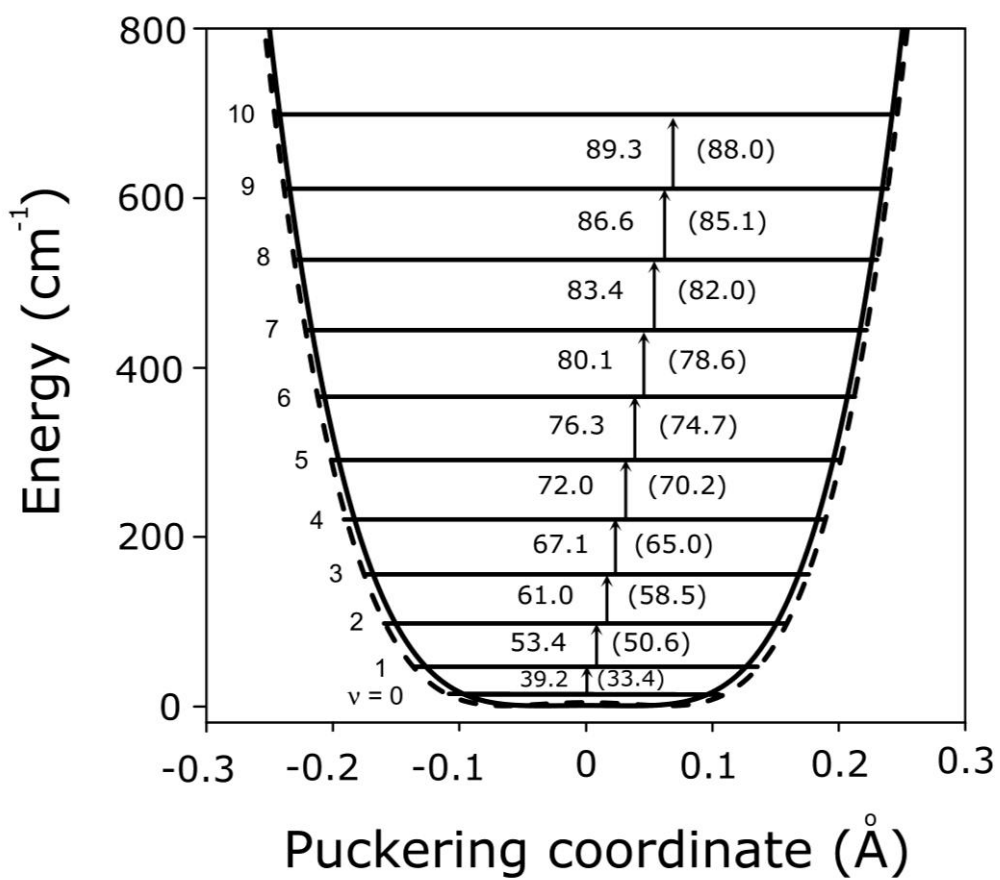
Figure 21. Experimental (solid line) and theoretical (dashed line) potential energy functions for the ring-puckering vibration of 1-silacyclopent-3-ene (V).

55

Transition	Frequency, cm^{-1}		
	obs.	calc.[a]	calc.[b]
0-1	39.2	39.1	33.3
1-2	53.4	53.5	50.6
2-3	61.0	61.2	58.5
3-4	67.1	67.3	65.0
4-5	72.0	72.3	70.2
5-6	76.3	76.5	74.7
6-7	80.1	80.3	78.6
7-8	83.4	83.6	82.0
8-9	86.6	86.6	85.1
9-10	89.3	89.3	88.0

[a] $V(cm^{-1}) = 2.130 \times 10^5 x^4 - 0.0054 \times 10^5 x^2$ (experimental fit)
[b] $V(cm^{-1}) = 2.220 \times 10^5 x^4 - 0.0183 \times 10^5 x^2$ (*ab initio*)

Table 5. Observed and calculated ring-puckering transitions for 1-silacyclopent-3-ene.

[56,57] for calculating the reduced mass for the puckering has produced a very accurate

value. The frequencies calculated for Eq. (6.1) agree remarkably well considering that

the potential energy function was generated directly from the *ab initio* data. As seen

from Eq. (6.1), the slightly higher (but still tiny) barrier for this function causes the

lowest two energy levels to start to merge and produces a lower transition frequency by

5.9 cm^{-1}. All of the other frequencies from the *ab initio* calculation function of Eq. (6.1)

wind up 1.3-2.9 cm^{-1} lower than those from eq. (6.2). It is remarkable that the *ab initio*

prediction is as good as it is, and it is interesting that the barrier difference of 3.5 cm^{-1}

does have a significant effect on the observed values. It is also noteworthy that the

GAUSSIAN program predicts a transition frequency from the DFT calculation of 62cm^{-1}

which is higher than the experimental value of 39.2 cm^{-1}. The theoretical value is based

on the assumption of harmonic forces but, as the result has been obtained, the puckering

vibration is very nearly pure quartic.

2. 1,3-Disilacyclopent-4-ene

The calculations for VII were carried out in similar fashion as for V. The

previously reported potential function for the puckering determined from the

experimental data [4] was

$$V(cm^{-1}) = 1.48 \times 10^5 x^4 + 0.030 \times 10^5 x^2 \tag{6.3}$$

The function determined from the *ab initio* calculations is

$$V(cm^{-1}) = 1.83 \times 10^5 x^4 + 0.020 \times 10^5 x^2 \tag{6.4}$$

Both functions are shown in Fig. 22 and the agreement is very good. Although the
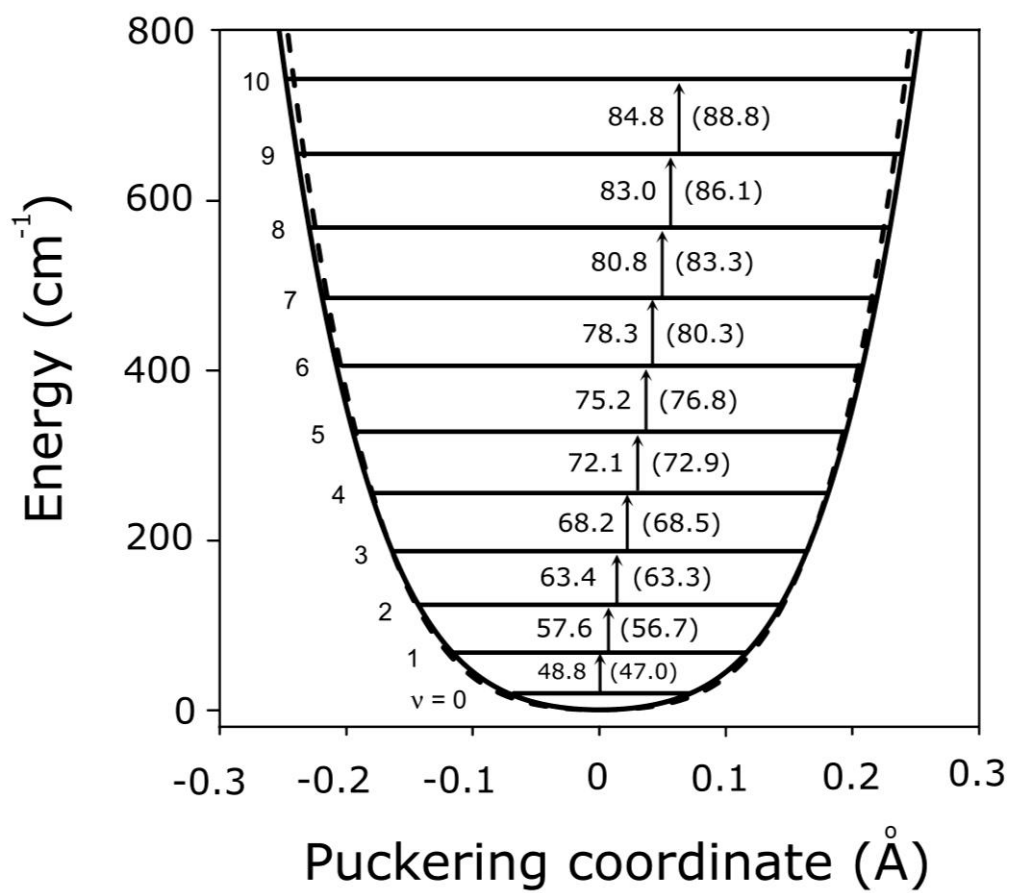
Figure 22. Experimental (solid line) and theoretical (dashed line) potential energy functions for the ring-puckering vibration of 1,3-disilacyclopent-4-ene (VII).

quartic constant in Eq. (6.4) is about 20% higher than that in Eq. (6.3), this is somewhat compensated for by a lower quadratic constant. Table 6 also shows the comparison between the observed transition frequencies and those calculated from Eqs. (6.3) and (6.4). The generally higher values resulting from the *ab initio* calculation result from the higher quartic potential energy constant. Nonetheless, it is obvious that the theoretical calculation again does a remarkably good job of predicting the potential energy curve quite accurately. The DFT calculation predicts a puckering frequency of 46 cm^{-1} whereas the experimental value is 48.8 cm^{-1}.

3. Silacyclopentane

The far-infrared data for this molecule were reported by Laane in 1969 [53] and a two-dimensional potential energy surface in terms of the ring-twisitng and ring-bending modes was calculated based on that data in 1990 [9]. The potential energy surface that best fit the data had potential energy minima corresponding to the two equivalent twisting structures and a barrier to planarity of 2110 cm^{-1}. The bent conformations are saddle points on the surface and were calculated to be 601 cm^{-1} in energy below the planar structure. *Ab initio* calculations presented here confirm that the molecule is twisted and that the bent forms are intermediate in energy. The theoretical calculations predict a twisting barrier of 2493 cm^{-1} and also predict that the bent structure is a saddle point with an energy 1026 cm^{-1} lower than the planar structure. Fig. 23 depicts the energy values both from the present theoretical calculation along with those from the

Transition	Frequency, cm^{-1}		
	obs.	calc.[a]	calc.[b]
0-1	48.8	49.2	47.0
1-2	57.6	56.9	56.7
2-3	63.4	62.5	63.3
3-4	68.2	67.0	68.5
4-5	72.1	70.9	72.9
5-6	75.2	74.3	76.8
6-7	78.3	77.3	80.2
7-8	80.8	80.1	83.3
8-9	83.0	82.6	86.1
9-10	84.8	85.0	88.8

[a] $V(cm^{-1}) = 1.480 \times 10^5 x^4 + 0.0300 \times 10^5 x^2$ (experimental fit)
[b] $V(cm^{-1}) = 1.830 \times 10^5 x^4 + 0.0203 \times 10^5 x^2$ (*ab initio*)

Table 6. Observed and calculated ring-puckering transitions for 1,3-disilacyclopent-4-ene.
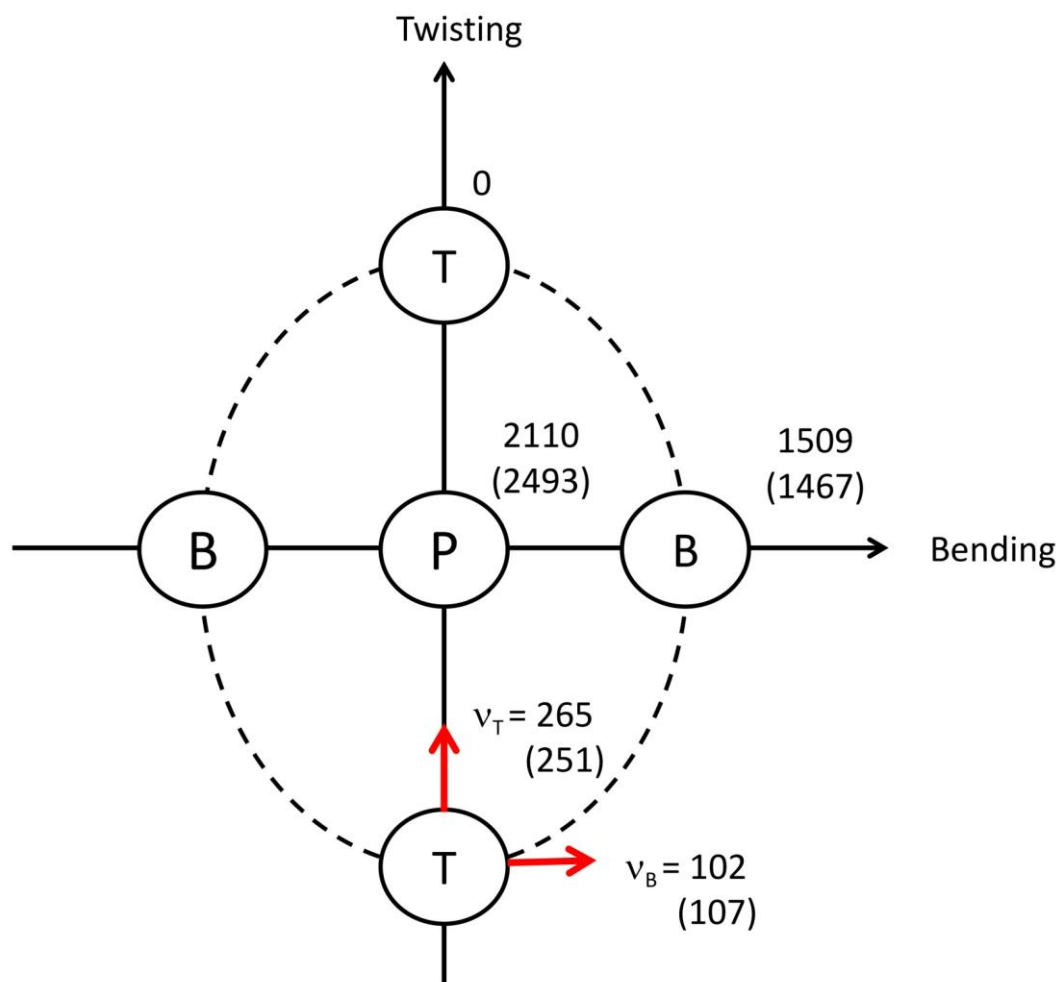
Figure 23. Schematic representation of the two-dimensional potential energy surface for the ring-twisting and ring-bending vibrations of silacyclopentane (III). P = planar structure; T = twist structure (energy minimum); B = bent structure (saddle point); ν_T = twisting frequency; ν_B = bending frequency. The energy and frequency values are in cm^{-1} are from [9]; values in parentheses are from the theoretical calculations.

previously published two-dimensional energy surface. The agreement is reasonably good, but it must be remembered that the experimental barriers are extrapolated values since the spectroscopic data only extend up to about 1200 cm^{-1}, well below the calculated barrier of 2493 cm^{-1}. Figure 24 presents a comparison of the potential energy curves along the ring-twisting coordinate from the published two-dimensional surface [9] and from the theoretical calculation in the present study. A comparison of the observed and calculated frequencies is also shown. The calculated values are from the one-dimensional fit of the conformational energy as a function of the twisting coordinate. It has the form

$$V(cm^{-1}) = 6.01x10^4x^4 - 2.45x10^4x^2 \hspace{2cm} (6.5)$$

This may be compared to the twisting part of the two-dimensional surface

$$V(cm^{-1}) = 3.68x10^4x^4 - 1.76x10^4x^2 \hspace{2cm} (6.6)$$

The barrier values differ by about 15% and the *ab initio* value to be somewhat more reliable than the extrapolated experimental one. The frequencies calculated from the theoretical calculation differ from the observed by about 20%, but that is not unreasonable considering that they were calculated using a one-dimensional potential energy approximation. The DFT calculation predicts a twisting frequency of 251 cm^{-1} while the experimental value is 265 cm^{-1}. In the initial study of silacyclopentane (III) a one-dimensional hindered pseudorotational model was used to calculate the energy levels [27]. Using a barrier to pseudorotation of 1362 cm^{-1} and a pseudorotational constant of B = 1.97 cm^{-1}, the experimental data were fit very well. In this present work the barrier to pseudorotation (the energy of the bent conformation relative to the twist
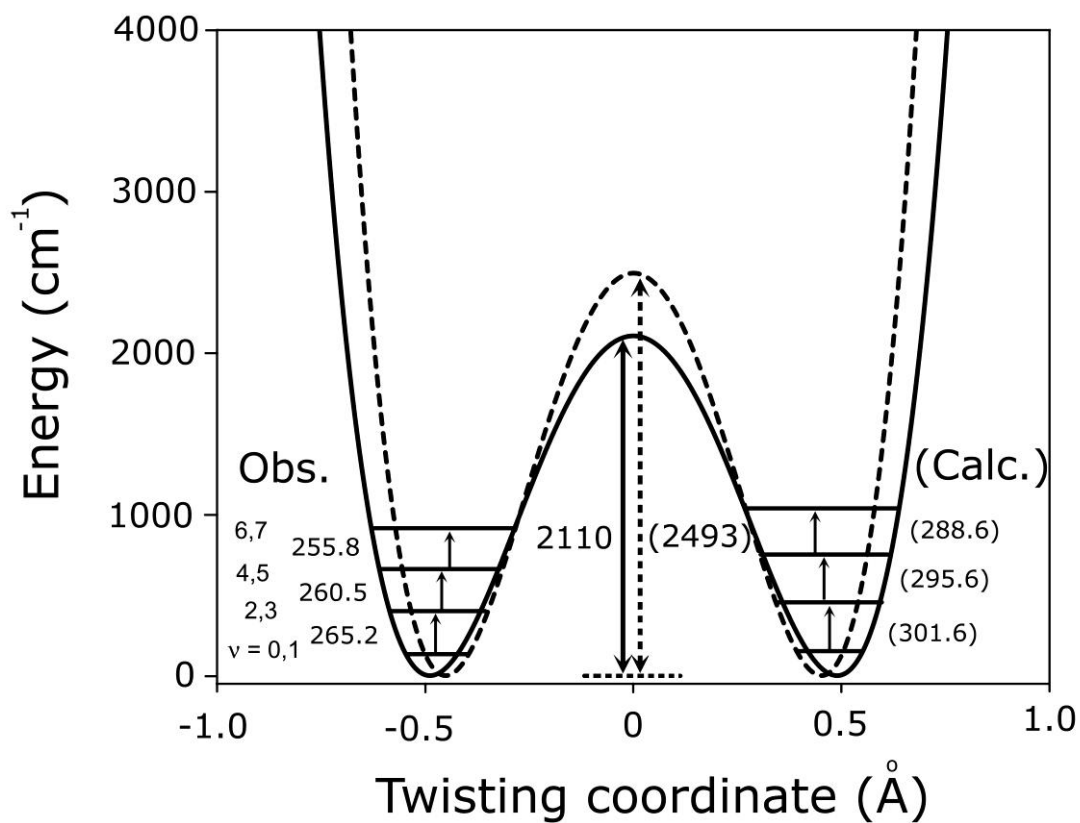
Figure 24. Comparison of the one-dimensional potential energy curves from the experimental (solid line) and theoretical (dashed line) determinations for the ring twisting of silacyclopentane (III). Values in parentheses are calculated from Eq (6.5).

structure) was calculated to be 1467 cm^{-1}. The energy level calculation has been repeated [27] using the potential energy function

$$V \text{ (cm}^{-1}) = \frac{1}{2}V_2(1-\cos 2\varphi) \tag{6.7}$$

with V = 1467 cm^{-1} and B = 1.828 cm^{-1}. The result is shown in Fig. 25. It can be seen that the energy differences calculated for the *ab initio* function differ remarkably little from those observed.

4. 1,3-Disilacyclopentane

The experimental data for this molecule were obtained along with that for the unsaturated 1,3-disilacyclopent-4-ene (VII) [4,10]. Fig. 26 shows the far-infrared bands between 53 and 58 cm^{-1} observed for the pseudorotational (bending) motion. The spectra for the twisting vibration were not observed. Fig. 27 shows a schematic diagram for the calculated conformational energies of this molecule and Fig. 28 presents the potential energy curve calculated along the ring-twisting coordinate. Fig. 28 also shows the calculated ring-twisting frequencies. In order to represent the bending (hindered pseudorotation) the potential function was utilized again in Eq. (6.6). Values of V = 878 cm^{-1} and B = 0.968 cm^{-1} were selected in order to fit the lowest energy transition observed in the spectra. Fig. 29 shows this function along with the observed and calculated transition frequencies. The agreement here again is remarkably good.

The lower barrier to planarity of this molecule (1395 cm^{-1}) as compared to silacyclopentane (III) results from the presence of a second silicon atom in the five-
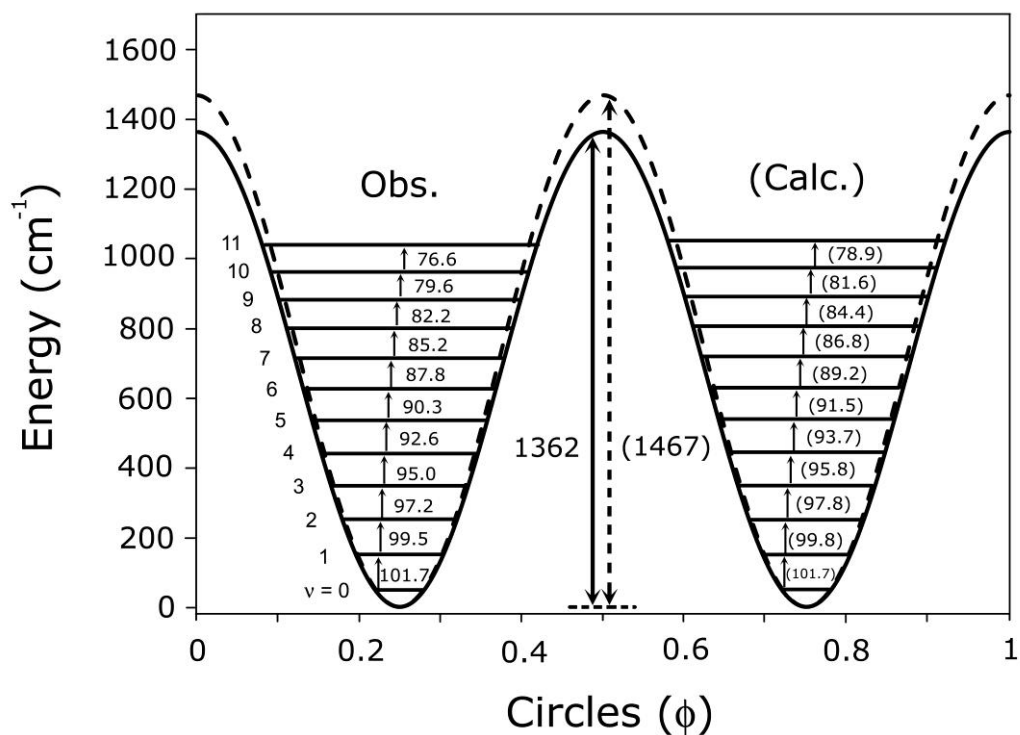
Figure 25. Calculated one-dimensional potential energy curve (dashed line) for the hindered pseudorotation (bending) of silacyclopentane (III) compared to the experimental curve (solid line) [53]. All of the energy levels shown are nearly doubly degenerate. The potential function is periodic in terms of the pseudorotational angle Φ and repeats itself after one circle (2π radians).
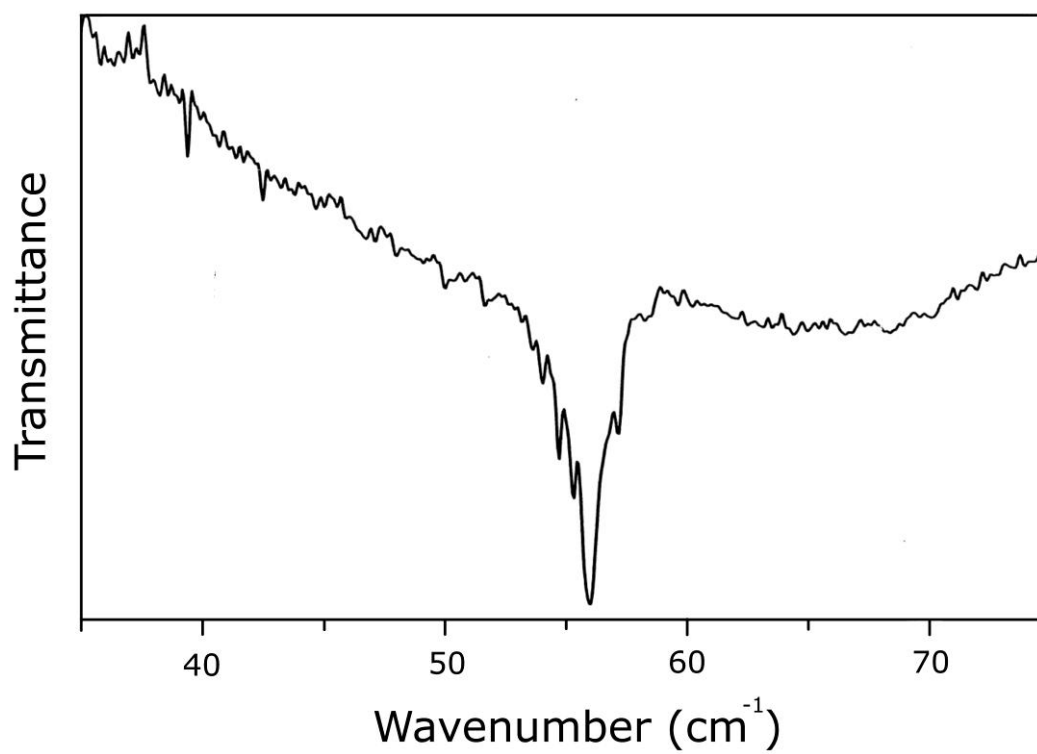
Figure 26. Far-infrared spectrum showing the ring-bending (pseudorotational) transitions of 1,3-disilacyclopentane [4,10].
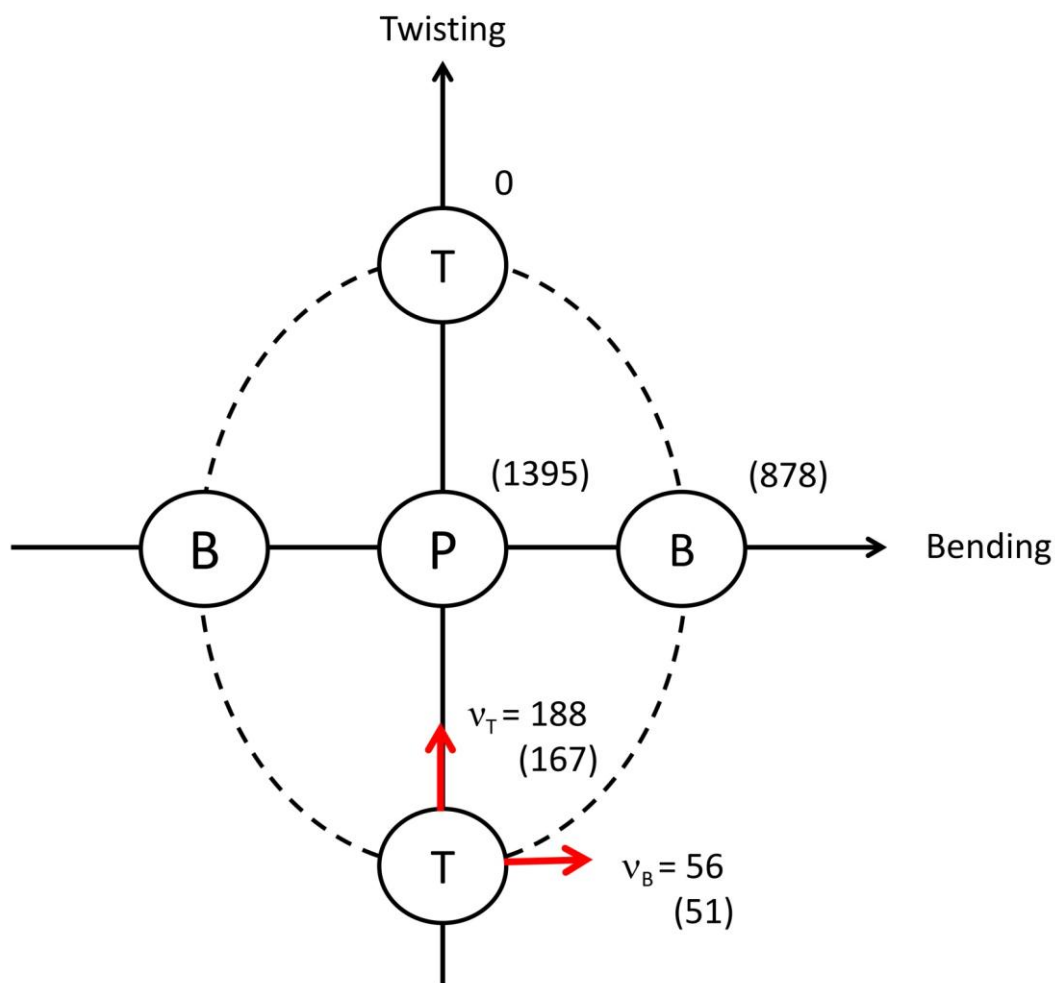
Figure 27. Schematic representation of the two-dimensional potential energy surface for the ring-twisting and ring-bending vibrations of 1,3-disilacyclopentane (IV). The observed frequency values in cm^{-1} are from [10] ; values in parentheses are from the theoretical calculations.
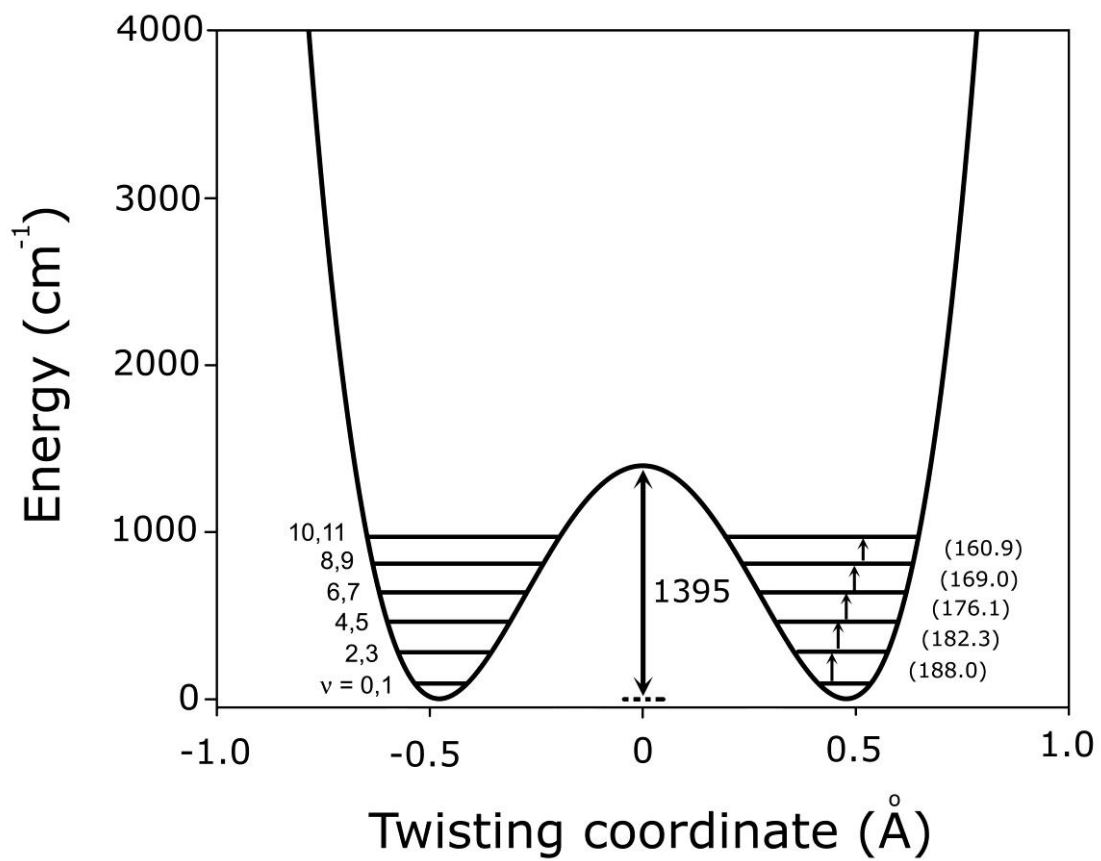
Figure 28. One-dimensional potential energy curve calculated for the ring-twisting vibration of 1,3-disilacyclopentane (IV).
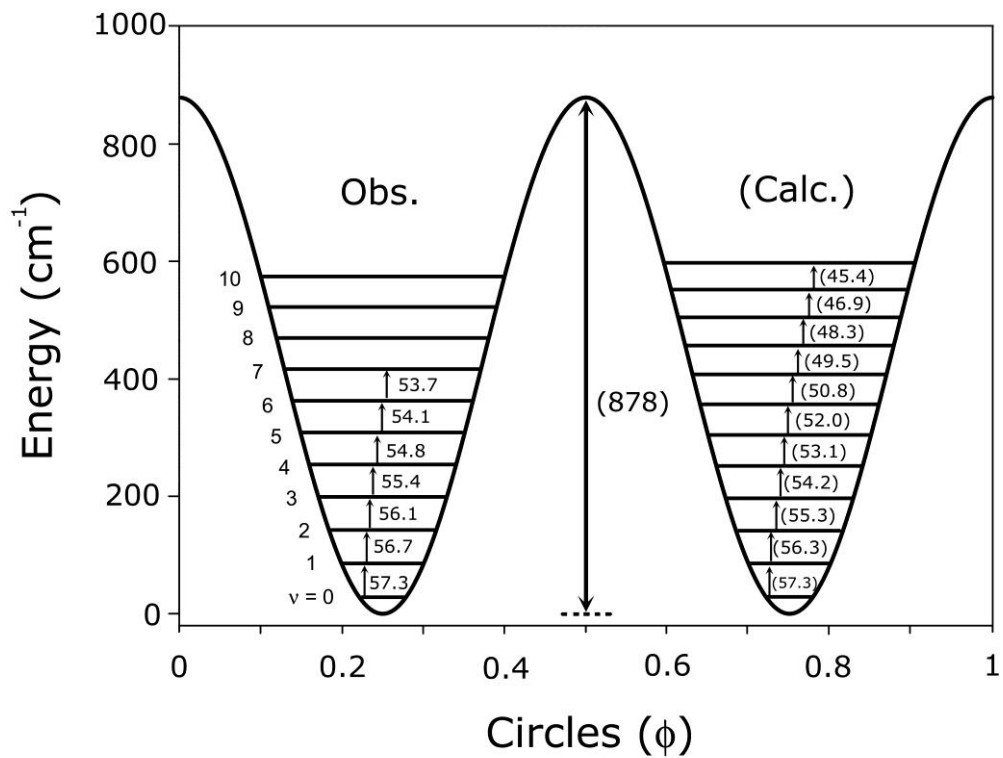
Figure 29. One-dimensional potential energy curve calculated for the hindered pseudorotational (ring-bending) vibration of 1,3-disilacyclopentane (IV).

membered ring. The CSiC angle bending force constants are smaller than the corresponding CCC angle bending constants and these results in lower angle strain. For the same reason the barrier to pseudorotation, as shown in Fig. 29, is lower (878 cm^{-1}) than for III (1362 cm^{-1}).

Conclusion

Utilizing *ab initio* computations the one-dimensional ring-puckering potential energy functions for 1-silacyclopent-3-ene (V) and 1,3-disilacyclopent-4-ene (VII) were generated and compared to the experimentally determined functions. The remarkably good agreement not only demonstrates how well present day *ab initio* calculations perform in calculating conformational energies, but it also provides strong support for the validity of previous determinations of potential energy functions from spectroscopic data. The conformational energies for silacyclopentane (III) and 1,3-disilacyclopentane (IV) have also been calculated and one-dimensional ring-twisting and pseudorotational potential energy functions has been generated. These again provided excellent confirmation of the experimental functions. It is most gratifying to see that experimental analyses and theoretical computations are in such good agreement.

CHAPTER VII

VIBRATIONAL SPECTRA AND DFT CALCULATION FOR

SQUALENE[*]

Introduction

Squalene (Fig. 30) is a linear triterpene molecule found in many organisms throughout nature including mammals, plants, and bacteria [11,12]. Organisms primarily utilize squalene by cyclizing it to form a vast array of triterpenes that have functions ranging from regulating membrane fluidity to protection against pathogens [58,59]. Squalene also exists in organisms in its native, linear state and can be found in high quantities in the oils of human skin, shark liver, and the oil of several plants such as olive [60-63]. Studies have suggested that squalene has many bioactive properties including antioxidant and anticancer activities, and these properties may contribute to the health benefits of the Mediterranean diet [11,64-65]. This diet is high in squalene-rich olive oil and has a low occurrence of associated cancers [66-68]. Squalene has also been shown to reduce the prevalence of colon cancer resulting from chemical exposure and breast cancer caused by DNA damage [11,69-71]. Interestingly, sharks are known to not have cancer and this is thought to be related to the high level of squalene in sharks [72]. Squalene is also used for pharmaceutical and commercial purposes such as an

---

Figure 30. The structure of squalene. The calculated bond distances (Å) are shown in the center.

emulsifier for drug delivery, an adjuvant for vaccine delivery, a moisturizer in cosmetics, a surfactant in dry cleaning, and as a vulcanization test molecule [73].

The biosynthesis of squalene utilizes the isoprenoid pathway [59]. Two molecules of the C_{15} isoprenoid intermediate farnesyl diphosphate (FPP) are condensed to form C_{30} squalene [74,75]. This reaction is carried out by the enzyme squalene synthase, requires the reducing agent NADPH, and results in the connection of two farnesyl moieties from C1 of one farnesyl molecule to C1 of the second farnesyl molecule [74,75]. This results in the linear structure of squalene with six carbon–carbon double bonds (C=C) in the backbone at carbons 2, 6, 10, 14, 18, and 22 (Fig. 30) that should provide unique qualities for spectroscopic studies such as Raman spectroscopy. Reports of Raman spectroscopy analysis for squalene are limited and have been used to identify squalene as a component of olive oil [13], to study the effect of squalene on the packing of lipid bilayers and monolayers [14], to analyze the degradation of squalene by bacteria [15], and to analyze the components of sebaceous gland exudates [16]. However, there are no reported studies on a detailed analysis of the squalene structure based on Raman spectroscopy. Given the importance of this molecule, a molecular-level understanding of the squalene structure will be invaluable in advancing squalene functional studies.

Raman spectroscopy was utilized to study the structure of hydrocarbons called botryococcenes from the green microalgae Botryococcus braunii that are structurally and biosynthetically (produced from two farnesyl molecules) similar to squalene [76]. Botryococcenes have several Raman active C=C bonds including backbone C=C bonds

73

similar to squalene, a central branch C=C bond, and exomethylene groups [77]. Coupled with DFT calculations, Raman spectroscopy was able to distinguish between these different C=C groups; backbone C=C frequencies in the 1663–1679 cm^{-1} range, exomethylene frequencies in the 1646–1655 cm^{-1} range, and branch C=C frequencies in the 1642–1649 cm^{-1} range [76]. While squalene is similar to botryococcenes, it only contains backbone C=C groups. Here a similar analysis of squalene was reported using Raman spectroscopy as well as infrared spectroscopy to assign frequencies to all bonds in squalene. In addition, density functional theory calculations were carried out to complement the experimental work.

Experimental Methods

A Jobin–Yvon U-1000 spectrometer equipped with a liquid nitrogen-cooled charged-coupled device (CCD) detector was used to record the liquid Raman spectrum of squalene. A Coherent Verdi-V10 laser operating at 532 nm was used and typically operated at 2 Watts of power. The liquid mid-infrared spectrum of squalene was recorded on a Bruker Vertex 70 FT spectrometer equipped with a globar light source, a KBr beamsplitter and deuterated lanthanum triglycine sulfate (DLaTGS) detector. Liquid squalene was obtained from Sigma.

Theoretical Calculations

Density functional theory (DFT) computations were carried out using the B3LYP/cc-pvtz. Squalene can possess a variety of conformations resulting from internal

74

rotations about their single C-C bonds. Hence, calculations were carried out on several conformations of the molecule but only minor effects on the vibrational frequencies and bond distances were found. A scaling factor of 0.969 was used for all frequencies above 1350 cm^{-1} [76] and 0.980 was used for the lower frequencies.

Results and Discussion

The calculated structure of squalene (Fig. 30-center) has bond distances in line with expectations. The C=C bond distances are all 1.336 ± 0.001 Å, the C-C single bonds not adjacent to the double bonded carbon atoms are 1.546 ± 0.001 Å, and single bonds adjacent to the double bonded carbon atoms are 1.506 ± 0.006 Å. Figs. 31 and 32 show the experimental liquid-phase Raman and infrared spectra of squalene, respectively. The computed spectra for the individual (vapor phase) molecule are also shown in the figures. The frequency agreement between the experimental and calculated spectra is in good agreement, but as is commonly the case, the intensities are in somewhat poorer agreement. Since squalene has 234 vibrational frequencies, both the C-H stretching region (50 vibrations in the 2800–3100 cm^{-1} region) and the fingerprint region (184 vibrations below 1700 cm^{-1}) are extremely rich with spectral bands. This makes it very difficult to do a one to one correlation between observed and calculated spectral bands. The calculated frequencies are expected to be within 10 cm^{-1} of the observed frequencies, but since there are often several observed spectral bands within 10 cm^{-1} of each other, identifying which correlates to which calculated vibrational frequency is challenging. Table 7 presents a summary of the different types of
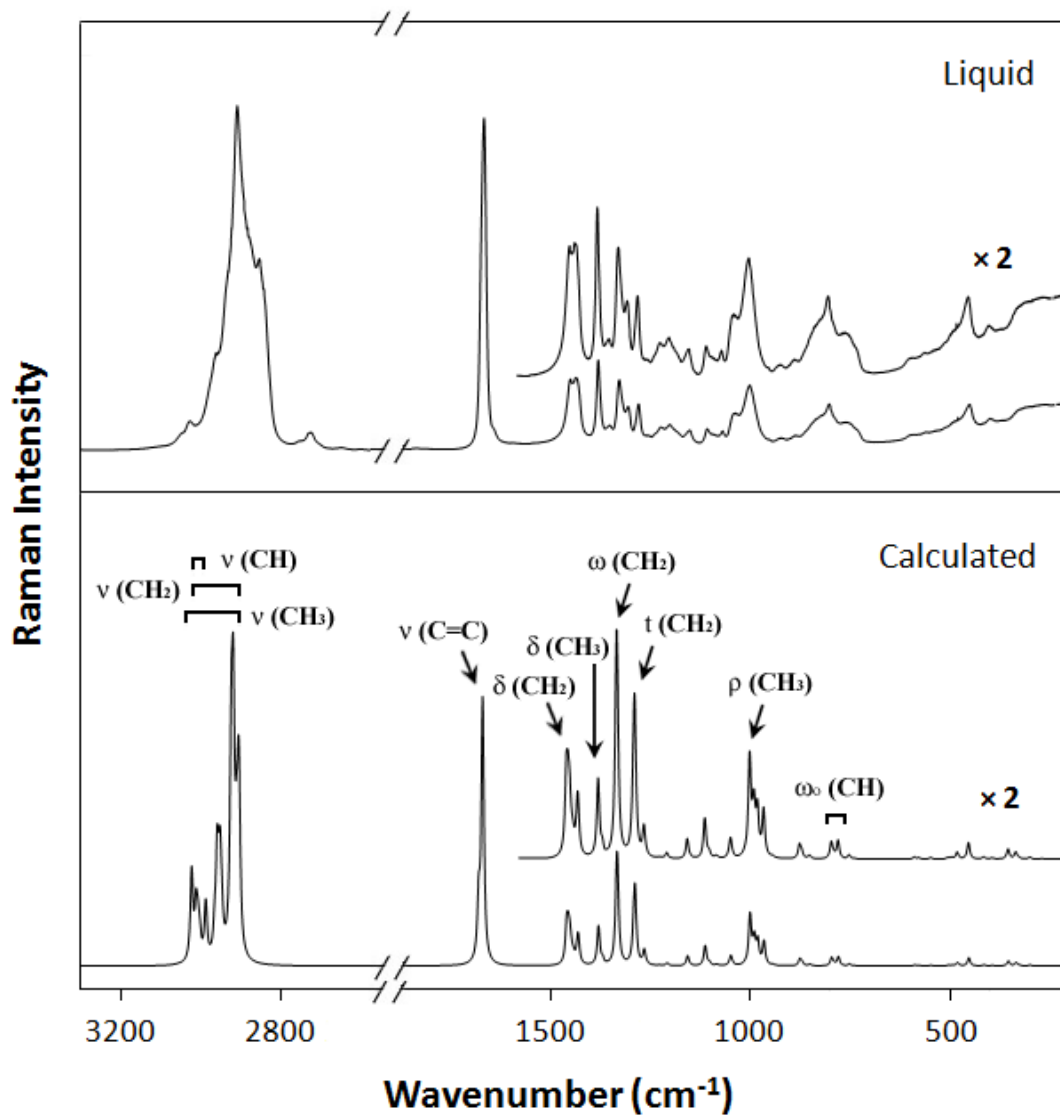
Figure 31. The experimental and calculated Raman spectra of liquid squalene.
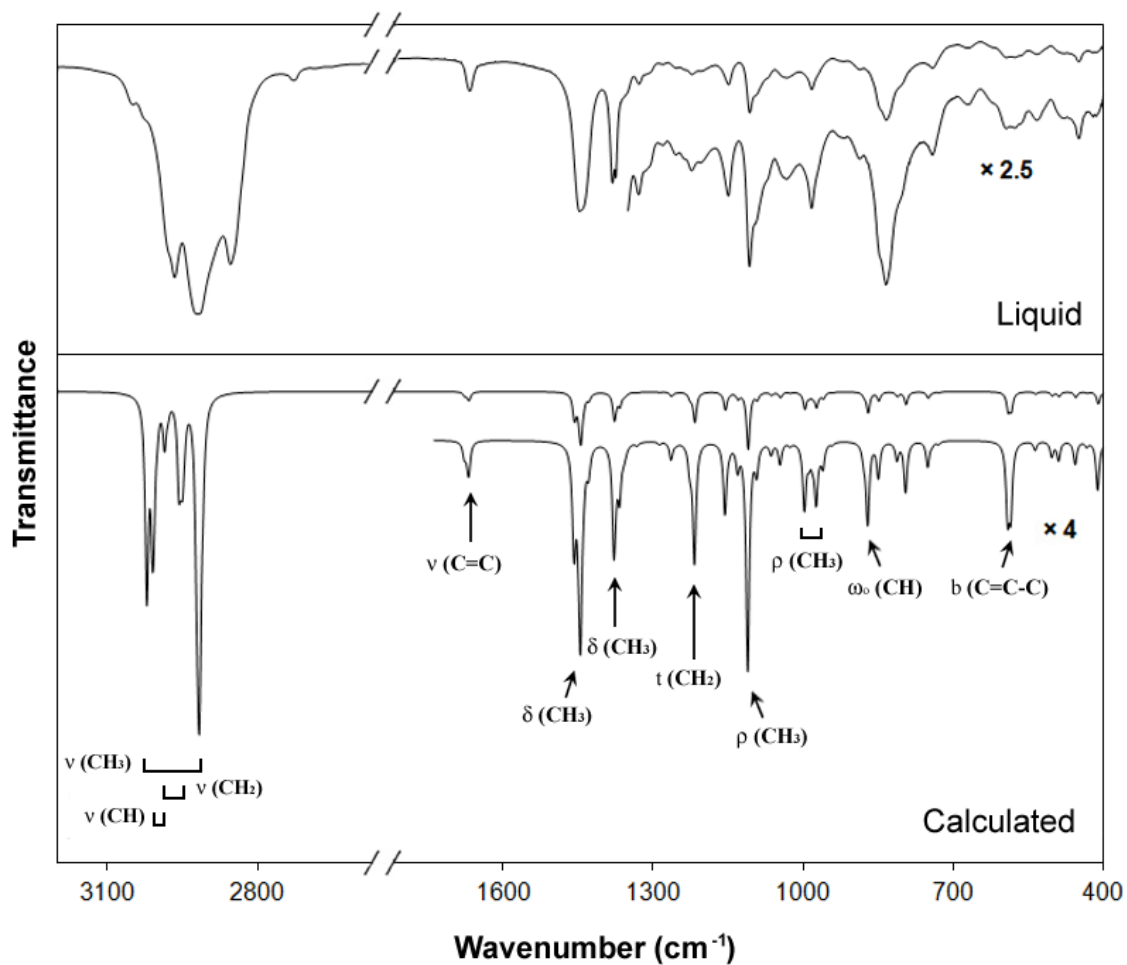
Figure 32. The experimental and calculated infrared spectra of liquid squalene.

Symbol	Vibration	Wavenumber Range (cm^{-1})	Number of vibrations
ν (CH$_3$)	CH$_3$ stretch	2911-3024	24
δ (CH$_3$)	CH$_3$ deformation	1254-1460	24
ρ (CH$_3$)	CH$_3$ rock	943-1228	16
τ (CH$_3$)	CH$_3$ torsion	110-209	8
ν (CH$_2$)	CH$_2$ stretch	2904-2988	20
δ (CH$_2$)	CH$_2$ deformation	1428-1460	10
ω (CH$_2$)	CH$_2$ wag	1207-1333	10
t (CH$_2$)	CH$_2$ twist	1012-1291	10
ρ (CH$_2$)	CH$_2$ rock	730-1207	10
ν (CH)	=C-H stretch	3006-3012	6
ω_i (CH)	CH wag (in-plane)	1012-1379	6
ω_o (CH)	CH wag (out-of-plane)	778-1000	6
ν (C=C)	C=C stretch	1668-1679	6
ν (C-C)	C-C stretch	730-1379	23
b (C-C-C)	C-C-C angle bend	169-503	6
b (C=C-C)	C=C-C angle bend	319-592	12
ω_o (C-CH$_3$)	C-CH$_3$ wag (out-of-plane)	452-503	8
ω_i (C-CH$_3$)	C-CH$_3$ wag (in-plane)	353-434	8
τ (C-C)	Internal rotation (C-C)/Skeletal	4-209	15
τ (C=C)	Internal rotation (C=C)/Skeletal	42-209	6

Table 7. Vibrations of squalene.

vibrational modes in squalene and the frequency ranges calculated (and observed) for each. Table 8 presents a condensed version showing the observed and calculated frequencies and intensities along with approximate descriptions for the more prominent infrared and Raman bands. It should be noted that for a large molecule such as this, the vibrational modes, especially for the low-frequency ones, will be highly coupled. Hence a single vibrational frequency, for example, may have contributions from C-C stretchings, CH wags, CH_3 rocks, as well as skeletal motions. Some of the vibrational descriptions based on the symbolic representation in Table 7 are shown in Figs. 31 and 32.

In the previous study of the botryococcene hydrocarbons each bond of the C=C stretching modes resulted in an individual vibrational frequency for the most part without significant interactions with the stretching of other bonds [76]. The backbone, exomethylene, and branch C=C frequencies were found in different frequency ranges. For squalene the two C=C groups near the ends of the molecule (carbons 2 and 22) vibrate together (symmetrically or antisymmetrically) giving rise to two almost identical frequencies of 1679 cm^{-1} (Table 7). The other four C=C bonds (carbons 6, 10, 14, 18) vibrate simultaneously with differences in the phase of the motions, and these produce four frequencies in the 1668–1672 cm^{-1} range (Table 7). For the botryococcene molecules the backbone C=C vibrations were found previously in the 1663–1679 cm^{-1} range [76], so the results here for squalene are consistent with that of botryococcenes. In addition to the intense C=C stretching bands in the Raman several other bands were obtained with strong intensity. These include all types of C-H stretchings, the CH_3

79

Frequency (cm^{-1})			Approximate assignment
Calculated	Infrared	Raman	
2960 (97, 0)	2967 vvs		ν (CH$_3$), ν (CH$_2$)
2919 (1613, 4)	2920 vvs		ν (CH$_3$), ν (CH$_2$)
2919 (5, 117)		2913 vvs	ν (CH$_3$), ν (CH$_2$)
1670 (13, 0)	1668 m		ν (C=C)
1668 (0, 100)		1668 vvs	ν (C=C)
1458 (0, 12)		1451 ms	δ (CH$_3$), δ (CH$_2$)
1446 (58, 0)	1449 vs		δ (CH$_3$), δ (CH$_2$)
1379 (42, 0)	1383 s		δ (CH$_3$), ω_i (CH), ν (C-C)
1379 (0, 12)		1382 s	δ (CH$_3$), ω_i (CH), ν (C-C)
1333 (0, 29)		1330 ms	δ (CH$_3$), ω (CH$_2$), ω_i (CH)
1287 (0, 15)		1281 m	δ (CH$_3$), t (CH$_2$)
1218 (52, 0)	1224 m		ρ (CH$_3$), t (CH$_2$), ν (C-C)
1157 (31, 0)	1151 m		ρ (CH$_3$), t (CH$_2$), ω_i (CH)
1112 (100, 0)	1108 ms		ρ (CH$_3$), ν (C-C)
1000 (0, 12)		1003 ms	ρ (CH$_3$), ω_o (CH)
998 (27, 0)	984 m (broad)		ρ (CH$_3$), ν (C-C)
975 (26, 0)			ρ (CH$_3$), ν (C-C)
872 (35, 0)	836 ms (broad)		ω_o (CH), ν (C-C)
850 (16, 0)			ω_o (CH), ν (C-C)
796 (23, 0)			ω_o (CH), ν (C-C)
795 (0, 3)		804 m	ω_o (CH), ν (C-C)
452 (0, 3)		454 m	ω_o (C-CH$_3$), b (C=C-C)

Table 8. Observed and calculated frequencies for the more prominent bends of squalene.

deformations $\delta(CH_3)$, CH_2 deformations $\delta(CH_2)$, CH_2 wags $\omega(CH_2)$, CH_2 twists $t(CH_2)$, and CH_3 rocks $\rho(CH_3)$. In the infrared spectrum the C=C stretching bands are considerably less intense, but other bands show up with strong intensity including the C-H stretches, the CH_3 deformations $\delta(CH_3)$, CH_2 twists $t(CH_2)$, and CH_3 rocks $\rho(CH_3)$.

Conclusion

Squalene is an important molecule because of its bioactive properties and similarity to the botryococcenes which were studied previously [76]. Raman and infrared spectra have been recorded and DFT computations were used to predict its structure and vibrational frequency. The match between theory and experiment is excellent. However, the molecule has 234 vibrations, many of which are strongly coupled, so the descriptions are very complicated.

CHAPTER VIII

RAMAN SPECTRA, DFT CACULATIONS FOR

BOTRYOCOCCENE HYDROCARBONS[*]

Introduction

In recent years, interest in the use of green algae as a source of biofuels has increased due to the need to reduce greenhouse gas emissions and because of depletion of world petroleum reserves [78]. For algae to produce enough oil to meet fuel demands, large scale culturing of algae and monitoring of oil production will be required [79,80]. Current analysis methods for monitoring algal oil production are complicated, time consuming, and destructive [17]. Thus, a simple and nondestructive method for analyzing algal oil composition is required. Raman spectroscopy is such a technique and has been used to detect various molecular compounds in algae, both to detect algae in aqueous samples and differentiate algal strains, as well as analyze cellular triglycerides, the most common oil used to produce biofuels [17, 81-91]. Thus, Raman spectroscopy has great potential to be used as an in vivo detection method for monitoring algal oil production. Spectroscopic characterization, other than NMR, of *B. braunii* hydrocarbons is extremely limited [89,92]. A characteristic absorbance spectroscopy peak for

---

botryococcenes has been identified and used to quantitate extracted botryococcenes [92]. Raman spectroscopy has been used on the A race of *B. braunii* to determine that the intracellular oils were similar in nature to the extracellular oils and that these oils were composed of long chain unsaturated hydrocarbons [89]. Specific characterization by Raman spectroscopy for any hydrocarbon from any race of *B. braunii* has not been reported. There are several C=C bonds in botryococcenes that offer unique Raman spectroscopic parameters. For example, the methylation of C_{30}–C_{33} botryococcenes causes C=C bond migration from the backbone endo positions to exo positions at carbons 2, 6, 17, and 21 to create exomethylene groups (Fig. 33A). Additionally, the C-26 branch C=C bond is specific to botryococcenes. In our present work we report characterization of botryococcenes from the B race of *B. braunii* by Raman spectroscopy and density function theory (DFT) calculations. Additionally, an identified Raman signature specific to methylated botryococcenes is used to map *in vivo* the presence of methylated botryococcenes in the extracellular matrix and intracellular oil bodies of live *B. braunii* cells.

Experimental

Algal culturing and purification of B. *branii botryococcenes* were performed in laboratory of Professor Timothy P. Devarenne at Department of Biochemistry and Biophysics, Texas A&M University [76]. Raman spectra of squalene (Sigma), total hydrocarbon extract, and purified botryococcenes (all in n-hexane in a cuvette) were obtained at Horiba Scientific (Edison, NJ) using a Horiba LabRam HR 800 confocal
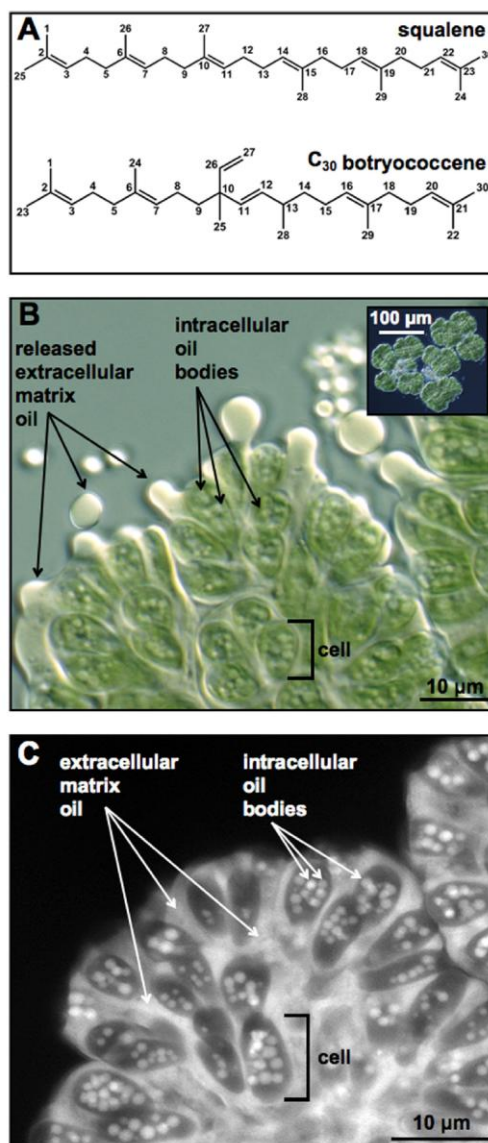
Figure 33. Microscopy and Nile red fluorescent imaging of *B. braunii* cells. (A) Structure of squalene and C_{30} botryococcene. (B) Transmitted light microscope image of a partial *B. braunii* colony showing pressure-released extracellular oil and intracellular oil bodies. A *B. braunii* colony was subjected to pressure by gently pressing on the microscope slide coverslip to expel extracellular oil. *Inset* shows full *B. braunii* colony for perspective. (C) Colony of *B. braunii* treated with Nile red and viewed by fluorescent microscopy to visualize the Nile red-stained extracellular matrix oil and intracellular oil bodies.

Raman microscope. The Raman spectrometer was coupled with an Olympus BXFM microscope and a liquid nitrogen-cooled CCD detector. The excitation source was a Melles-Griot laser operating at 532 nm with a 50-mW output.Asinglet lens with a focal length of 40 mm was used.

Raman spectra of squalene and total hydrocarbon extract contained in vials without solvent were also recorded with a Jobin Yvon U-1000 double monochromator equipped with a liquid nitrogen-cooled CCD detector. A Coherent Verdi-V10 laser operating at 532 nm was utilized as the excitation source. A laser power of 2W was typically used.

In vivo mapping by confocal Raman spectroscopy was performed at the Texas A&M Materials Characterization Facility using a Horiba Jobin Yvon LabRam IR system with an Olympus BX 41 microscope, a computer-controlled motorized XYZ microscope stage, and a liquid nitrogen-cooled CCD detector. Excitation was achieved with a laser wave length of 785nm at an output power of 20 mW. The spectral maps were recorded with a spectral resolution of 0.16 cm^{-1} and pixel size of 275 nm with an UPLSAPO 100×/1.4 oil immersion objective. Cell photobleaching was performed using a 785-nm laser at a power output of 500 mW for at least 20 min. Exact treatment times varied as colony cell density varied across the z axis. Photobleaching was considered complete once the high, consistent Raman intensities across 200–3600 cm^{-1} sufficiently decreased to allow detection of individual Raman peaks and remained static for at least 2 min. All Raman spectra were collected in 60-cm^{-1} segments with accumulation times of 1000 s for each segment. Spectra were analyzed for peak wavenumbers using the LabSpec

program version 5.58.25. Microscopy imaging of *B. braunii* colonies was performed at the Texas A&M University Microscopy and Imaging Center using Nile red fluorescence [76].

Computations

DFT computations used the GAUSSIAN 03 package [18] to obtain the calculated vibrational frequencies and produce the computed Raman spectra. The B3LYP method and cc-pvtz basis set were utilized. Ascaling factor of 0.969 was applied for all frequencies. This value was selected to match the observed and calculated ν(C=C) stretching frequencies for squalene. The computed spectra were produced using the GaussView 4.1.2 program.

Results and Discussion

1. *B. braunii* System Description

Most of the botryococcene oils in *B. braunii*, B race, localize to the colony extracellular matrix and can be released with pressure (Fig. 33B). It is well known that *B. braunii* cells also have many intracellular oil bodies [93-95] (Fig. 33B). Both these intracellular oil bodies and extracellular oil can be visualized using the fluorescent neutral lipid-binding stain Nile red, which has been used to accurately estimate *B. braunii* oil content in high-throughput screens [96-98]. Therefore, fluorescence microscopy and Nile red were used to show the dramatic accumulation of lipids in the extracellular matrix and in intracellular oil bodies (Fig. 33C). The lipid composition of

these intracellular oil bodies is not known. Thus, the ultimate goal of this research is to use Raman microspectroscopy to detect specific botryococcenes within both the extracellular matrix and intracellular oil drops to begin to address the questions about oil body botryococcene composition. Experimental Raman Spectra for Botryococcenes—To identify spectral regions that contain specificity for botryococcenes, Raman spectroscopy was applied to squalene and a total hydrocarbon extract from *B. braunii*, B race. Because a total hydrocarbon extract from some strains of the B race of *B. braunii*, for example the Berkeley strain, is predominantly C_{34} botryococcene [99-101] and GC analysis of our total hydrocarbon extract shows C_{34} botryococcene as the primary constituent, comparison of the two spectra should indicate regions unique to botryococcenes. Analysis of the two spectra indicates similarity across the spectra (Fig. 34A). However, the 1600–1700 cm^{-1} region for $v(C=C)$ stretching vibration were focused because the main structural differences between squalene and botryococcenes are in the C=C bond positions. Within this spectral region, squalene generated a single band at 1668 cm^{-1}, and the total hydrocarbon fraction generated two bands at 1647 and 1660 cm^{-1} (Fig. 34A). Because the subsequent analysis of purified botryococcenes was performed in n-hexane (see below), the Raman spectra of squalene and total hydrocarbons dissolved in n-hexane were analyzed to ensure that the difference in the $v(C=C)$ stretching region could still be detected in the presence of n-hexane. As shown in Fig. 34B, the 1600–1700 cm^{-1} $v(C=C)$ stretching region of the spectra of squalene and total hydrocarbons in n-hexane shows the same bands seen without n-hexane. However,
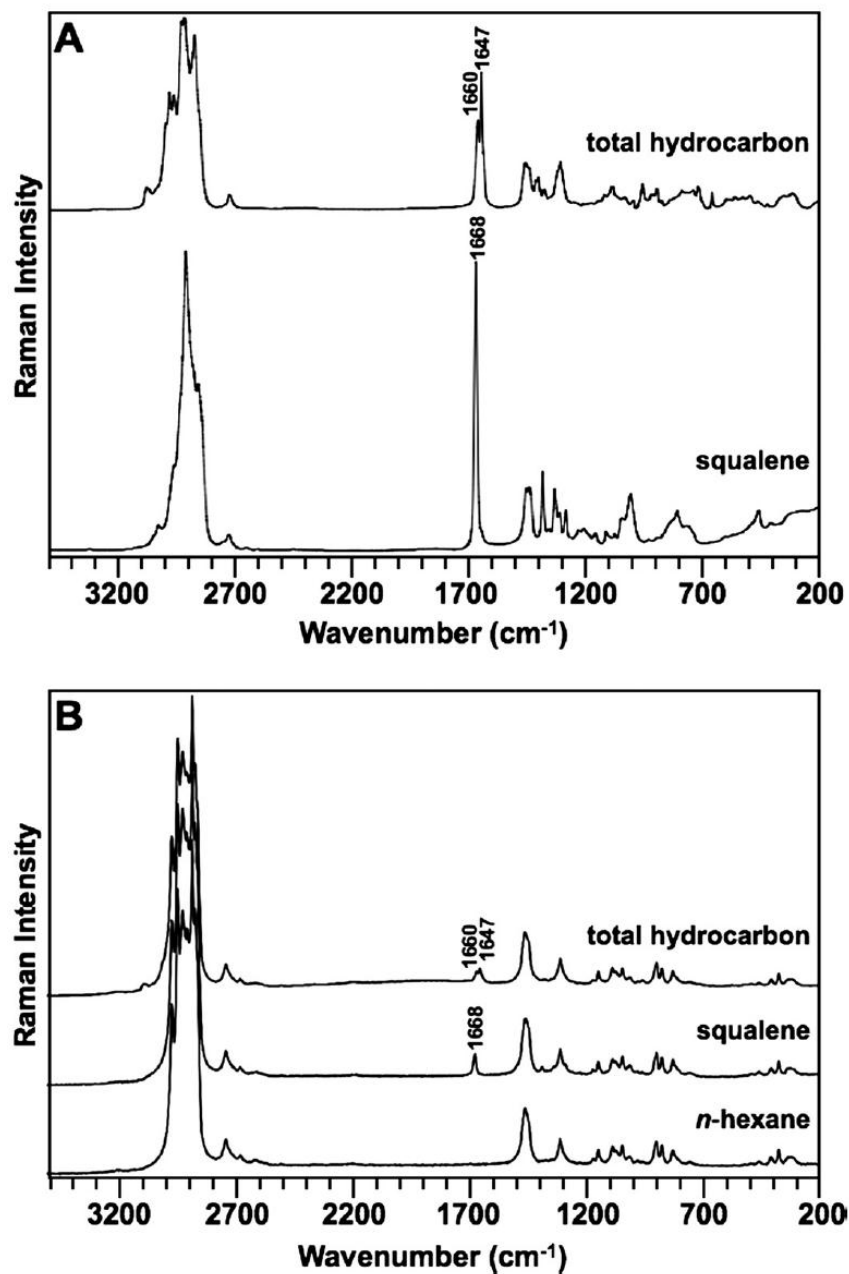
Figure 34. Raman spectra of squalene and total *B. braunii* hydrocarbons. (A) Total hydrocarbon extract from *B. braunii* and a pure, commercially   acquired squalene sample were analyzed by Raman spectroscopy without solvent. (B) *B. braunii* total hydrocarbon extract and squalene samples from *A* were solubilized in *n*-hexane and analyzed by Raman spectroscopy. Analysis was performed on *n*-hexane alone to determine background Raman spectra.

88

the absolute intensity was reduced (compare Fig. 34, A and B). The n-hexane sample alone did not show these bands (Fig. 34B).

Next, Raman spectroscopy was applied to individual botryococcenes in n-hexane and analyzed in the ν(C=C) stretching region to identify bands specific to the botryococcene structure. Pure C_{30}, C_{32}, C_{33}, and C_{34} botryococcenes were obtained by HPLC, purity was confirmed by GC, molecular weights were confirmed by fast atom bombardment-mass spectroscopy, and structures were confirmed by NMR as described previously [99-101]. It was unable to purify sufficient quantities of C_{31} botryococcene to analyze by Raman spectroscopy at this time and obtained a minimal amount of C_{30} botryococcene (3 mg) to obtain a workable spectrum. Analysis of all bands identified in the 1600–1700 cm^{-1} ν(C=C) stretching region of the spectra reveals that several of the bands can be assigned to specific bonds in botryococcenes. The band at 1647 cm^{-1} is seen in all botryococcenes except for C_{30} botryococcene (Fig. 35A). Because C_{30} botryococcene lacks methylation (Fig. 3B), this suggests that the 1647 cm^{-1} band originates from the exomethylene groups generated by the methylation events. The band at 1670 cm^{-1} is seen in all botryococcenes except C_{34} botryococcene (Fig. 35A), suggesting that it is due to the backbone C=C bonds because C_{34} botryococcene lacks these bonds with the exception of the C=C bond at C-11 (Fig. 35B). Moreover, squalene, which possesses only backbone C=C bonds, has its maximum Raman intensity at 1668 cm^{-1}. The bands at 1639 and 1660 cm^{-1} are more difficult to assign but appear to be specific to botryococcenes compared with squalene (Fig. 35A). These bands may be assigned to the branch C=C bond at C-26 and the backbone C=C bond at C-11 that are

89
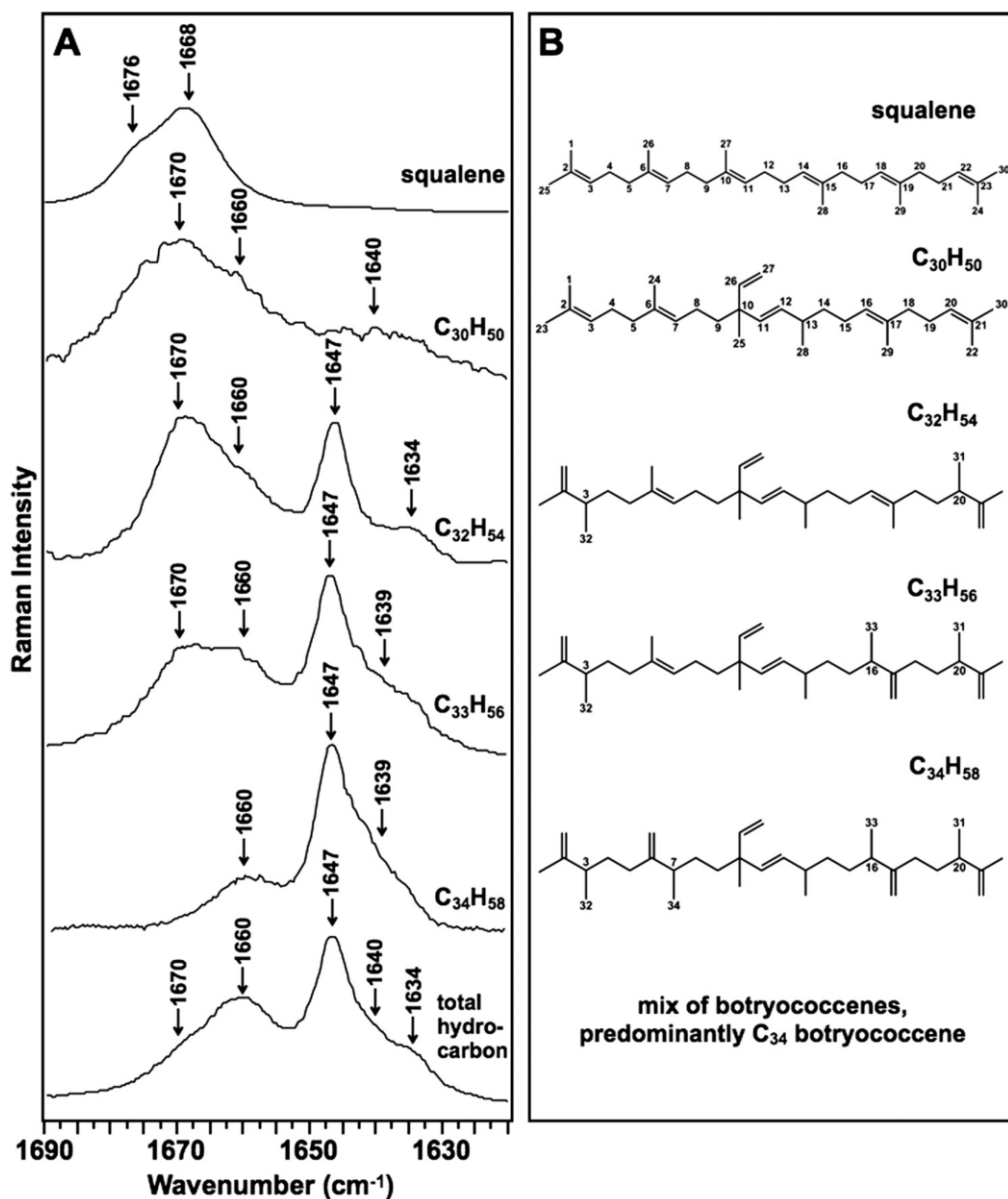
Figure 35. Raman spectra for the ν(C=C) stretching region of botryococcenes. (A) Indicated botryococcenes were purified from *B. braunii* by HPLC, dissolved in *n*-hexane, analyzed by Raman spectroscopy within the ν(C=C) stretching region, and compared with that for the total hydrocarbon extract and pure squalene. (B) Structures of squalene and individual botryococcenes analyzed in A.

found in all botryococcenes (Fig. 35B). This is supported by the spectrum for C_{34} botryococcene (Fig. 35A), which has three major bands: 1647 cm^{-1} attributed to the exomethylene groups and 1639 and 1660 cm^{-1}, which should be attributable to the C-26 and C-11 C=C bonds because they are the only other C=C bonds in C_{34} botryococcene (Fig. 35B). However, with these data it is difficult to assign these bands specifically to the C-26 or C-11 C=C bonds. A band at 1634 cm^{-1} is also seen in C_{32} botryococcene which cannot be assigned at this time.

These Raman spectra indicate that the Raman bands of 1639, 1647, 1660, and 1670 cm^{-1} are specific for botryococcenes. Thus, these bands could be used as diagnostic signatures for the presence of botryococcenes. The 1647 cm^{-1} band is specifically due to botryococcene methylation and may offer the best signature for Raman spectroscopy identification of botryococcenes. This is supported by the Raman spectrum of the total hydrocarbon fraction, which shows the four main botryococcene-specific bands of 1639, 1647, 1660, and 1670 cm^{-1} (Fig. 35A). Additionally, the band of 1634 cm^{-1} was detected in the total hydrocarbon fraction that was seen for C_{32} botryococcene and cannot be assigned at this time (Fig. 35A). It should be noted that the increasing methylation of botryococcenes is correlated with a shift of bands in the Raman spectra from the 1670 cm^{-1} region toward the 1647 cm^{-1} region (Fig. 35A).

2. Computational Analysis

Because sufficient quantities of C_{31} botryococcene for Raman spectroscopy were not obtained and specifically the 1639 and 1660 cm^{-1} bands (Fig. 35A) could not be

91

assigned, DFT calculations were used to address these problems as well as support the experimental spectra interpretation. There are two isomers of C_{31} botryococcene (Fig. 36A) that have been identified in *B. braunii* by methylation of C_{30} botryococcene at C-3 or C-20 [100-102] (Fig. 36A). The full Raman spectra from the calculations indicate that the major differences among all the botryococcenes analyzed are in the $\nu(C=C)$ stretching region as seen in the experimental spectra (Fig. 36B). Analysis of the 1600–1700 cm^{-1} region for $\nu(C=C)$ stretching shows strong similarities to our experimental spectra (Fig. 37). Fig. 37 shows the computed spectra for this region, and Table 9 lists the calculated wavenumber values and compares them with those observed experimentally. It should be noted that each molecule has six independent $\nu(C=C)$ stretching frequencies, but these may overlap to produce only two or three Raman bands depending on the type (backbone, exomethylene, or branch) of C=C bond present. Fig. 38 shows the individual stretching frequency calculated for each specific C=C bond for each of the molecules. Remarkably, the stretching vibration of each individual C=C bond is shown by the calculations to be almost totally independent and uncoupled to any of the other $\nu(C=C)$ stretching motions or to any other vibration. What clearly evident from Figs. 37 and 38 and Table 9 is that the three types of $\nu(C=C)$ stretching vibrations fall into distinct spectral regions. The backbone $\nu(C=C)$ stretching wavenumbers are calculated to be between 1663 and 1679 cm^{-1} for all the molecules and are observed in the 1660–1670 cm^{-1} region. The exomethylene stretches are calculated to be between 1646 and 1655 cm^{-1} and are all observed at 1647 cm^{-1}. The branch C=C stretches are computed to be in the 1642–1649 cm^{-1} range and are experimentally observed at 1639–

92
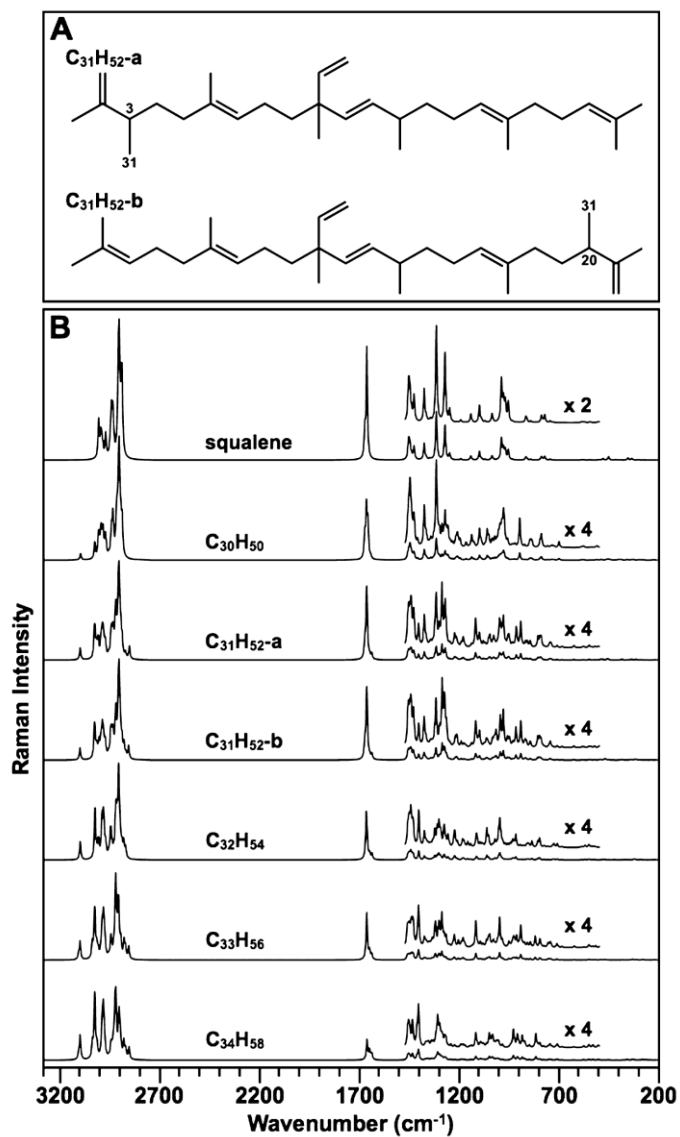
Figure 36. DFT-calculated Raman spectra for botryococcenes. (A) Structure of the two forms of C$_{31}$ botryococcene identified in *B. braunii*. (B) DFT-calculated Raman spectra for squalene and the indicated botryococcenes. DFT calculations were performed using the GAUSSIAN 03 package, and the computed spectra were assembled using the GaussView 4.1.2 program.
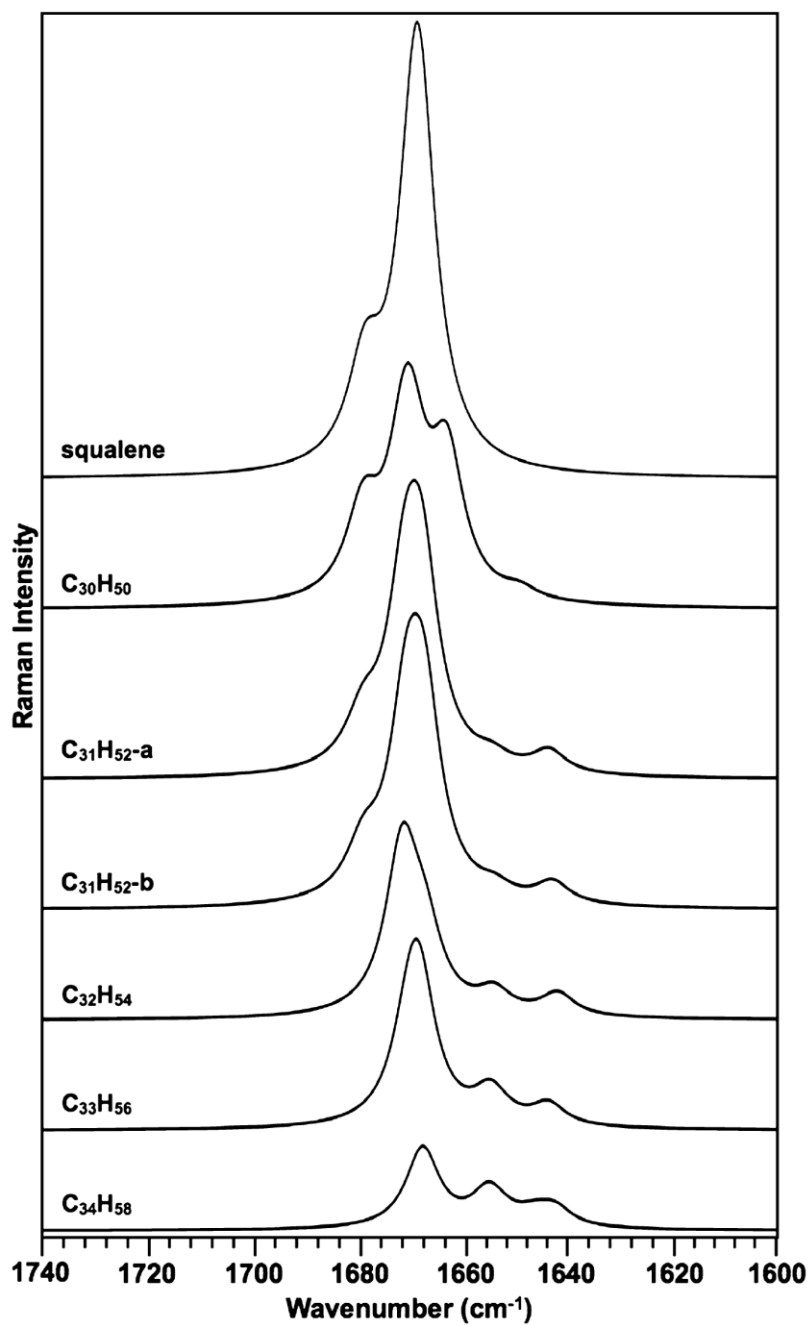
Figure 37. DFT-calculated Raman spectra for squalene and all botryococcenes in the ν(C=C) stretching region.
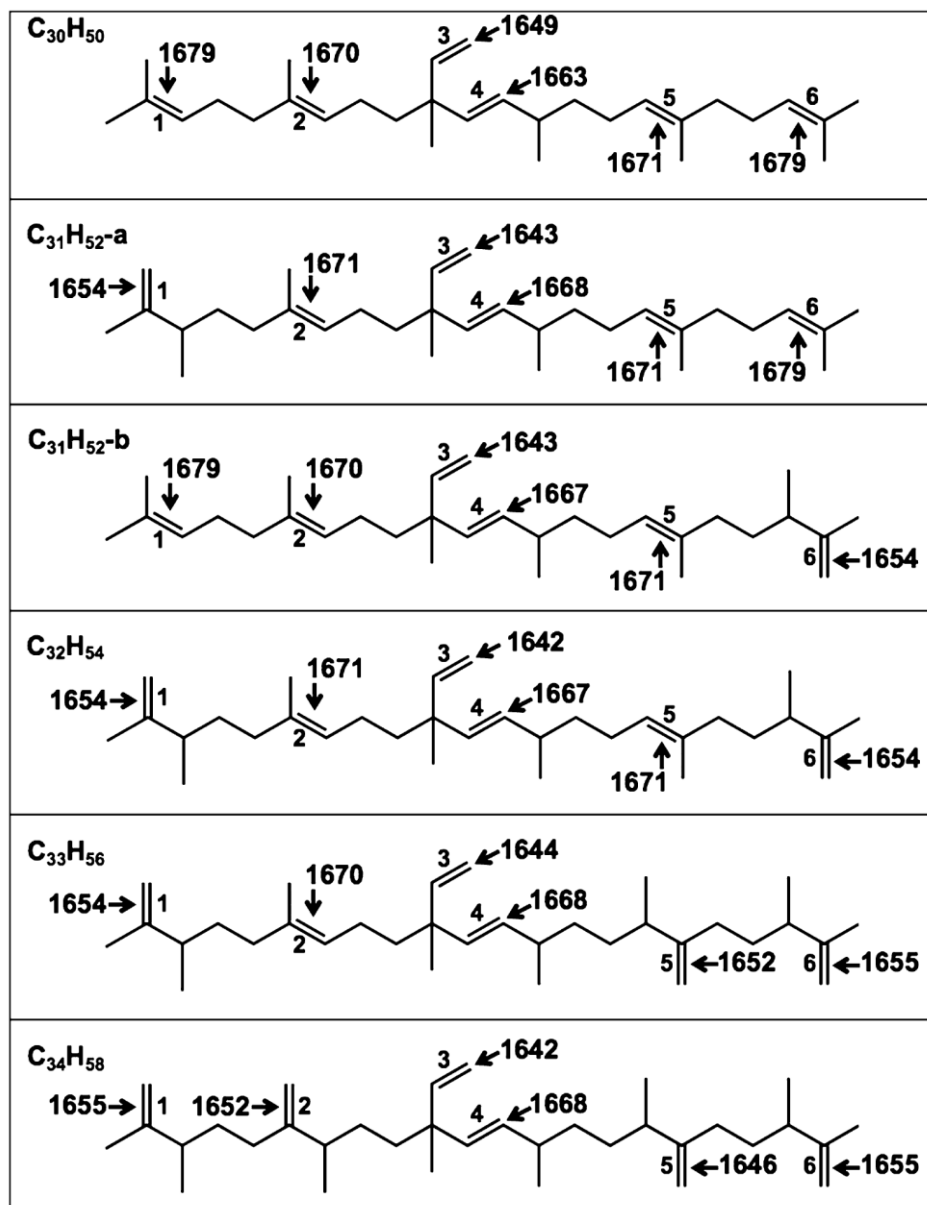
Figure 38. Calculated Raman wavenumbers for each C-C bond of individual botryococcenes.

Molecule	C=C type	Bond number (as shown in Fig. 38)	Frequency range	
			Observed	Calculated
			cm^{-1}	cm^{-1}
$C_{30}H_{50}$	Backbone	1, 2, 4, 5, 6	1970	1663-1979
	Exomethylene	NP[a]	NP	NP
	Branch	3	1640	1649
$C_{31}H_{52}$-a	Backbone	2, 4, 5, 6	ND[b]	1668-1679
	Exomethylene	1	ND	1654
	Branch	3	ND	1643
$C_{31}H_{52}$-b	Backbone	1, 2, 4, 5	ND	1667-1679
	Exomethylene	6	ND	1654
	Branch	3	ND	1643
$C_{32}H_{54}$	Backbone	2, 4, 5	1670	1667-1671
	Exomethylene	1, 6	1647	1654
	Branch	3	1639	1642
$C_{33}H_{56}$	Backbone	2, 4	1670	1668-1655
	Exomethylene	1, 5, 6	1647	1652-1655
	Branch	3	1639	1644
$C_{34}H_{58}$	Backbone	4	1660	1668
	Exomethylene	1, 2, 5, 6	1647	1646-1655
	Branch	3	1639	1642

[a] Not present in this structure.
[b] Not determined.

Table 9. Comparison of observed and calculated Raman bands for botryococcenes.

1640 cm^{-1}. Because the calculated Raman spectra were determined for fixed bonds of a linear botryococcene structure, it was analyzed how different conformations of the botryococcene structure would affect the Raman spectra.

It should be noted that each of these molecules has a large number of vibrations (3N−6 where N = number of atoms), and all of these are Raman-active. Thus, for example, $C_{34}H_{58}$ has 270 vibrations. These include 58 C–H stretching modes between 2800 and 3200 cm^{-1} and 33 skeletal stretching vibrations, including the ν(C=C) stretching modes. The remainders are various types of angle bending, twisting, wagging, rocking, etc. motions, and all are below 1500 cm^{-1}. In the present work the ν(C=C) stretching vibrations (1600–1700 cm^{-1}) is focused because these are well separated from all other modes and provide the means for discriminating between the different botryococcenes and their three types of C=C double bonds (backbone, exomethylene, and branch).

3. *In Vivo* Raman Spectroscopy Mapping of Botryococcenes

The Raman spectroscopy analysis presented here indicates that specific Raman bands can be used as markers for the presence of botryococcenes in live *B. braunii* cells and/or colonies. This is especially true for the 1647 cm^{-1} band that is specific for indicating the presence of methylated botryococcenes (Fig. 35A). Thus, Raman microspectroscopy was applied to a colony of *B. braunii* to map the presence of botryococcenes in the extracellular matrix and intracellular oil bodies. A roughly circular region within a 13 × 13-µm area of a *B. braunii* colony was scanned as shown in Fig. 39
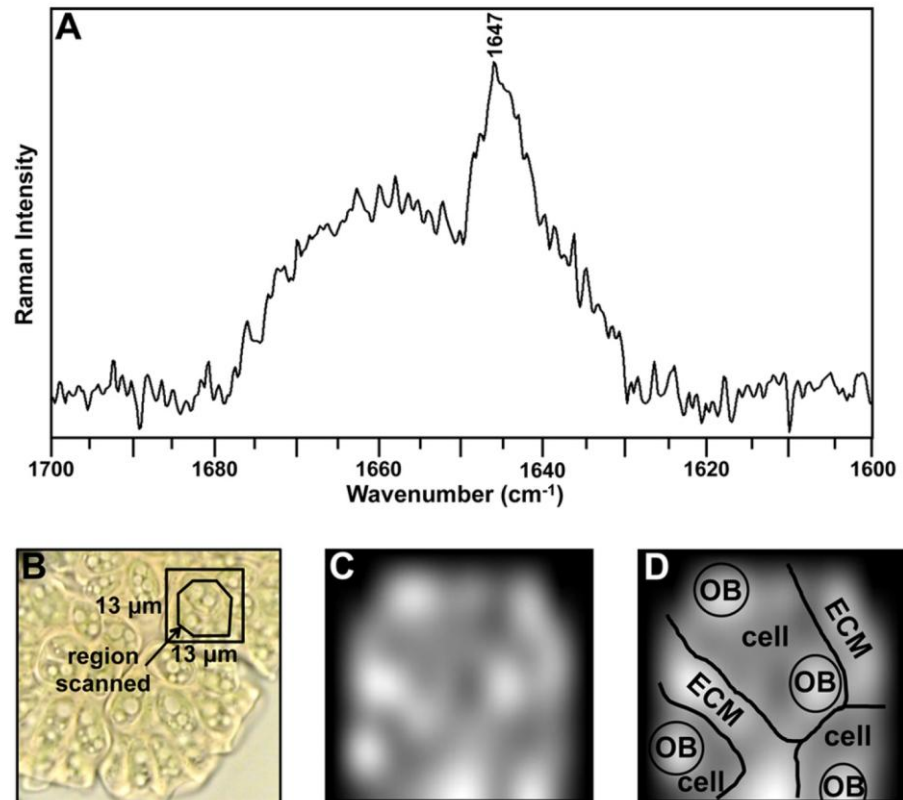
Figure 39. Mapping of methylated botryococcenes in a *B. braunii* colony. (A) *In vivo* Raman spectrum of a *B. braunii* colony. The laser of the confocal Raman microscope was focused on a 13 × 13-μm region of a colony of *B. braunii*, as shown in B, and the Raman spectrum of the region recorded. (B) Light microscope image of the *B. braunii* colony before photobleaching for Raman spectroscopy. Boxed region indicates region used for analysis in A. (C) Mapping of the 1647 cm^{-1} specific botryococcene Raman band in the *B. braunii* colony. (D) Graphical representation of colony structure in C. *OB*, oil body; *ECM*, extracellular matrix.

98

B. Spectroscopy was implemented after photobleaching, and the Raman spectrum in the 1700–1600 cm^{-1} region is shown in Fig. 39A. Detection of the botryococcene methylation-specific 1647 cm^{-1} band was evident and was the most prominent band in the spectrum (Fig. 39A). The high level of background within this spectrum prevented us from defining other botryococcenespecific bands.

4. The detection of the botryococcene methylation

Specific 1647 cm^{-1} band was mapped at 54 points yielding a spectral map of the scanned region of the *B. braunii* colony. The presence of the 1647 cm^{-1} band was assigned a white color with diminishing detection levels of the 1647 cm^{-1} band scaled to gray. Because our cells were photobleached prior to Raman analysis, the cells and extracellular matrix could not be distinguished by a microscopy image. Thus, Fig. 39D shows a graphical representation of the colony and cell structure. The results show, as expected and reported [103-105], that the extracellular matrix has high amounts of methylated botryococcenes (Fig. 39, C and D), likely C_{34} botryococcene because it is mostly found in the extracellular matrix [93-95,103,106]. The intracellular oil bodies also contained methylated botryococcenes as determined by detection of the 1647 cm^{-1} band (Fig. 39, C and D). Unfortunately, it was not able to determine the specific botryococcene makeup of the individual oil bodies beyond the presence of methylated botryococcenes because it was not able to assign and map additional Raman bands due to the high background in our analysis and sample degradation from prolonged interrogation (Fig. 39A).

Conclusion

These studies have identified specific Raman spectroscopic characteristics for botryococcenes of *B. braunii*, B race. Additionally, a botryococcene methylation-specific Raman signature can be detected in living *B. braunii* cells, indicating that Raman spectroscopy is a powerful tool that can be applied to advancing studies on botryococcene biosynthesis. A goal for future studies is to refine the Raman microspectroscopy using instrumentation appropriate to very small photosynthetic cells to fine-map the presence of the different botryococcene homologs in a colony of *B. braunii*. Of particular interest will be the location of the different botryococcenes within the cells to determine whether there is a biosynthetic, or composition difference among the many intracellular oil bodies. Additionally, Raman spectroscopy could be applied to analyze botryococcenes levels and quality during the development of a *B. braunii* culture to determine when oil levels are of both maximal quantity and quality for cell harvesting.

CHAPTER IX

CONCLUSIONS

Infrared and Raman spectroscopy have been used to collect vibrational spectra, and vibrational assignments have been made. Theoretical computational calculations were utilized to calculate vibrational frequencies, potential energy functions (PEFs) and structures of 2,4,7-Trioxa(3.3.0)octane (247TOO) and cyclic silanes. The characterization and vibrational frequencies of botryococcenes were determined using DFT calculations.

First, the infrared and Raman spectroscopy were used to determine the vibrational spectra for 247TOO. DFT calculation was utilized to calculate vibrational spectra and to aid in making vibrational assignments. *Ab initio* computations were used to calculate the structures and PEFs for 247TOO. The computed results provided four conformations. The lowest energy structure was the conformation which has both rings puckered up and the dihedral angles of puckering as 41.9 ° for the α ring with the single oxygen and 36.0 ° for the β ring with two oxygens. The potential energy surface (PES) was determined using the MP2 method and the cc-pVTZ basis set. The PES is

$$
\begin{aligned}
V\ (cm^{-1}) =\ & 6.324x10^5\ x_1^4 + 2.250x10^4\ x_1^3 - 6.551x10^4\ x_1^2 \\
& + 1.781x10^6\ x_2^4 + 2.766x10^4\ x_2^3 - 9.851x10^4\ x_2^2 \\
& + 3.223x10^5\ x_1^2\ x_2^2 - 4.809x10^3\ x_1^3\ x_2 + 4.443x10^4\ x_1\ x_2^3 \\
& - 3.116x10^3\ x_1 - 1.589x10^3\ x_2 + 2.001x10^3\ x_1\ x_2 \\
& + 1.309x10^5\ x_1^6 + 1.039x10^4\ x_1^5 - 9.946x10^4\ x_2^6 \\
& - 8.653x10^4\ x_2^5 + 9.827x10^6\ x_1^4\ x_2^2 - 1.391x10^7\ x_1^2\ x_2^4 \\
& - 3.136x10^5\ x_1^3\ x_2^3 + 9.684x10^5\ x_1^5\ x_2 + 8.336x10^4\ x_1\ x_2^2 \\
& + 3141
\end{aligned}
\tag{9.1}
$$

The x_1 and x_2 are puckering coordinates depending on α ring and β ring, respectively. This PES was used to determine the energy levels for this surface using the Meinander-Laane DA2OPTN4 program. The wavefunctions were also calculated for the energy levels of each walls of the PES. This study has helped us to understand the anomeric effect and torsional forces of two rings. The β ring with two oxygens showed the anomeric effect due to the O-C-O bonding configuration. The puckering of α ring with the single oxygen was determined by the torsional strain between the CH_2 group and H-C-O grouping on the bridgehead carbon atom.

Second, the DFT and *ab initio* computations were carried out to calculate the vibrational spectra, vibrational assignments, structures, and potential energy functions (PEFs). In this work the calculated and previously recorded infrared and Raman spectra were compared to determine their vibrational assignments for 1,3-disilacyclopent-4-ene, 1,3-disilacyclopentane, 1,1,3,3-tetrachloro-1,3-disilacyclopent-4-ene, and 1,1,3,3-tetrachloro-1,3-disilacyclopentane. The PEFs were determined using MP2/cc-pVTZ computations. Each energy point was collected point by point. The *ab initio* computations of 1-silacyclopent-3-ene and 1,3-disilacyclopent-4-ene were utilized to compare to the experimentally determined functions. These are shown in equations (9.2) and (9.3), respectively.

$$V(cm^{-1}) = 2.130 \times 10^5 x^4 - 0.0054 \times 10^5 x^2 \text{ (experimental fit)}$$

$$V(cm^{-1}) = 2.220 \times 10^5 x^4 - 0.0183 \times 10^5 x^2 \text{ (\textit{ab initio})} \qquad (9.2)$$

$$V(cm^{-1}) = 1.480 \times 10^5 x^4 + 0.0300 \times 10^5 x^2 \text{ (experimental fit)}$$

$$V(cm^{-1}) = 1.830 \times 10^5 x^4 + 0.0203 \times 10^5 x^2 \text{ (\textit{ab initio})} \tag{9.3}$$

The *ab initio* calculations were in remarkably good agreements with the experimentally determined functions. The conformational energies for silacyclopentane and 1,3-disilacyclopentane have also been calculated and one-dimensional ring-twisting and pseudorotational potential energy functions were generated. Their agreements were in excellent agreement.

Third, vibrational spectra for squlalene and botryococcenes of *B. braunii* were collected using infrared and Raman spectroscopy. The DFT computations were carried out to determine their calculated spectra and vibrational assignments. In this study the vibrational assignment and structure studies of squalene were reported. This theoretical study helped to understand its structure and vibrational frequencies. The characterization of botryococcenes was aided using Raman spectroscopy and B3LYP/cc-pVTZ computations. DFT computations indentified each ν(C=C) stretching bond of individual botryococcenes. They were mostly independent and uncoupled to any of the other (C=C) stretching motions or to any other vibration. Each botryococcene has three types of C=C bonds, namely backbond, exomethylene, and branch. The backbone C=C bonds appeared in 1670-1679 cm^{-1} region. The exomethylene C=C bonds were in 1652-1655 cm^{-1} region, and branch C=C bonds gave 1642-1649 cm^{-1}. The agreements between observed and calculated Raman spectra were good evidence to understand and analyze botryococcenes.

REFERENCES

[1]   J. Laane, "Vibrational potential energy surfaces in electronic excited states" in Frontiers of Molecular Spectroscopy, J. Laane, Ed., Elsevier Publishing, Amsterdam, 2009, pp. 63-132. J. Laane, Ed., Elsevier Publishing, Amsterdam, The Netherlands, 2009, 706 pp.

[2]   J. Laane, J. Phys. Chem. A. 104 (2000) 7715.

[3]   J. Yang and J. Laane, J. Elec. Spectrosc. and Related Phenomena 156-158 (2007) 45.

[4]   L. F. Colegrove and J. Laane, J. Phys. Chem. 95 (1991) 6494.

[5]   J. D. Lewis, T. H. Chao, and J. Laane, J. Chem. Phys. 62 (1975) 1932.

[6]   P. M. Killough and J. Laane, J. Chem. Phys. 80 (1984) 5475.

[7]   T. H. Chao and J. Laane, Acta Part A 28 (1972) 2443.

[8]   J. Laane, J. Chem. Phys. 50 (1969) 776.

[9]   L. F. Colegrove, J. C. Wells, and J. Laane, J. Chem. Phys. 93 (1990) 6291.

[10]   L. F. Colegrove, Ph.D. Thesis, Texas A&M University, 1989.

[11]   L. H. Reddy and P. Couvreur, Adv. Drug Deliv. Rev. 61 (2009) 1412.

[12]   B. H. Amdur, E. I. Szabo, and S. S. Socransky, J. Bacteriol. 135 (1978) 161.

[13]   V. Baeten, P. Dardenne, and R. Aparicio, J. Agric. Food Chem. 49 (2001) 5098.

[14]   S. A. Simon, L. J. Lis, R. C. MacDonald, and J. W. Kauffman, Biophys. J. 19 (1977) 83.

[15] M. K. Weldon, M. D. Morris, A. B. Harris, and J. K. Stoll, J. Lipid Res. 39 (1998) 1896.

[16] M. K. Weldon, V. R. Zhelyaskov, and M. D. Morris, Appl. Spectrosc. 52 (1998) 265.

[17] Y. Y. Huang, C. M. Beal, W. W. Cai, R. S. Ruoff, and E. M. Terentjev, Biotechnol. Bioeng. 105 (2010) 889.

[18] M. J. Frisch, G. W. Trucks, H. B. Schlegel, G. E. Scuseria, M. A. Robb, J. R. Cheeseman, J. A. Montgomery, Jr., T. Vreven, K. N. Kudin, J. C. Burant, J. M. Millam, S. S. Iyengar, J. Tomasi, V. Barone, B. Mennucci, M. Cossi, G. Scalmani, N. Rega, G. A. Petersson, H. Nakatsuji, M. Hada, M. Ehara, K. Toyota, R. Fukuda, J. Hasegawa, M. Ishida, T. Nakajima, Y. Honda, O. Kitao, H. Nakai, M. Klene, X. Li, J. E. Knox, H. P. Hratchian, J. B. Cross, V. Bakken, C. Adamo, J. Jaramillo, R. Gomperts, R. E. Stratmann, O. Yazyev, A. J. Austin, R. Cammi, C. Pomelli, J. W. Ochterski, P. Y. Ayala, K. Morokuma, G. A. Voth, P. Salvador, J. J. Dannenberg, V. G. Zakrzewski, S. Dapprich, A. D. Daniels, M. C. Strain, O. Farkas, D. K. Malick, A. D. Rabuck, K. Raghavachari, J. B. Foresman, J. V. Ortiz, Q. Cui, A. G. Baboul, S. Clifford, J. Cioslowski, B. B. Stefanov, G. Liu, A. Liashenko, P. Piskorz, I. Komaromi, R. L. Martin, D. J. Fox, T. Keith, M. A. Al-Laham, C. Y. Peng, A. Nanayakkara, M. Challacombe, P. M. W. Gill, B. Johnson, W. Chen, M. W. Wong, C. Gonzalez, and J. A. Pople, Gaussian 03, revision C.2, Gaussian, Inc., Wallingford CT, 2004.

[19] M. J. Frisch, G. W. Trucks, H. B. Schlegel, G. E. Scuseria, M. A. Robb, J. R. Cheeseman, G. Scalmani, V. Barone, B. Mennucci, G. A. Petersson, H. Nakatsuji, M. Caricato, X. Li, H. P. Hratchian, A. F. Izmaylov, J. Bloino, G. Zheng, J. L. Sonnenberg, M. Hada, M. Ehara, K. Toyota, R. Fukuda, J. Hasegawa, M. Ishida, T. Nakajima, Y. Honda, O. Kitao, H. Nakai, T. Vreven, J. A. Montgomery Jr., J. E. Peralta, F. Ogliaro, M. Bearpark, J. J. Heyd, E. Brothers, K. N. Kudin, V. N. Staroverov, R. Kobayashi, J. Normand, K. Raghavachari, A. Rendell, J. C. Burant, S. S. Iyengar, J. Tomasi, M. Cossi, N. Rega, N. J. Millam, M. Klene, J. E. Knox, J. B. Cross, V. Bakken, C. Adamo, J. Jaramillo, R. Gomperts, R. E. Stratmann, O. Yazyev, A. J. Austin, R. Cammi, C. Pomelli, J. W. Ochterski, R. L. Martin, K. Morokuma, V. G. Zakrzewski, G. A. Voth, P. Salvador, J. J. Dannenberg, S. Dapprich, A. D. Daniels, €O. Farkas, J. B. Foresman, J. V. Ortiz, J. Cioslowski, and D. J. Fox, Gaussian 09, Revision A.02, Gaussian, Inc., Wallingford, CT, 2009.

[20] R. P. Bell, Proc. R. Soc. London, Ser. A 183 (1945) 328.

[21] J. Laane, Int. Rev. Phys. Chem. 18 (1999) 301.

[22] J. Laane, Annu. Rev. Phys. Chem. 45 (1994) 179.

[23] J. Laane, Pure Appl. Chem. 59 (1987) 1307.

[24] J. Laane, "Pseudorotation of five-membered rings" in Vibrational Spectra and Structure, J. Durig, Ed., Marcell Deckker, Inc., 1972, Vol. 1, pp. 25-50.

[25] J. Laane, Quart. Rev. Chem. Soc. 25 (1971) 533.

[26] N. Meinander and J. Laane, J. Mol. Struct. 569 (2001) 1.

[27]   J. D. Lewis, T. B. Malloy Jr., T. H. Chao, and J. Laane, J. Mol. Struct. 12 (1972) 427.

[28]   N. Meinander and J. Laane, J. Mol. Struct. 569 (2001) 1.

[29]   D. Autrey, N. Meinander, and J. Laane, J. Phys. Chem. 108 (2004) 409.

[30]   E. J. Ocola, N. Meinander, and J. Laane, J. Chem. Phys. 2014, in press.

[31]   H. L. Sheu and J. Laane, J. Phys. Chem. A 2014, submitted.

[32]   J. Villarreal, unpublished synthesis paper.

[33]   K. Haller, W. -Y. Chiang, A. del Rosario, and J. Laane, J. Mol. Struct. 379 (1996) 19.

[34]   J. Laane, K. Haller, S. Sakurai, K. Morris, D. Autrey, Z. Arp, W. -Y. Chiang, and A. Combs, J. Mol. Struct. 650 (2003) 57.

[35]   E. Cortez, R. J. Verastegui, J. Villarreal, and J. Laane, J. Amer. Chem. Soc. 115 (1993) 12132.

[36]   S. Sakurai, N. Meinander, K. Morris, and J. Laane, J. Amer. Chem. Soc. 121 (1999) 5056.

[37]   J. Laane, Appl. Spectrosc. 24 (1970) 73.

[38]   A. A. Al-Saadi and J. Laane, J. Mol. Struct. 830 (2007) 46.

[39]   A. A. Al-Saadi, N. Meinander, and J. Laane, J. Mol. Spectrosc. 242 (2007) 17.

[40]   H. J. Chun and J. Laane, unpublished results.

[41]   J. Laane, J. Chem. Phys. 52 (1970) 358.

[42]   M. B. Kelly and J. Laane, J. Phys. Chem. 92 (1988) 4056.

[43]   A. A. Al-Saadi and J. Laane, Organometallics 27 (2008) 3435.

[44]   M. A. Harthcock, J. M. Cooke, and J. Laane, J. Phys. Chem. 86 (1982) 4335.

[45]   J. F. Blanke, T. H. Chao, and J. Laane, J. Mol. Spectrosc. 38 (1971) 483.

[46]   J. Laane, Acta Part A 26 (1970) 517.

[47]   J. Laane and R. C. Lord, J. Chem. Phys. 48 (1968) 1508.

[48]   J. Laane, J. Am. Chem. Soc. 89 (1967) 1144.

[49]   M. Z. M. Rishard, R. M. Irwin, and J. Laane, J. Phys. Chem. A 111 (2007) 825.

[50]   R. M. Irwin, J. M. Cooke, and J. Laane, J. Am. Chem. Soc. 99 (1977) 3273.

[51]   J. Laane, J. Mol. Struct. 126 (1985) 99.

[52]   D. L. Philen, T. H. Chao, and J. Laane, J. Mol. Struct. 16 (1973) 417.

[53]   J. Laane, J. Chem. Phys. 50 (1969) 1946.

[54]   H. J. Chun, L. F. Colegrove, and J. Laane, J. Mol. Struct. 1049 (2013) 172.

[55]   M. B. Kelly and J. Laane, J. Phys. Chem. 93 (1989) 8388.

[56]   M. A. Harthcock and J. Laane, J. Mol. Spectrosc. 94 (1982) 461.

[57]   M. A. Harthcock and J. Laane, J. Mol. Spectrosc. 91 (1982) 300.

[58]   T. P. Devarenne, "Terpenoids: higher" in Encyclopedia of Life Sciences (ELS), John Wiley & Sons, Chichester, 2009.

[59]   R. Do, R. S. Kiss, D. Gaudet, and J. C. Engert, Clin. Genet. 75 (2009) 19.

[60]   Z. R. Huang, Y. K. Lin, and J. Y. Fang, Molecules 14 (2009) 540.

[61]   S. Passi, O. De Pita, P. Puddu, and G. P. Littarru, Free Radic. Res. 36 (2002) 471.

[62]   H. J. Channon, Biochem. J. 20 (1926) 400.

[63]   M. Tsujimoto, Ind. Eng. Chem. 8 (1916) 889.

[64]   Y. Kohno, Y. Egawa, S. Itoh, S. Nagaoka, M. Takahashi, and K. Mukai, Biochim. Biophys. Acta 1256 (1995) 52.

[65]   D. Saint-Leger, A. Bague, E. Lefebvre, E. Cohen, and M. Chivot, Br. J. Dermatol. 114 (1986) 543.

[66]   H. L. Newmark, Ann. N. Y. Acad. Sci. 889 (1999) 193.

[67]   R. W. Owen, W. Mier, A. Giacosa, W. E. Hull, B. Spiegelhalder, and H. Bartsch, Food Chem. Toxicol. 38 (2000) 647.

[68]   E. Escrich, M. Solanas, R. Moral, I. Costa, and L. Grau, Clin. Transl. Oncol. 8 (2006) 868.

[69]   F. Warleta, M. Campos, Y. Allouche, C. Sanchez-Quesada, J. Ruiz-Mora, G. Beltran, and J. J. Gaforio, Food Chem. Toxicol. 48 (2010) 1092.

[70]   T. J. Smith, G. Y. Yang, D. N. Seril, J. Liao, and S. Kim, Carcinogenesis 19 (1998) 703.

[71]   T. G. Sotiroudis and S. A. Kyrtopoulos, Eur. J. Nutr. 47 (Suppl. 2) (2008) 69.

[72]   J. Mathews, J. Natl. Cancer Inst. 84 (1992) 1000.

[73]   C. B. Fox, Molecules 14 (2009) 3286.

[74]   G. W. Robinson, Y. H. Tsay, B. K. Kienzle, C. A. Smith-Monroy, and R. W. Bishop, Mol. Cell. Biol. 13 (1993) 2706.

[75]   P. Gu, Y. Ishii, T. A. Spencer, and I. Shechter, J. Biol. Chem. 273 (1998) 12515.

[76]   T. L. Weiss, H. J. Chun, S. Okada, S. Vitha, A. Holzenburg, J. Laane, and T. P. Devarenne, J. Biol. Chem. 285 (2010) 32458.

[77]   P. Metzger and C. Largeau, Appl. Microbiol. Biotechnol. 66 (2005) 486.

[78]   Q. Hu, M. Sommerfeld, E. Jarvis, M. Ghirardi, M. Posewitz, M. Seibert, and A. Darzins, Plant J. 54 (2008) 621.

[79]   Y. Chisti, Trends Biotechnol. 26 (2008) 126.

[80]   Y. Chisti, Biotechnol. Adv. 25 (2007) 294.

[81]   B. R. Wood, P. Heraud, S. Stojkovic, D. Morrison, J. Beardall, and D. Mc-Naughton, Anal. Chem. 77 (2005) 4955.

[82]   W. D. Wagner, and W. Waidelich, Appl. Spectrosc. 40 (1986)191.

[83]   Q. Wu, W. H. Nelson, P. Hargraves, J. Zhang, C. W. Brown, and J. A. Seelenbinder, Anal. Chem. 70 (1998) 1782.

[84]   S. K. Brahma, P. E. Hargraves, W. F. Howard, and W. H. Nelson, Appl. Spectrosc. 37 (1983) 55.

[85]   M. Chen, H. Zeng, A. W. Larkum, and Z. L. Cai, Spectrochim. Acta A. Mol. Biomol. Spectrosc. 60 (2004) 527.

[86]   Y. Kubo, T. Ikeda, S. -Y. Yang, and M. Tsuboi, Appl. Spectrosc. 54 (2000) 1114.

[87]   B. Li, D. Mao, Y. Liu, L. Li, and T. Kuang, Photosynth. Res. 83 (2005) 297.

[88]   H. G. M. Edwards, L. F. C. de Oliveira, C. S. Cockell, J. C. Ellis-Evans, and D. D. Wynn-Williams, Int. J. Astrobiol. 3 (2004) 125.

[89]   C. Largeau, E. Casadevall, C. Berkaloff, and P. Dhamelincourt, Phytochemistry 19 (1980) 1043.

[90]   P. Heraud, B. R. Wood, J. Beardall, and D. McNaughton, J. Chemometrics 20 (2006) 193.

[91]   P. Heraud, J. Beardall, D. McNaughton, and B. R. Wood, FEMS Microbiol. Lett. 275 (2007) 24.

[92]   E. Eroglu and A. Melis, Bioresource Technol. 101 (2010) 2359.

[93]   J. R. Maxwell, A. G. Douglas, G. Eglinton, and A. McCormick, Phytochemistry 7 (1968) 2157.

[94]   B. A.Knights, A. C.Brown, E. Conway, and B. S. Middleditch, Phytochemistry 9 (1970) 1317.

[95]   A. Banerjee, R. Sharma, Y. Chisti, and U. C. Banerjee, Crit. Rev. Biotechnol. 22 (2002) 245.

[96]   D. Elsey, D. Jameson, B. Raleigh, and M. J. Cooney, J. Microbiol. Methods 68 (2007) 639.

[97]   S. J. Lee, B. -D. Yoon, and H.-M. Oh, Biotech. Tech. 12 (1998) 553.

[98]   K. E. Cooksey, J. B. Guckert, S. A. Williams, and P. R. Callis, J. Microbial. Methods 6 (1987) 333.

[99]   Y. Sato, Y. Ito, S. Okada, M. Murakami, and H. Abe, Tetrahedron Lett. 44 (2003) 7035.

[100]   E. Eroglu and A. Melis, Bioresource Technol. 101 (2010) 2359.

[101]   S. Okada, M. Murakami, and K. Yamaguchi, J. Appl. Phycol. 7 (1995) 555.

[102]   Z. Huang, and C. D. Poulter, Phytochemistry 28 (1989) 3034.

[103]   P. Metzger, M. David, and E. Casadevall, Phytochemistry 26 (1987) 129.

[104]   E. Casadevall, P. Metzger, and M. P. Puech, Tetrahedron Lett. 25 (1984) 4123.

[105]   F. R. Wolf, E. K. Nemethy, J. H. Blanding, and J. A. Bassham, Phytochemistry 24 (1985) 733.

[106]   F. R. Wolf, A. M. Nonomura, and J. A. Bassham, J. Phycol. 21 (1985) 388.